AN EXPERIMENTAL EVALUATION OF IMAGE QUALITY FOR VARIOUS SCENARIOS IN A CHROMOTOMOGRAPHIC SYSTEM WITH A SPINNING PRISM

THESIS

Kyle J. Dufaud, Captain, USAF

AFIT-ENP-14-M-07

DEPARTMENT OF THE AIR FORCE
AIR UNIVERSITY

AIR FORCE INSTITUTE OF TECHNOLOGY

Wright-Patterson Air Force Base, Ohio

AFIT-ENP-14-M-07

AN EXPERIMENTAL EVALUATION OF IMAGE QUALITY FOR VARIOUS

SCENARIOS IN A CHROMOTOMOGRAPHIC SYSTEM WITH A SPINNING PRISM

THESIS

Presented to the Faculty

Department of Engineering Physics

Graduate School of Engineering and Management

Air Force Institute of Technology

Air University

Air Education and Training Command

in Partial Fulfillment of the Requirements for the

Degree of Master of Science

Kyle J. Dufaud, B.S.

Captain, USAF

March 2014

AFIT-ENP-14-M-07

AN EXPERIMENTAL EVALUATION OF IMAGE QUALITY FOR VARIOUS

SCENARIOS IN A CHROMOTOMOGRAPHIC SYSTEM WITH A SPINNING PRISM

Kyle J. Dufaud, B.S.
Captain, USAF

Approved:

//signed//	13 March 2014
Michael R. Hawks, PhD (Chairman)	Date
//signed//	11 March 2014
Michael T. Eismann, PhD (Member)	Date
//signed//	17 March 2014
Glen P. Perram, PhD (Member)	Date

Abstract

A lab and field based hyperspectral chromotomographic imager has been developed at the Air Force Institute of Technology. It is a prototype used to study the requirements for a space-based system. The imager uses a high speed visible band camera behind a direct-vision prism to image both spatial dimensions and the spectral dimension at the same time. Capturing all 3 simultaneously allows for the hyperspectral imaging of transient events. The prism multiplexes the spectral and spatial information, so tomographic reconstruction algorithms must be used to separate hyperspectral channels.

Experiments were conducted to compare reconstructed image quality as a function of spatial, spectral, and temporal complexity. To test spatial complexity, a simulated point source, a standard bar chart, and an amorphous object were imaged. The more simple objects were reconstructed well. When objects dispersed by the prism overlapped in the raw data, reconstructions diminished. To test spectral complexity, atomic emission lines and white light with different types of optical filters were imaged. Because of the way the prism disperses light, shorter wavelengths were reconstructed better than longer ones. The temporal complexity experiments determined 3/4 of a prism revolution is sufficient (with approximately 60 projections) to reconstruct a scene as long as there were a sufficient number of frames in the recording. As few as 12 frames are sufficient in a complete revolution. Finally, a fireball was imaged in a field experiment. The chromotomographic imager constructed the spectrum of the fireball with very wide spectral lines.

Hindrances to reconstruction, such as a cone of missing hyperspectral information, are discussed. Additionally, a comparison of and improvements to the reconstruction algorithms are suggested.

Table of Contents

List of Figures

Figure

Page

x

xii

List of Tables

List of Symbols

Symbol	Definition
Hz	Hertz (cycles per second)
nm	Nanometers
μm	Microns
μs	Micro seconds
λ	Wavelength
$K_{1,2,3}$	Sellmeier K coefficient
$L_{1,2,3}$	Sellmeier L coefficient
n	Index of refraction
$\xi_{1,2}, \zeta$	Frequency Variables
x, y	Pixel locations
η	Quantum Efficiency
μrad	Microradian
mm	Millimeters
A	Amp
W	Watt
h	Planck's Constant, $6.626x10^{-34} J \cdot s$
c	Speed of light, $3x10^8 \frac{m}{s}$
q	Charge of an electron, $1.6x10^{-19}C$
K	Kelvin
ν	Modulation

List of Acronyms

Acronym	Definition
AFIT	Air Force Institute of Technology
AAA	anti-aircraft artillery
HSI	Hyperspectral imagers
FPA	focal plane array
DVP	direct vision prism
CTEx	Chromotomography Experiment
FOV	field of view
CT	Computed Tomography
MAE	Mean Absolute Error
FWHM	Full Width Half Max
POCS	Projections Onto Convex Sets
QE	quantum efficiency
STF	System Transfer Function
PSF	Point Spread Function
COTS	Commercial Off The Shelf
MTF	Modulation Transfer Function
CCD	Charge-Couple Device

AN EXPERIMENTAL EVALUATION OF IMAGE QUALITY FOR VARIOUS

SCENARIOS IN A CHROMOTOMOGRAPHIC SYSTEM WITH A SPINNING PRISM

I. Introduction

1.1 Motivation

Battle space managers and the intelligence community require accurate information on their areas of responsibility. It is difficult for them to get this information from transient events, such as bomb blasts, artillery/anti-aircraft artillery (AAA), muzzle flashes, and missile launches. In order to provide accurate information, intelligence analysts must be able to identify, classify, and characterize such events. One method used to capture these kinds of images is with a hyperspectral remote sensor placed on a satellite. Hyperspectral Imagers capture 2 spatial dimensions over a broad spectral band of a scene [9], which can indicate location and chemical composition of a bomb blast. Hyperspectral imagers (HSI)s also measure incoming light at a large number of wavelengths. Analysts are able to compare the spectral composition with known data about various materials, especially those used in explosives. Typically, this technology is best suited to capture static or slowly evolving scenes. That is insufficient, however, for an event that might last for only a few thousandths of a second.

1.2 Hyperspectral Imagers

Hyperspectral imagers are imaging spectrometers: they capture 2 spatial dimensions and a spectral dimension of information and store it in a hypercube, as seen in Figure 1.1 [15]. Imaging systems remotely measure the spatial relationships between objects in a scene. Spectrometers measure the intensities of various wavelengths of light, which can
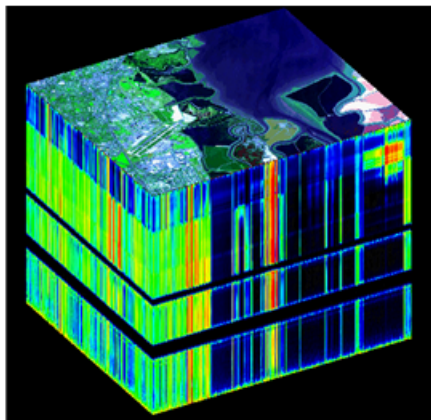
Figure 1.1: Hypercube taken from AVIRIS platform over Moffet Field, CA [15].

be used to determine chemical composition. The x and y axes of the hypercube make up the spatial dimensions. The z axis contains the spectral information. A slice of the cube parallel to the x-y plane yields the entire spatial scene for one small wave band or wavelength. Likewise, looking at a single pixel through each of the slices will yield the spectrum of that pixel. HSIs use a dispersive element, like a diffraction grating or a prism, to diffract individual wavelengths of light into unique positions on the camera's focal plane array. There are 2 common types of HSI: scanning-slit and optical filter imagers.

Optical filter imagers look at the entire field of view of the scene at a time, but only images over a narrow spectral band. As it finishes in the first band, the filters are adjusted to pass the next band of light, and so on until the entire spectrum of interest has been imaged. This is a slow and inefficient way of performing HSI for the quickly changing scenario, but simple to build the hypercube. Its ability to measure the difference between 2 wavelengths, or spectral resolution, is also limited by the quality, bandpass, and number of filters.

The scanning-slit method looks over the entire spectrum, but over only one spatial dimension (one row or column of pixels) at a time. Like in the optical filter method, once the instrument finishes recording a row of pixels, it moves on the the next row, records, and so forth until the entire scene has been captured. This method is also simple to rebuild

the hypercube, but is far too slow to capture the transient events in which analysts are interested. The ability to distinguish between objects, or spatial resolution, is limited by the width of the slit and pixel size, among other things.

A third and less common hyperspectral imager is a tomographic HSI. Tomographic HSIs, inspired by the medical community's Computed Tomography (CT), use a diffraction element to separate the light from a scene into its component wavelengths onto the camera's focal plane array (FPA). This method images both spatial dimensions over the entire spectral band simultaneously. It is expected to be able capture transient scenes without losing any data. The difficulties lie in reconstructing the scene, as it is quite complicated. Since no filters are used, the spatial information from each wavelength can overlap, muddling both spatial and spectral information. It is up to computer algorithms to make something useful out of the raw data. The practice is called chromotomography.

1.3   Research Goals

The Air Force Institute of Technology (AFIT) is working on a solution to identify information from transient events anywhere in the world. The project called Chromoto-mography Experiment (CTEx), is putting a hyperspectral imager on a satellite. The AFIT Engineering Physics and Astronautical Engineering (ENP and ENY, respectively) depart-ments are working together to create a tomographic HSI with a direct vision prism. For this project, only the visible portion of the spectrum will be recorded. That will nominally be in the range of 400-800 nm. Everything will also be passively imaged - only the light emitted from or reflected by the object provides information.

This thesis will focus on the varying degrees of complexity a chromotomographic imager might encounter, and how the hypercube's image quality is affected by the complexity. Goals specifically addressed by this research project include:

- Establish reliable metrics for chromotomographic image quality

3

- Establish method to estimate accuracy and resolution of spectra

- Determine the utility of using the backprojection then filter reconstruction

- Measure image quality as a function of spatial complexity

  - Measure a pinhole, a simple 2 dimensional image, and a spatially complex scene illuminated by simple spectra

- Measure image quality as a function of spectral complexity

  - Measure monochromatic light, atomic lines, filtered and unfiltered white light's effect on scenes of simple spatial complexity

- Measure image quality as a function of time

  - Determine how the number of frames affects reconstruction

  - Determine the effect of motion blur from the spinning prism affects reconstruction

  - Determine how a changing spatial scene affects reconstruction

- Image and reconstruct a fireball to encompass all previous items in this list

1.4 Organization

Chapter 2 will lay out the background and theories associated with this project. Chapter 3 will describe the methodology - how the data were collected and processed. It specifically addresses the MATLAB code used in the data reconstruction process. Chapter 3 also explains how the hypercube was used to evaluate image quality. Chapter 4 describes the results and compares them to theory. It goes into detail on the specific steps used in collecting laboratory and field data. Chapter 5 lays out conclusions and makes recommendations for future work.

II. Background and Theory

Over the past several years, the Engineering Physics and Astronautical Engineering departments at AFIT have been developing a hyperspectral imager that uses a direct vision prism (DVP) to collect spatial and spectral information. The rapidly rotating prism allows the HSI to image scenes that develop in a matter of milliseconds [5][20][24].   While sufficient for collecting spatial and spectral information, the scanning-slit and optical filter mechanisms are too slow to record transient events at millisecond timescales. Additionally, Mantravadi explains that a DVP will provide better spatial and spectral resolution than a diffraction grating [16].

2.1 Chromotomography

Chromotomography, has its roots in the medical field.   A CT, or computed tomographic imager, consists of an x-ray transmitter and receiver placed 180° from each other.   They rotate about a stationary patient and take pictures through a 360° collection [12].   Like chromotomography, CT's goal is to compile a 3 dimensional image from the series of 2 dimensional images.   However, CT results in 3 spatial dimensions, while chromotomography has 2 spatial and one spectral dimension.   The word chromotomography is derived from the color aspect of this form of tomography. This technique leverages work done by the medical community in the development of reconstruction algorithms. They form the basis for code AFIT uses to build the data cube [20].

2.2 CTEx Components

In its current configuration, the CTEx hardware is a laboratory prototype. A schematic of the hardware is in Figure 2.1.   It consists of an objective lens (L_1), field stop (F.S.), collimating lens (L_2), the DVP with the motor to spin it and encoder to measure its angular

5
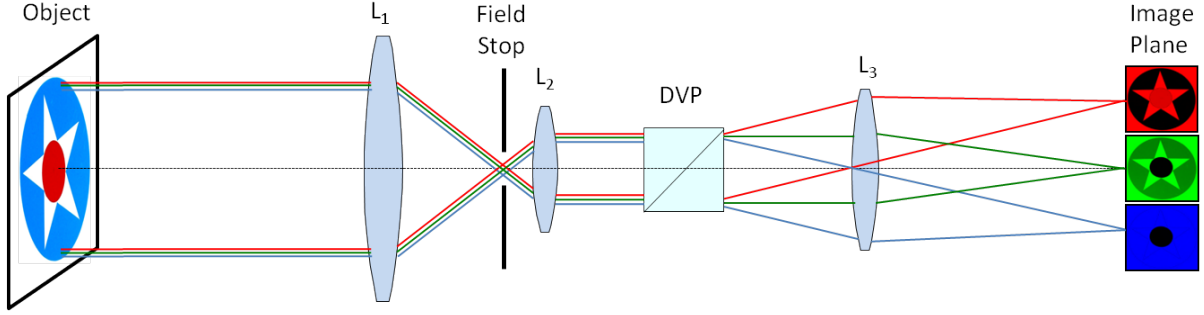
Figure 2.1: Optical layout of the CTEx system using a rotating Direct Vision Prism to vary the spectral dispersion. L_1, L_2, and L_3 are COTS lenses and F.S. is a field stop made of masking tape. The image plane was a high speed Phantom camera.

position, a focusing lens (L_3), and the FPA. L_1 had a focal length of 100 mm, L_2 was 75 mm, and L_3 was 85 mm. Further specifications are in Table 2.1. The lenses weren't

Table 2.1: Table of the lenses used in CTEx

Lens	Model	Focal Length (mm)	f/#
L_1	Zeiss Makro-Planar	100	2.0
L_2	Tamron 1A1HB	75	3.9
L_3	AF Nikkor f/1.8D	85	1.8

simple singlet lenses like shown. They were compound Commercial Off The Shelf (COTS) lenses. The field stop was a piece of masking tape with a hole cut out of it. The FPA was a high speed Phantom camera which images in the visible spectrum. In addition to the optical equipment, there are racks with encoding computers, display monitors, and power supplies, mostly developed and built by Su'e [24]. Due to the high revolution rate of the prism, the hardware was designed to reduce vibrations. Any vibrations will reduce the fidelity of the

images collected because it is impossible to know exactly where light would have struck the camera. The housing is machined from solid blocks of aluminum to minimize vibration [19]. The optical path does not contain any folding mirrors, though there is a design for such a system.

When the light strikes the objective lens, it gets focused down to a point at its focal length. Around the focused beam of light is a field stop to limit the field of view (FOV). From there, the light propagates to the collimating lens. This lens is placed so the focused point is at its focal length, ensuring a collimated beam emerges from the lens. At this point, the light enters the prism.

2.2.1 Phantom Camera.

The camera used was a high speed v5.1 Phantom camera [25]. It imaged in the visible band, which will be considered 400-800 nm in this project. Its FPA was a silicon Charge-Couple Device (CCD). Though it was visible band, it displayed in a gray-scale. The focal plane array consisted of 1024x1024 pixels. The proprietary Phantom software allowed the user to crop down the usable pixels for FOV and speed purposes. Each recording was made with only the center 512x512 pixel area. The FOV was further stopped down by a field stop to minimize vignetting seen early in the experiment. Before recording, each target was checked to ensure it fell completely within the field of view. Every model was built under the assumption that the pixels were 20 μm squares, taken from manufacturer specifications. The camera headers say the pixels are 16 μm squares, but multiple experiments confirmed the size to be 20 μm.

2.2.2 Direct Vision Prism.

The prism is 2 triangular pieces of glass adhered with optical contact bonding, which relies on intermolecular forces with no chemicals involved. Prism 1 is made of SF L6 and prism 2 is LaSF N30 (see Figure 2.2). The angle at the intersection of the two pieces causes slight, although necessary and measurable, redirection of each wavelength. This
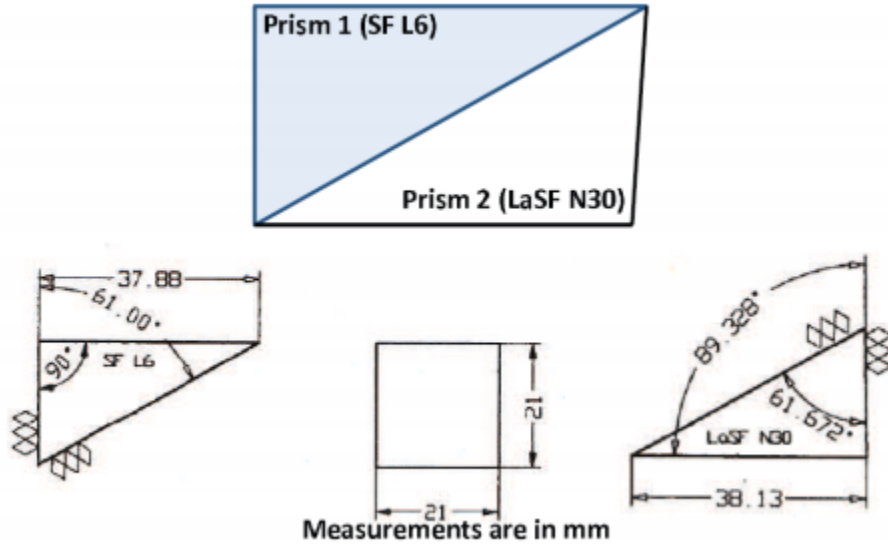
Figure 2.2: The Direct Vision Prism is made of two pieces of triangular glass optically bonded together. Figure taken from manufacturer's specification sheet.

combination of dispersing material is expected to deviate the light according to Figure 2.3 in the longitudinal direction, which will be considered the direction the prism would be expected to disperse the light. At 0.547 μm, the light is not expected to deviate at all, while it will deviate the most in the blue wavelengths. The curve gets close to linear in the reds. After passing through the prism, each wavelength is going in a slightly different angle. It strikes L_3, which brings each wavelength to a point on the FPA, located one focal length behind the lens [20][11]. They will all land in a different spot on the FPA according to

$$y(\lambda) = f_3\theta(\lambda), \tag{2.1}$$

where $y(\lambda)$ is a location on the FPA with 0 at the center, f_3 is the focal length of L_3 (85 mm), and θ is the angle of dispersion. Equation (2.1) is a small angle approximation.

8
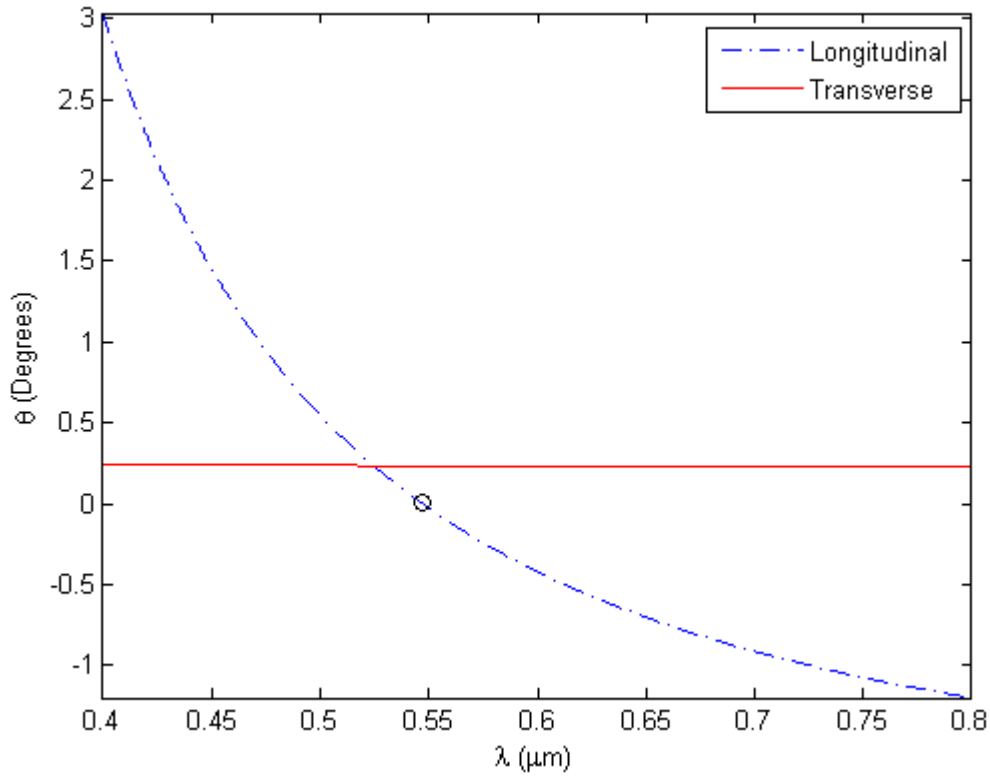
Figure 2.3: For the prism selected, the visible light is expected to disperse about 3° in the blue wavelengths and a little more than -1° in the other direction in the red. The light is not deviated at 0.547 μm. Notice the line is nearly linear in the longer wavelengths. Because of the error in manufacturing the prism, there is a transverse dispersion that is nearly constant as a function of wavelength.

In addition to the longitudinal dispersion, an error in the manufacturing of the prism introduced a transverse dispersion [20]. The two pieces of glass were optically bonded together with about 20 arcminutes of twist. The error was modeled in an optical design program called Zemax. It was small, but noticeable and affected all wavelengths. The consequence was a shift of the light in a direction perpendicular to the longitudinal shift, which has been confirmed in models and experiments [24][19]. Hence, there was no

9

truly undeviated wavelength. Even the 0.547 μm light was deviated a small amount (approximately 17 pixels on the FPA).

2.2.2.1 Calculating Dispersion.

In order to make any sense of data, the displacement of each wavelength at the FPA as a function of the rotation angle of the prism must be known. To calculate the amount of longitudinal dispersion, the Sellmeier equation (Equation (2.2)) was used to calculate the wavelength dependent indices of refraction for each piece of glass. The Sellmeier equation is

$$n(\lambda) = \sqrt{1 + \frac{K_1\lambda^2}{\lambda^2 - L_1} + \frac{K_2\lambda^2}{\lambda^2 - L_2} + \frac{K_3\lambda^2}{\lambda^2 - L_3}}, \tag{2.2}$$

where n is the wavelength dependent index of refraction, λ is the wavelength of the light in μm, and K and L were the Sellmeier coefficients in Table 2.2. The coefficients are valid in

Table 2.2: Table of the Sellmeier coefficients for the prism glass

Glass	K1	K2	K3	L1	L2	L3
SF L6	1.78	3.89E-1	1.30	8.73E-3	3.08E-2	9.28E1
LaSF N30	1.79	3.28E-1	2.02	1.35E-2	6.23E-2	1.68

the visible band. The longitudinal curve in Figure 2.3 was calculated by tracing a ray from the air through the prism and back into air using

$$n_1 \sin(\theta_1) = n_2 \sin(\theta_2), \tag{2.3}$$

called Snell's Law. It was applied at each transition between media. θ are the incident angles of the light beams with the surfaces of the glass. n_1 and n_2 are the indices of refraction for the losing and gaining media. n for air was assumed to be 1 and n for each piece of glass was calculated in Equation (2.2). θ going from the collimated light to the

first surface of the prism was assumed to be 0. The final longitudinal dispersion is give by Equation (2.4):

$$\theta(\lambda) = \sin^{-1}\{n_L(\lambda)\sin[61.672° - \sin^{-1}(\frac{n_S(\lambda)\sin(61°)}{n_L(\lambda)})] - 0.672°\}, \qquad (2.4)$$

where $n_L(\lambda)$ is the wavelength dependent index of refraction for the LaSF N30 glass and $n_S(\lambda)$ is the wavelength dependent index of refraction of SF L6. 61.672° was the apex angle of SFL6. 0.672° was the tilt angle of the back surface of LaSF N30.

The sampling for calculating the transverse offset in Zemax was for every 10 nm and only went from 400-700 nm. A data base of transverse offsets was created by interpolating the Zemax values for every 0.1 nm and extrapolating in MATLAB out to 800 nm to have a corresponding transverse angle for each longitudinal. For every wavelength, the total deviation distance on the FPA was calculated. The transverse offset was converted to a distance on the FPA according to Equation (2.1). Additionally, the distance was converted into the number of pixels by Equation (2.5) and Equation (2.6) by

$$x_{pixel}(\phi_{prism}, \lambda) = 50Y(\lambda)\sin\{\phi_{prism} - \cos^{-1}[\frac{y_{long}(\lambda)}{Y(\lambda)}]\}, \qquad (2.5)$$

$$y_{pixel}(\phi_{prism}, \lambda) = 50Y(\lambda)\cos\{\phi_{prism} - \cos^{-1}[\frac{y_{long}(\lambda)}{Y(\lambda)}]\}, \qquad (2.6)$$

where $x_{pixel}(\phi_{prism}, \lambda)$ and $y_{pixel}(\phi_{prism}, \lambda)$ are the number of pixels shifted in the x and y directions, and ϕ_{prism} is the prism rotation angle measured by the encoder. 50 is the frequency of pixels, as in 50 pixels/mm. $Y(\lambda)$ is the total deviation distance given by

$$Y(\lambda) = \sqrt{y_{long}(\lambda)^2 + y_{trans}(\lambda)^2}, \qquad (2.7)$$

where $y_{long}(\lambda)$ is the longitudinal dispersion distance and $y_{trans}(\lambda)$ is the transverse dispersion distance. A graphical depiction of Equation (2.5) and Equation (2.6) is in Figure 2.4. A look-up table of pixel deviations in the x and y directions as functions of wavelength and prism rotation angle was created for reference by the reconstruction algorithms.
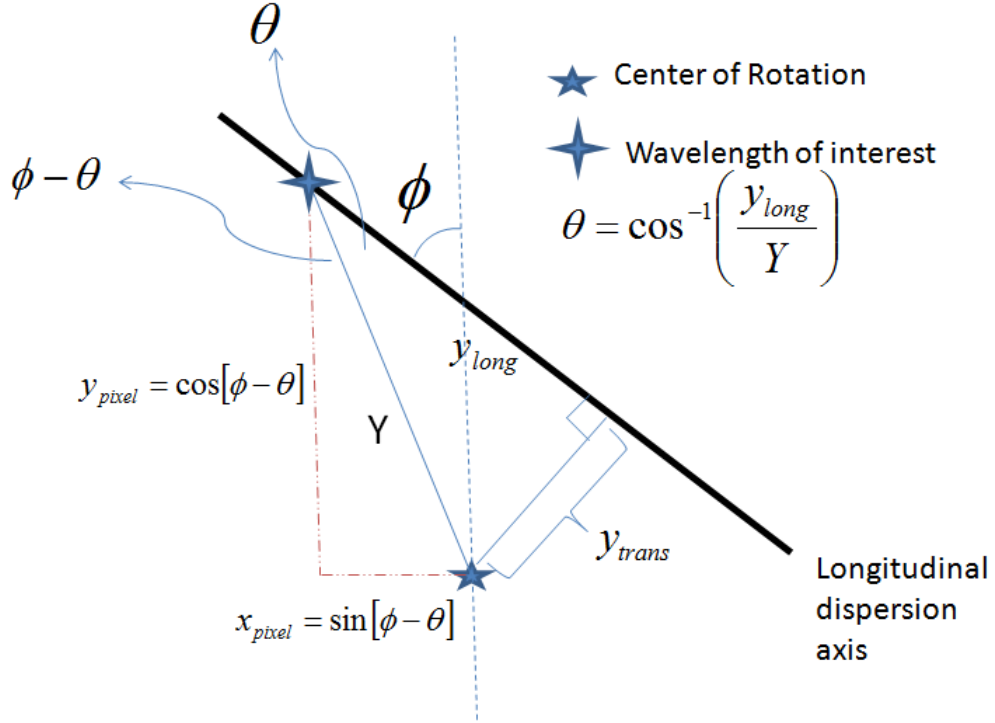
Figure 2.4: A graphical depiction of Equation (2.5) and Equation (2.6) is in Figure 2.4. It shows how the algorithms convert the location of light based on prism rotation angle and wavelength into x and y pixel deviations.

2.3   Reconstruction Algorithms

Although classification of the various reconstruction algorithms proposed in literature will not be a main thrust of this thesis, there is value in going over the basic aspects of how they work. The first thing the algorithm must do is decide where a given wavelength will be located on the FPA. 547 nm was expected to pass through the CTEx optical system undeviated, and every other wavelength dispersed along a line. The algorithm looked in this pre-determined spot (based on encoder angle) on the FPA to form a slice of the hypercube. No matter how the prism was rotated, the deviation should be the same number of pixels relative to a center spot. That center spot was the nominal location of the object when the

prism was removed. Each of the reconstruction algorithms discussed in this section were written in MATLAB.

2.3.1 On- and Off-wavelength Reconstructions and Artifacts.

References to both on- and off-wavelength reconstructions will be made throughout this document. An on-wavelength reconstruction is one corresponding to a wavelength that was present in the spectrum of the scene. For example, the 546 nm slice of the hypercube in a Mercury spectrum is considered on-wavelength. 500 nm would be off-wavelength. If more than 1 emission is present in any scene, artifacts will always be present in every slice of the hypercube. Artifacts are spectral and spatial information for any wavelength other than the on-wavelength light. As a result of the reconstruction algorithms to be discussed later in this section, they take the form of circles or halos about a certain point. Artifacts are not desirable as they affect the proper interpretation of what happens in a scene at a specific location and wavelength. They can be seen in Figure 2.5.

2.3.2 Shift and Add (Backprojection).

The shift and add technique is the simplest algorithm both conceptually and mathematically. It converts raw CTEx data into a usable hypercube. Its principles form the basis of all other reconstructions discussed here. The algorithm first determines the prism's rotation angle for a given frame. That information is contained in a text file written by the encoder. The encoder measures the angle at the beginning and end of each video frame. The angle chosen is the average of the start and stop angle. Based on this angle, the algorithm shifts every pixel in the frame by the opposite of the expected total dispersion discussed above according to the wavelength chosen for reconstruction. For instance, consider the "undeviated" 547 nm being reconstructed, and the angle of rotation was 90° for a given frame. The total dispersion would move the light 17 pixels to the right. The algorithm would then write a new frame with every pixel shifted 17 pixels to the left. Any light of 547 nm would nominally be in the location it would have been had the prism been removed.

The same thing would happen to every other frame (each at a different angle) in the scene. After everything has been shifted according to angle, the frames are added together. The result is an accurate spatial image of the light at that wavelength. This process is repeated for every wavelength in the band to form the hypercube. Any off-wavelength light is in the form of dimmer artifacts or halos, which form circles around the center of reconstruction. They should be visible, but considerably dimmer than the on-wavelength light because they have not been added on top of each other as many times as the on-wavelength. A visual depiction of the process can be seen in Figure 2.5, borrowed from O'Dell [20].
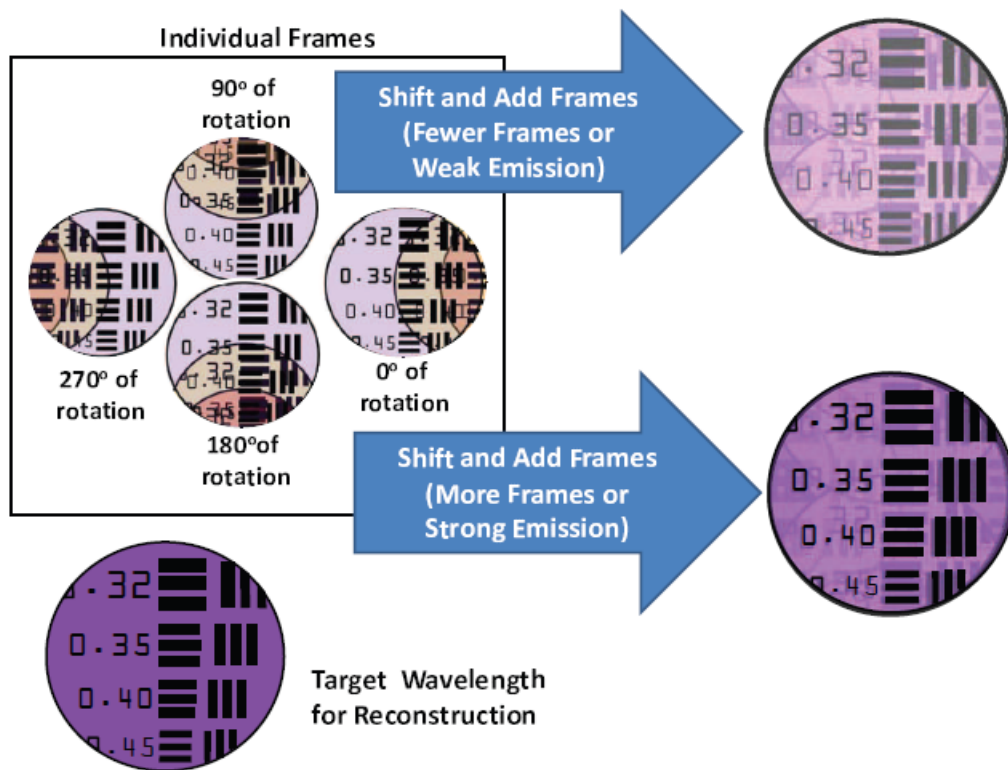
Figure 2.5: A visual representation of the shift and add technique. The top right shows how the artifacts might diminish the quality of the reconstruction. Image from O'Dell [20].

More frames used in reconstruction dims out the artifacts the most. Artifacts will cause

problems if they aren't considerably washed out. This new shifted and added frame would be marked with the wavelength and placed as a layer in the hypercube. The entire process would happen again to the raw video frames for every wavelength in a band selected by the user to create the whole hypercube.

2.3.3 System Transfer Function.

A System Transfer Function (STF) is common to all chromotomography reconstructions in literature. It is a matrix that contains the location of each spectral Point Spread Function (PSF) created by the prism. Mooney shows in [18] that the projections, or raw data on the FPA denoted as $g(x, y, \phi)$, can be modeled by convolving the hypercube $f(x, y, \lambda)$ with the PSF of the system with respect to λ by

$$g(x, y, \phi) = \int_{-\infty}^{\infty} f(x, y, \lambda) * * \delta(x - k(\lambda)cos(\phi), y - k(\lambda)sin(\phi))d\lambda, \tag{2.8}$$

where x and y are the pixel coordinates. ϕ is the prism angle, and $k(\lambda)$ is the radial shift from the center of the FPA, or the spectrometer constant. Referencing Mooney in [18], Deming [8] more succinctly writes Equation (2.8) as

$$g(\overline{x}, \phi) = \int_{-\infty}^{\infty} f(\overline{x} - k(\lambda)\overline{p}_{\phi}, \lambda)d\lambda, \tag{2.9}$$

where $\overline{x} = (x, y)$ and $\overline{p}_{\phi} = (cos(\phi), sin(\phi))$. Deming further takes a 2D Fourier transform to change the convolution to multiplication [8] by

$$G(\overline{\xi}, \phi) = \int_{-\infty}^{\infty} \exp[-2\pi k(\lambda)\overline{\xi} \cdot \overline{p}_{\phi}]F(\overline{\xi}, \lambda)d\lambda, \tag{2.10}$$

where $\overline{\xi}$ is the transformed coordinates drawn from $\overline{x}$. It can also be written as (ξ_1, ξ_2). $\overline{\xi} \cdot \overline{p}_{\phi}$ is the vector dot product. Capital letters represent the transformed functions of the corresponding lower-case letters. Since the data cube is sampled at discrete wavelengths and not a continuous spectrum, Mooney and Deming represent Equation (2.10) as a summation rather than an integral:

$$G_m(\overline{\xi}) = \sum_{n=0}^{N-1} \exp[-2\pi n\overline{\xi} \cdot \overline{p}_m]F_n(\overline{\xi}, \lambda)\Delta\lambda, \tag{2.11}$$

15

where m is a discrete projection, n is a discrete spectral band, $\overline{p}_m = [cos(\frac{2\pi m}{M}), sin(\frac{2\pi m}{M})]$ for M projections, $0 \leq m \leq M$, and $n = k(\lambda)$ for the N spectral bands used. In this Fourier space and following from Equation (2.10), the spatial frequencies of the projections and the actual image cube are related by

$$G(\overline{\xi}) = A(\overline{\xi})F(\overline{\xi}). \tag{2.12}$$

$A(\overline{\xi})$ is an MxN matrix and is the System Transfer Function. Its elements are

$$A_{m,n}(\overline{\xi}) = \exp[-2\pi n\overline{\xi} \cdot \overline{p}_m]. \tag{2.13}$$

$F(\overline{\xi})$ is found by inverting $A(\overline{\xi})$ and multiplying it on both sides. Finally, $f(x, y, \lambda)$ is found by a 2-D inverse Fourier transform of $F(\overline{\xi})$.

2.3.4 Backprojection then Filtering.

Other algorithms exist that rely on a series of matrix inversions utilizing SVD [18]. Matrix inversions are computationally expensive, and it is not always possible to find the inverse of a matrix. Instead of using the simple shift and add technique, researchers have borrowed algorithms from the medical field's CT. One such method applies a spatial filter to the dispersed data and projects the image backwards through the prism [4]. Another backprojects the image first and then filters it according to λ [8]. The methods used in this project used backprojection first, both with and without the filter, because of the computational efficiency, and to leverage code previously developed at AFIT. It is technically called *backprojection then filtering*, but will often be referred to as *filtered backprojection*. All Fourier calculations were performed with MATLAB's efficient *fft, ifft, fft2, and ifft2* commands. To reiterate, Deming shows the raw projection $g(x, y, \phi)$ is 2D Fourier transformed into $G(\overline{\xi}, \phi)$ by

$$G(\overline{\xi}, \phi) = DFT[g(x, y, \phi)] \cong \int_{-\infty}^{\infty} \int_{-\infty}^{\infty} g(x, y, \phi) \exp[-2\pi i(\xi_1 x + \xi_2 y)]dxdy, \tag{2.14}$$

where $G(\overline{\xi}, \phi) = G(\xi_1, \xi_2, \phi)$, and DFT is a discrete Fourier transform. Then, the unfiltered Fourier cube, $F'(\overline{\xi}, \lambda)$ is computed by backprojecting the data cube, $G(\overline{\xi}, \phi)$ with the

Hermitian adjoint of $A(\bar{\xi})$ from Equation (2.13) by

$$F'(\bar{\xi}, \lambda) = [A^H G](\bar{\xi}, \lambda) = \int_0^{2\pi} \exp[2\pi i k(\lambda)\bar{\xi} \cdot \overline{p}_\phi] G(\bar{\xi}, \phi) d\phi, \qquad (2.15)$$

which is the process of backprojection. Next, the spectral filter must be calculated and applied to the unfiltered Fourier cube. Deming further defines the spectral filter as, $\widetilde{M}(\bar{\xi}, \omega_\lambda)$. It is a zero-order Bessel function that has been 1D Fourier transformed with respect to λ, and is simplified to

$$\widetilde{M}(\bar{\xi}, \omega_\lambda) = \int_{-\infty}^{\infty} 2\pi \exp(-2\pi i \omega_\lambda \lambda) J_0(2\pi k \xi_r \lambda) d\lambda = 2(k^2 \xi_r^2 - \omega_\lambda^2)^{-1/2}, \qquad (2.16)$$

where $\xi_r = (\xi_1^2 + \xi_2^2)^{1/2}$, and k is the spectrometer constant that depends on the angle of dispersion of the light. ω_λ is also written as ζ, and is the spectral frequency (not to be confused with ν, the frequency of a photon). The filtered Fourier cube $\widetilde{F}_\mu(\bar{\xi}, \omega_\lambda)$ is obtained by 1D Fourier transforming Equation (2.15) with respect to λ to make it $\widetilde{F}'(\bar{\xi}, \omega_\lambda)$ and applying Equation (2.16) by

$$\widetilde{F}_\mu(\bar{\xi}, \omega_\lambda) = \frac{\widetilde{F}'(\bar{\xi}, \omega_\lambda)}{\mu + \widetilde{M}(\bar{\xi}, \omega_\lambda)}, \qquad (2.17)$$

where μ is chosen based on the noise level in the data. If there is no noise, $\mu = 0$. Typical values in this project were arbitrarily chosen between 1 and 10, with 5 being the most common. The full importance of μ was not investigated in this project. Lastly, Deming shows $\widetilde{F}_\mu(\bar{\xi}, \omega_\lambda)$ is 1D inverse Fourier transformed with respect to ω_λ by

$$F(\bar{\xi}, \lambda) = \frac{1}{2\pi} \int_0^{2\pi} \widetilde{F}_\mu(\bar{\xi}, \omega_\lambda) \exp[2\pi i(\xi_1 x + \xi_2 y)] d\omega_\lambda \qquad (2.18)$$

to get the final filtered Fourier cube and 2D inverse Fourier transformed with respect to x and y to get the filtered cube in real space, $f(x, y, \lambda)$. The backprojection without the filter applied, also called unfiltered backprojection or just backprojection, was compared to the simple shift-and-add. Virtually no difference was found in the final product of the reconstruction between the two. Since shift-and-add was much more simple by not

requiring any Fourier transforms, it completed its calculations up to 3 times faster than backprojection with Equation (2.15). Despite this, backprojection was used throughout this project. The filter was applied in Fourier space, so it was impossible to do with just the shift-and-add algorithm. Because most cases were investigated with and without the filter, it was easier to stick with one algorithm instead of switching back and forth based on the scenario. The shift-and-add algorithm was described to show the basis of every other chromotomographic reconstruction.

2.3.5 *Fourier Principles, the Central Slice Theorem, and the Cone of Missing Information.*

Since the collected data has spatial and spectral information interlaced, a reconstruction algorithm is required to deconvolve them from each other. A deconvolution involves separating the spatial and spectral information with Fourier transforms. According to the central slice theorem, "the Fourier transform of a parallel (collimated) projection of an object at an angle equals a line through the center of the 2D Fourier transform taken at the same angle" [12]. The central slice theorem can be extended into the hypercube geometry: "the 2D Fourier transform of a parallel projection at an angle equals a plain through the center of the 3D Fourier transform at that same angle." By rotating the prism, a series of different slices through the origin are obtained, all at the same angle relative to the normal. In the limit that an infinite number of projections are taken, the missing area forms a cone whose half-angle is equal to the angle of the original lines. This is known as the cone of missing information [13][24]. A graphical representation of the cone is seen in Figure 2.6. A clearer image of just the cone is in Figure 2.7. The area within these lines in frequency

space must be filled in by the reconstruction algorithm to complete the hypercube. Brodzik [7] describes a method of Projections Onto Convex Sets (POCS) that attempts to do this.

Since all of the data in this project underwent projections, they were all affected by the cone. At $\zeta = 0$, which was 0 spectral frequency (the Fourier transform with respect to λ),

18
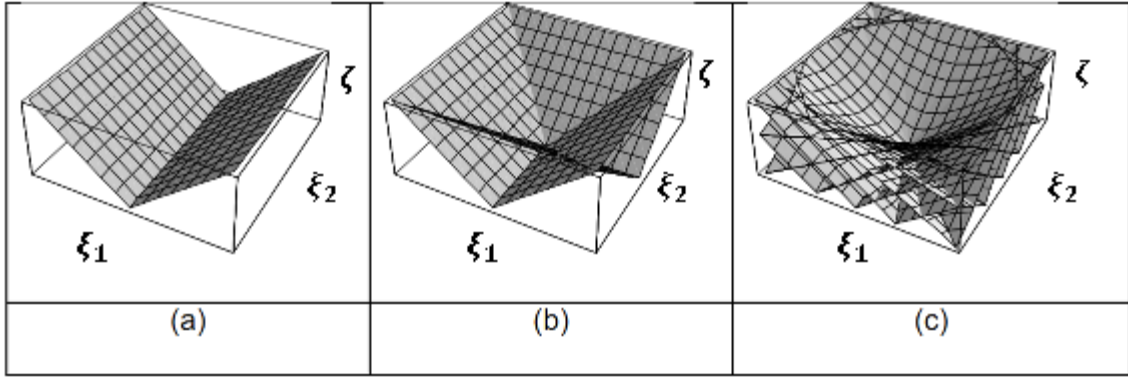
Figure 2.6: A visualization of the cone of missing information. Each projection is a 2D plane through the 3D Fourier cube (ξ_1, ξ_2, ζ). As the number of projections increases, the shape of the cone becomes more defined [6].
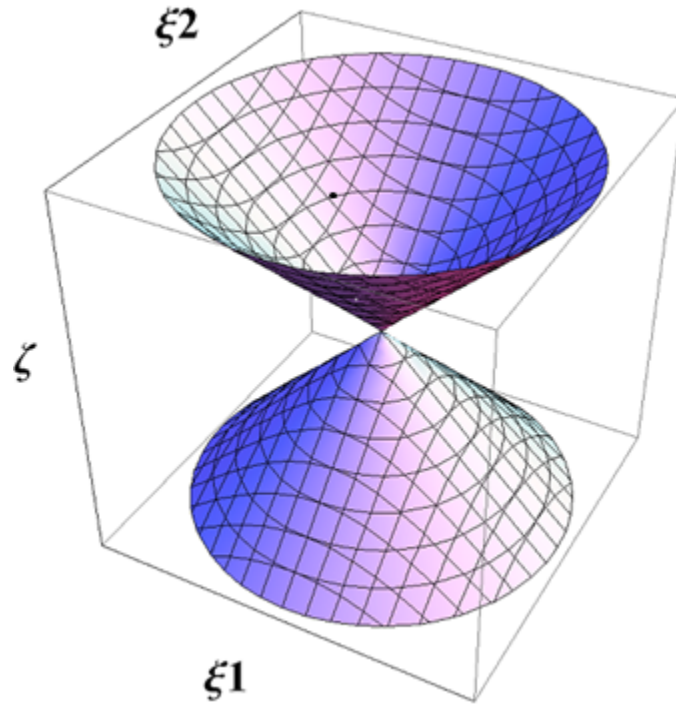
Figure 2.7: A clear depiction of the cone of missing information.

none of the spatial or spectral frequencies are lost; the radius of the cone is 0 at that point. As the magnitude of ζ increases, low magnitude spatial frequency data is lost in the cone. Additionally, more of the high ζ values are also lost. In Fourier space, high frequencies make up sharp edges of a real signal. Low frequencies correspond to energy and fill in the spaces in between sharp edges.

There is another area inside the cube that is not filled in. Because of the finite number of prism angles in any real system, there is a finite number of projection planes in the cube that form the cone. Therefore, the entire space of the cone is not represented by all of the planes. While the low spatial frequencies are well sampled, the higher spatial frequencies aren't represented as well. This is called the *limited angle* problem in chromotomography [17]. Some method of enhancing the higher spatial frequencies is required to make up for the under-sampling, which is what the filtered backprojection attempts to do. It is a high spatial frequency enhancer.

2.3.6   *Chromatic Aberration and Distortion.*

Because only refractive optics were used (as opposed to folding mirrors), chromatic aberrations must be considered. The focal length f of a lens depends on its index of refraction n. When n is constant, f is the same for every color of light. According to Equation (2.2), n is wavelength dependent, so f is a function of wavelength and becomes $f(\lambda)$. That means every color will focus at a slightly different distance behind L_3. Only one color of light can be in focus at a time. This is called chromatic aberration. If a broad-band source, such as white light, were to be imaged by the system, the blue light may be in focus while the red light is out of focus. This is shown in Figure 2.8.   The defocus causes the light to spread out over a larger area of pixels instead of being nice and sharp. It also lowers the peak intensity. Commercial lenses are engineered to reduce this effect, but it was still seen in this project.
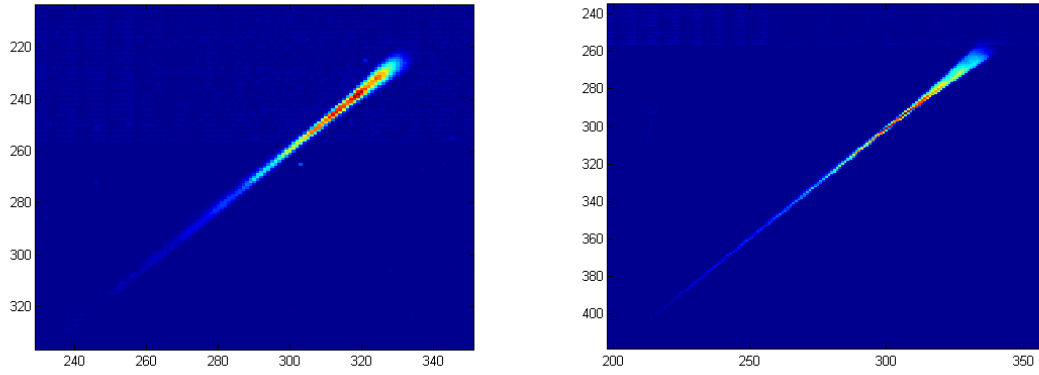
Figure 2.8: (L) A raw image of a white light source with a long wavelength in focus. (R) A raw image of a white light source with a short wavelength in focus. The long wavelength light is in the top right. When it is in focus, it is sharper than it was out of focus.

Distortion is considered a monochromatic aberration. It arises when each area of a lens has different focal lengths and transverse magnifications. Instead of being a function of wavelength, it is a function of off-axis image distance. Distortion can be seen as affecting the image like a pincushion (positive distortion) or a barrel (negative distortion). In pincushion distortion, images further from the optical axis are stretched even further from it. Similarly, negative distortion bring further images closer to the axis. In either effect, those images furthest from the optical axis are affected the greatest [11]. If distortion is present in the system, wavelength reconstructions would be least accurate at those wavelengths further spectrally from the undeviated. Even compound lenses can be affected by distortion.

2.3.6.1 *Experimental Evaluation.*

Even though commercial compound lenses are engineered to minimize chromatic aberration [11], it apparently still exists in this system. Because of it, many wavelengths were out of focus. That caused the light patterns to spread out in all directions more than

they would have been had they been in focus. An example of this is shown at the bottom of the halo in Figure 2.9. This is a zoomed in view of the 400 nm slice of a Mercury pen
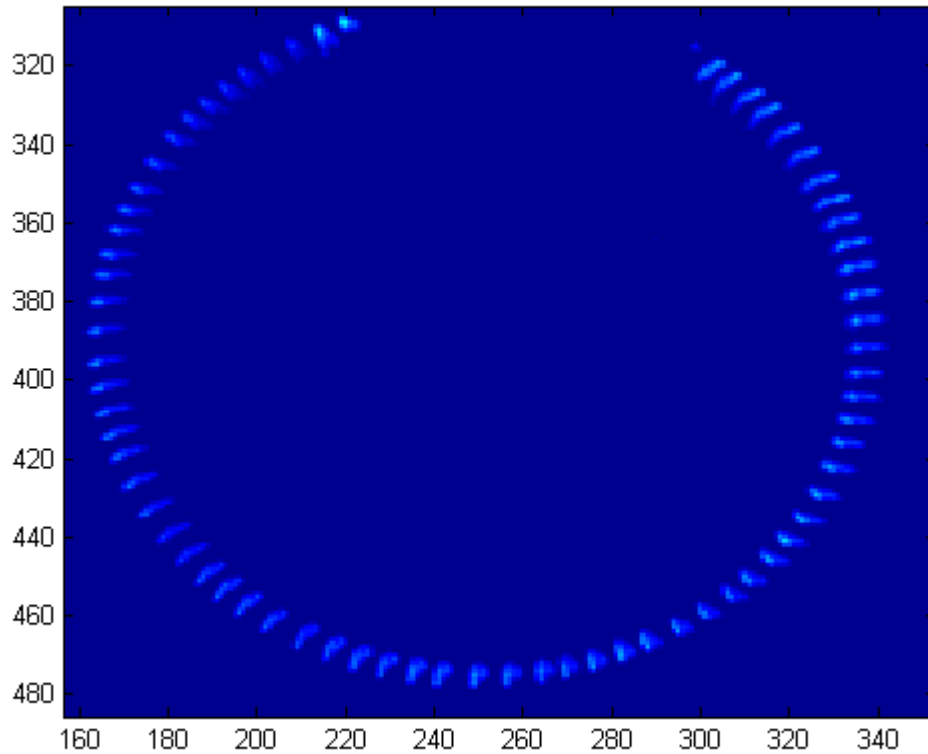
Figure 2.9: The 400 nm reconstruction of a Mercury pen lamp to investigate the effects of chromatic aberration and dispersion of a short wavelength. The light is from the 435 nm emission. Since the light was smeared in circular spots (bottom of halo) and in the radial direction (left and right sides), both prevented the light from forming nice tight spots.

lamp with the focus adjusted to minimize the 546 nm spot size. The area shown is the halo of the 435 nm emission. Since the energy there was spread out in a quasi-circular spot, it entered the region of reconstruction at a shorter wavelength and left it at a longer one than expected. The spectrum in Figure 4.5 then showed the emission to be more broad. Due to

the conservation of energy, the overall intensity of the light remained the same. Since it was divided over more pixels, the peak intensities were lowered.

While chromatic aberration played a role in reshaping an emission on the FPA, the far right and left areas of Figure 2.9 suggest another phenomenon also contributed. Recall the longitudinal dispersion caused the light to spread in the radial direction of the halo. Instead of spreading the light in a circular spot, it was spread along the longitudinal dispersion axis. This indicates that even though the line width of a pen lamp emission is very low, the extremely steep dispersion curve in the blue wavelengths caused that light to spread. The line at the (x,y) pixel location of (170, 380) was approximately 8 pixels in the radial direction. By converting the pixels to a distance on the FPA, converting it to an angle by Equation (2.1), and dividing by the slope of the dispersion curve at 435 nm, this would indicate the bandwidth of the emission was 3.6 nm. Note this effect is much more pronounced in the shorter wavelengths than the long because of the dispersion curve in Figure 2.3. The independent measurement's width at that wavelength was between 0.6-0.8 nm. While the actual bandwidth of the line is much smaller [1], dispersion and chromatic aberration likely contributed to the misshaped spots. These effects will collectively be called chromatic aberrations in this document. If a wavelength is said to be "in focus", it means focus was adjusted to minimize the spot size at that wavelength.

III.   Methodology

This thesis project only used the unfiltered and filtered backprojection algorithms to reconstruct the Chromotomography Experiment data. The algorithm was proposed by Deming [8] and written by Su'e [24]. It was modified to handle the specific problems addressed in this project. Once the filtered and unfiltered hypercubes were built, techniques were developed to assess image quality. These techniques were written to build a pseudo-spectrum out of the cube. In traditional hyperspectral imaging, spectra are normally built by measuring intensities for a single pixel along the λ axis of a hypercube [9]. Often times, the artifacts caused this method to yield a measured spectrum that looked nothing like the true spectrum. An alternate method was required. Instead of measuring the spectrum in the traditional way, several alternative methods were developed to create a "pseudo-spectrum." A reconstruction was considered better the more the pseudo-spectrum looked like an independently measured truth spectrum. Unless referring to a truth or theoretical spectrum, anything deemed a spectrum in this document is really a pseudo-spectrum.

3.1   Testing the Reconstruction Algorithm

The spectral lines of all radiating sources have finite widths, affected by random thermal motion, atomic collisions, and the finite size of light waves [3]. Gases like Neon and Mercury have well-characterized wavelength emissions which emit extremely narrow spectral lines. Pen lamps which contain gases of these elements have line widths on the order of 10^{-3} nm. This is very narrow compared to the data from most spectrometers [1]. If a pen lamp is placed behind a pinhole and imaged, it simulated a point source with spectral delta functions at its emission wavelengths. Some spectral emission lines of Mercury and Neon pen lamps are listed in Table 3.1.

Table 3.1: Table of Mercury and Neon pen lamp emission lines and normalized intensities [23]. Each element's intensities were independently normalized so the maximum in the set was 1.

Hg Lines (nm)	Ne Lines (nm)	Normalized Relative Intensity
435.8	-	1.0000
546.1	-	0.8704
577.0	-	0.0796
579.1	-	0.2963
-	594.5	0.1183
-	609.6	0.1935
-	614.3	0.3333
-	626.6	0.1613
-	633.4	0.2151
-	638.3	0.2366
-	640.2	1.0000
-	650.7	0.3978
-	667.8	0.5376
-	671.7	0.1398
-	692.9	0.2043
-	703.2	0.3011
-	724.5	0.1075
-	743.9	0.0269
-	753.6	0.0204

The reconstruction algorithms in this project had never been used to build real, complex laboratory data on this specific system; they were only used on point sources and simulated data. To test whether or not they were viable, a simple case was investigated. The Air Force bar chart (Figure 3.1) was illuminated with a Mercury pen lamp. The numbers
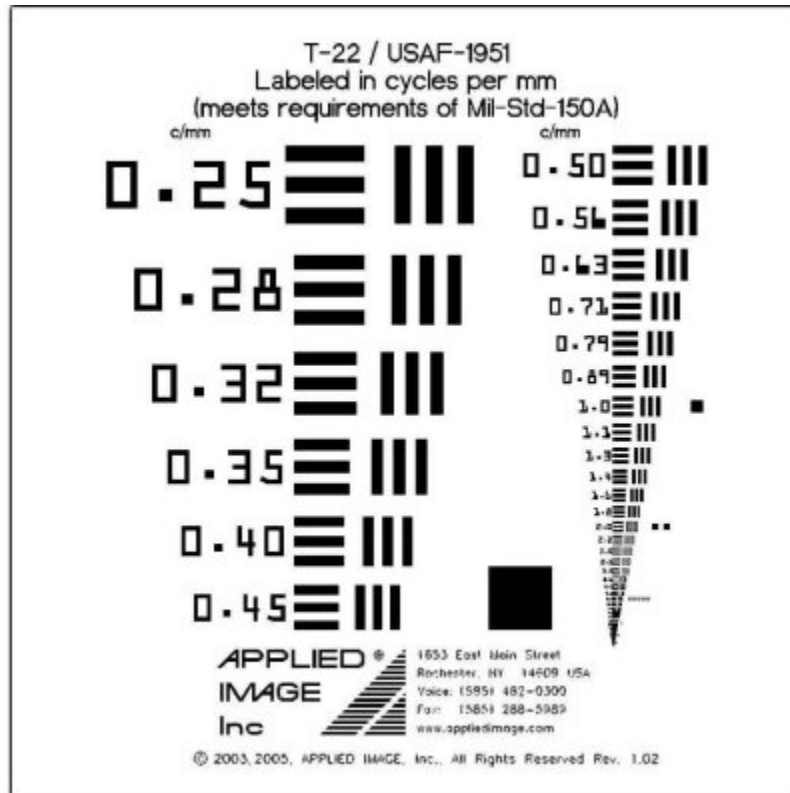
Figure 3.1: The Air Force bar chart. Its simple structure and selection of spatial frequencies make it ideal for imaging a scene with simple spatial complexity.

next to the bars are the spatial frequencies of those bars in terms of cycles/mm. The algorithms were applied to the raw data and each slice in the hypercube was investigated. When the reconstructed images near the 546 nm Mercury line looked like the scene by inspection, the algorithms worked.

3.2   Building Spectra

Hyperspectral imagers are imaging spectrometers - they record an image of a scene and measure the spectrum of each pixel. Normally, the intensity of a single pixel is measured along the λ axis in the real hypercube and plotted as a function of wavelength. If the pixel contained only light from a Neon source, it would have peaks consistent with Table 3.1 and 0 everywhere else. In the CTEx hypercubes built in this project, this method did not work. The artifacts, especially in a complex scene, caused intensities to be distributed throughout the spatial scene, even in the off-wavelength slices. An example of this plot is in Figure 3.2.   The spectrum was measured by taking the intensity of a pixel of white space in the Air Force bar chart illuminated by the Mercury pen lamp through the hypercube. The pixel was near the center of the field of view. In order to rectify this, other methods to build the spectra were devised. Since the techniques were different from the accepted way to measure HSI spectra, they were actually pseudo-spectra and not real. They were tools, however, to assess image quality. When a pseudo-spectrum looked like an independently measured spectrum, it was classified as good. The more it resembled the real spectrum, the better it was.

Each of the spectrum building techniques assumed that on-wavelength images had the highest intensities and sharpest contrast throughout the hypercube. The closer an off-wavelength reconstruction was to a wavelength present in the scene gave it higher intensities and sharper contrast than those further. The techniques were developed to give the on-wavelength slices maximum values. The more an image looked like the actual scene, the higher value it was given. The goal was to create pseudo-spectra that looked like the real spectra.

3.2.1   Mean Intensity.

The easiest way to build a spectrum from reconstructed images is to measure the mean intensity in a region of the scene and plot it versus the reconstructed wavelength. For an
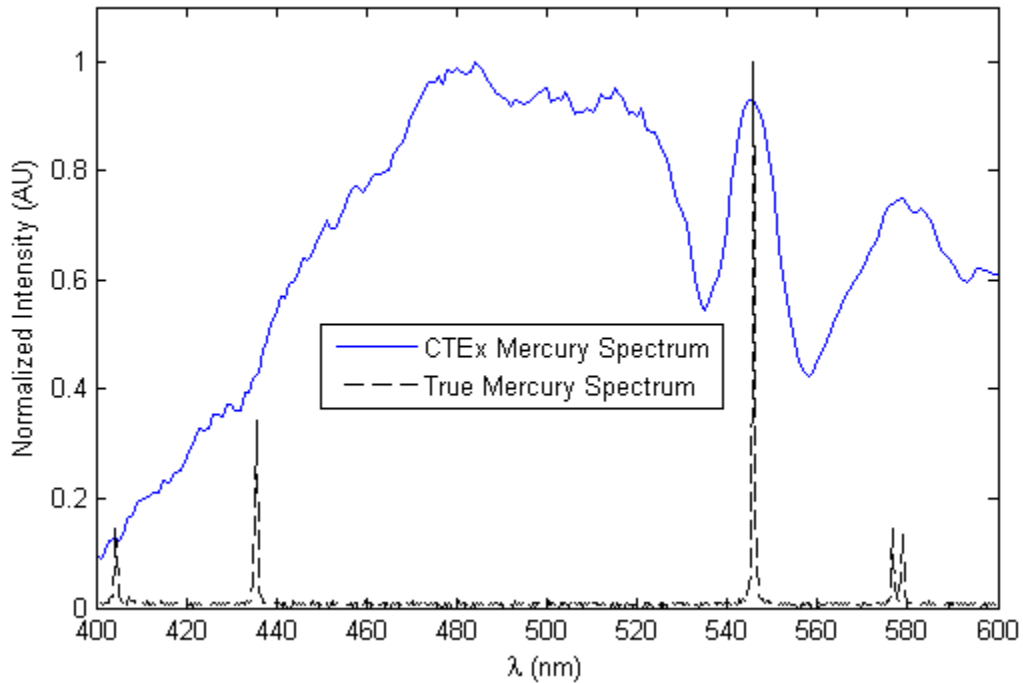
Figure 3.2: A comparison of the CTEx Mercury spectrum built with regular HSI methods vs a Mercury spectrum measured with an independent spectrometer. It was built by measuring the intensities of a pixel of white space in the Air Force bar chart illuminated by a Mercury pen lamp. It matched spectral peaks at 546 and 578 nm. The large intensities between 450 and 520 nm were from artifacts in reconstruction.

on-wavelength layer in the hypercube, every pixel with that wavelength should be more intense than it is in other layers because because each of the projections had been added on top of each other from backprojection. Therefore, if a region of those pixels is isolated and the intensities are averaged (Figure 3.3), the best reconstructions should yield the highest values. Repeating this process layer by layer will have maximum intensities on wavelength

and minimum intensities where there is no good reconstruction. The resulting plot should closely resemble the spectrum of the scene.
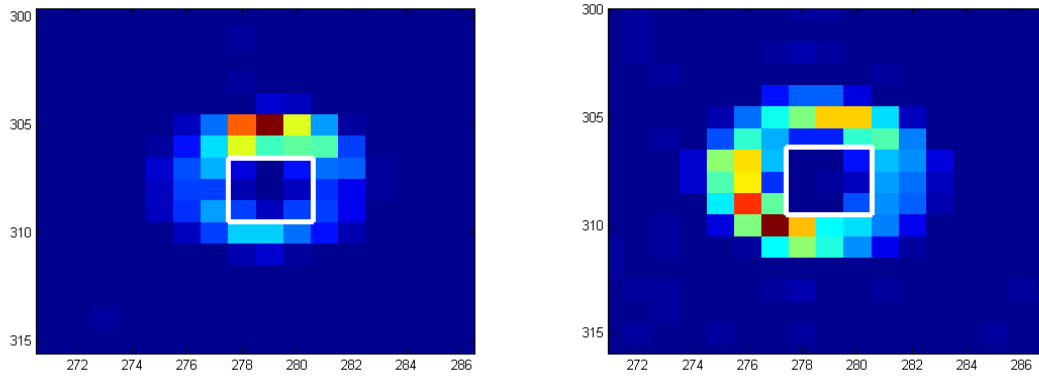
Figure 3.3: (L) Off-wavelength reconstruction of a light from a pinhole entering the area used to build a spectrum. (R) Off-wavelength reconstruction of a light from a pinhole exiting the area used to build a spectrum. The areas used to build the pseudo-spectrum are boxed in by the white rectangles.

This process is best suited for finding the spectrum of a true point source or of a single pixel. Each color of the light would only image to 1 pixel on the FPA. The on-wavelength reconstructions will have a single pixel at the center of the image and be dark in the areas between points and halos. If the region selected for averaging intensities is the single pixel, the highest intensities will be delta functions. If the region is a small area around the center pixel, the spectral lines will have some width to them.

If the region selected for averaging has a lot of dark space in it, like in the bars on the Air Force bar chart, the mean intensity can be artificially low. The areas that contain spectral information will contribute to a high mean intensity, but the dark spaces bring down the average in an on-wavelength reconstruction. In that same region, an off-wavelength reconstruction with a lot of artifacts might produce a high mean intensity and show spectral information where there should be none.

3.2.2 Edge Technique.

When a scene has sharply defined features, like in Figure 3.1, its edges can indicate a quality reconstruction. MATLAB code for this technique was written to quantify the sharpness of the edges. In this method, the user indicates the boundaries of the objects with sharp edges based *a priori* knowledge. The code then uses MATLAB's edge command, which uses a sobel filter, on the first reconstructed image in the cube. The command assigns either a 1 or a 0 on each pixel in the range depending on whether or not it contains an edge. The user can define in the code a threshold or use MATLAB's default value when determining an edge. The code then sums all of the binary values in the range to serve as the intensity value. An example of the edge technique used on the bar chart is in Figure 3.4. The region of interest was narrowed down from the entire chart to what was displayed.

All of the red pixels met the threshold defined as an edge and assigned values of 1. The blue pixels were assigned 0. The sharper, better reconstructed images should have more edges, resulting in higher "intensities." If accurate, the plot will look like the spectrum of the scene.

3.2.3 Gradient Technique.

Another way to build a spectrum from a chromotomographic data set is to measure the change in features of the image. MATLAB has a command that will find the direction and magnitude of the spatial gradient in each pixel. Code was written to take advantage of this method. Again, the user can specify where in the image a target is located. The code scans over the area and forms a matrix with the magnitude of the pixels' gradients, seen in Figure 3.5. Each pixel is transferred into a binary matrix as a 1 if its magnitude meets a user defined threshold and a 0 if it does not. If the angles of an edge are known, the user can also specify the direction of the gradient. When a reconstructed image is sharp, the change between an object and a background should be high, leading to higher gradient counts. The
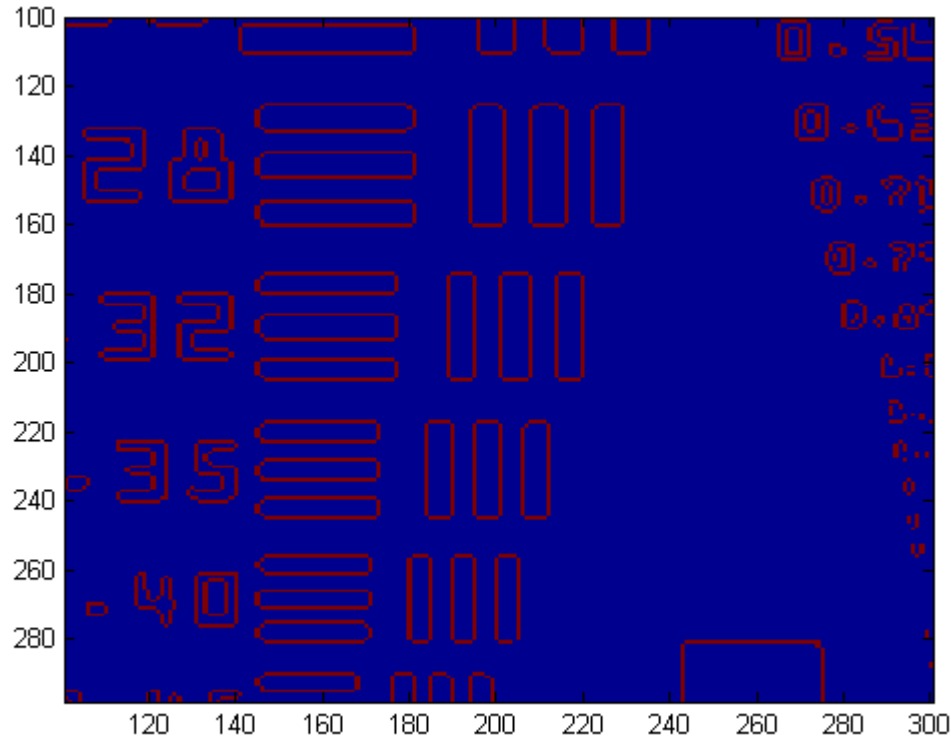
Figure 3.4: The edge technique on a section of the Air Force bar chart. Red pixels met the edge threshold and blue did not.

code sums the values and stores them as "intensities" again. It plots the intensities, which should be highest on a reconstruction of a wavelength that is present in the image.

3.2.4   Mean Absolute Error Technique.

The Mean Absolute Error (MAE) Technique compares a reconstructed image to an independent, pristine truth image. Like the other techniques, it relies solely on spatial image quality to build a spectrum. The truth image must have an identical FOV as the reconstructed image. For this demonstration, the truth image was obtained by placing a 500 nm long pass and a 550 nm short pass filter in front of the prism. The scene was then illuminated by a Mercury pen lamp. The filter ensured that only the 546 nm light

31
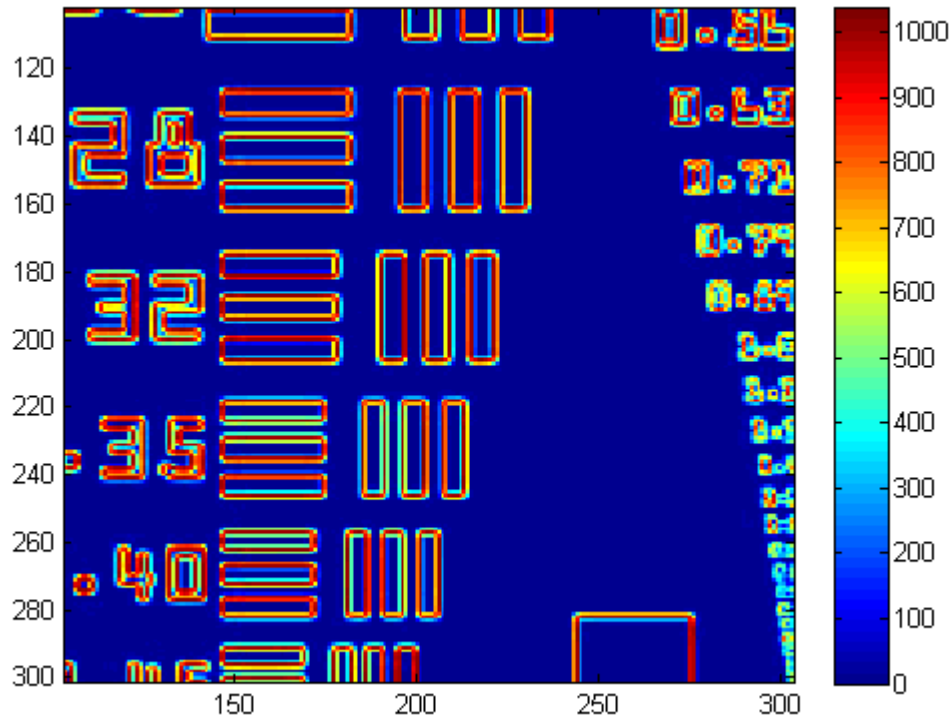
Figure 3.5: The gradient technique on a section of the Air Force bar chart. The scale is a measure of the magnitude of the gradient of each pixel.

from the lamp made it to the camera. The image was reconstructed for wavelengths in the neighborhood of 546 nm, and the spectral layers were examined. The best visual reconstruction was selected as the truth image. In an alternative method, the prism was removed and the reconstruction step was eliminated. That method was time consuming, and it increased the risk of moving the camera, changing the field of view.

After the truth image had been established, the filters were removed or the prism replaced. Without moving the target, more video was recorded while the prism spun, then it was reconstructed. Each reconstruction and the truth image was cropped so only the target in the scene remained. The difference in intensities of each pixel in both images were

calculated and squared to make every value positive. The square roots of the values were added together and catalogued by wavelength. Because an on wavelength reconstruction should look the most like the truth image, its MAE should be the lowest. Therefore, the inverse of the sums of the square roots were plotted so the better reconstructions had higher values and looked like spectra.

3.2.5 *Cross Correlation Technique.*

Another way to compare the similarity of 2 images is to cross correlate them [26]. In order to correlate 2 images $f_1(x, y)$ and $f_2(x, y)$, a 2 dimensional Fourier Transform is performed on each image by Equation (2.14), or more appropriately for real images, with a 2D discrete Fourier Transform by

$$\mathcal{F}_{1,2}\{\xi_1, \xi_2\} = \sum_{y=0}^{N-1} \sum_{x=0}^{M-1} f_{1,2}(x, y) \exp[-2\pi i(\frac{\xi_1 x}{M} + \frac{\xi_2 y}{N})], \tag{3.1}$$

where x and y are the spatial variables, ξ_1 and ξ_2 are the frequency variables, and N and M are the numbers of pixels on the FPAin the x and y directions, respectively [26]. The transformed images are then multiplied together. An inverse Fourier Transform is then performed on the product by

$$h(x, y) = \frac{1}{MN} \sum_{y=0}^{N-1} \sum_{x=0}^{M-1} \mathcal{F}_1\{\xi_1, \xi_2\}\mathcal{F}_2\{\xi_1, \xi_2\} \exp[2\pi i(\frac{\xi_1 x}{M} + \frac{\xi_2 y}{N})], \tag{3.2}$$

with $h(x, y)$ as the result of the cross correlation. The correlation is a measure of the overlap of the two images. When they are more similar, they will overlap more. The maximum value of $h(x, y)$ represents the point of greatest overlap. MATLAB has a function that normalizes cross-correlations so identical images will have a maximum value of 1.

Once again, the reconstructed images were compared to a truth image. The truth image was obtained in the same manner as in the previous section. Since the reconstructions occur where an undeviated image would appear, they were in the same position as the truth image, assuming the target and camera did not move relative to each other. When the reconstruction [$f_2(x, y)$] and the truth image were dissimilar, the maximum value of $h(x, y)$

was lower. When they were similar, it was closer to 1. This maximum value was used to represent the image quality and plotted against wavelength. Ideally, the plot would be the spectrum of the scene.

3.3 Spectral Resolution and FWHM

One of the goals was to produce accurate pseudo-spectra of a scene. Spectral resolution refers to how well the instrument or method can distinguish between two different wavelengths. When using atomic emission lines, the spectral resolution of the instrument should determine the width of the lines in a spectrum [1]. For other sources of light, spectral reconstruction quality can be determined by comparing the shapes and sizes, including the width of an emission line, of the reconstructed spectral data to independent measurements. One way to determine line width is by measuring its full width at half of its maximum value. The Full Width Half Max (FWHM) of a line is the spectral distance between two points of a curve at half of its maximum intensity, and is presented in terms of length (if the wavelengths are measured in nm, line width should be measured in nm). If a curve has an arbitrary relative peak intensity of 1, its width will be calculated by measuring the distance between points on either side of the peak with intensity 0.5.

Spectral resolution also describes the minimum spectral separation required to distinguish two peaks. Often times, as in a Mercury emission spectrum, the spectroscopic fine structure predicts 2 peaks very close together [3]. This is called a doublet. According to Rayleigh's Criterion, lines are just resolved if the saddle between to peaks is no more than $8/\pi^2$ of the peaks' values [11]. By looking at a doublet, the system's spectral resolution can be determined if the peaks are resolved. The spectral resolution is typically wavelength dependent and can be limited by the optics, pixel size, and/or image processing method.

3.3.1 Predicting Line Width.

The line width of a pinhole can be predicted independently of the spectrum building techniques. If a source of light were truly a point source with perfect optics, the light would

34

fall on a single pixel and the area to be used for the mean intensity would also be one pixel. Since there is no true point source, the light always fell on an area of pixels. When reconstructing, the total energy took a certain number pixel shifts (which can be related to a wavelength) to traverse the area for measurement. Therefore, the pixelated nature of FPAs give spectral lines minimum widths. The diameter of the spot size can be used to estimate the FWHM. If the wavelength of a spot is known, the dispersion relationship can be used to calculate the range of λs it would take to traverse the spot (which is the same as the region summed over in the mean intensity technique), shown in Figure 3.6. Each line was for
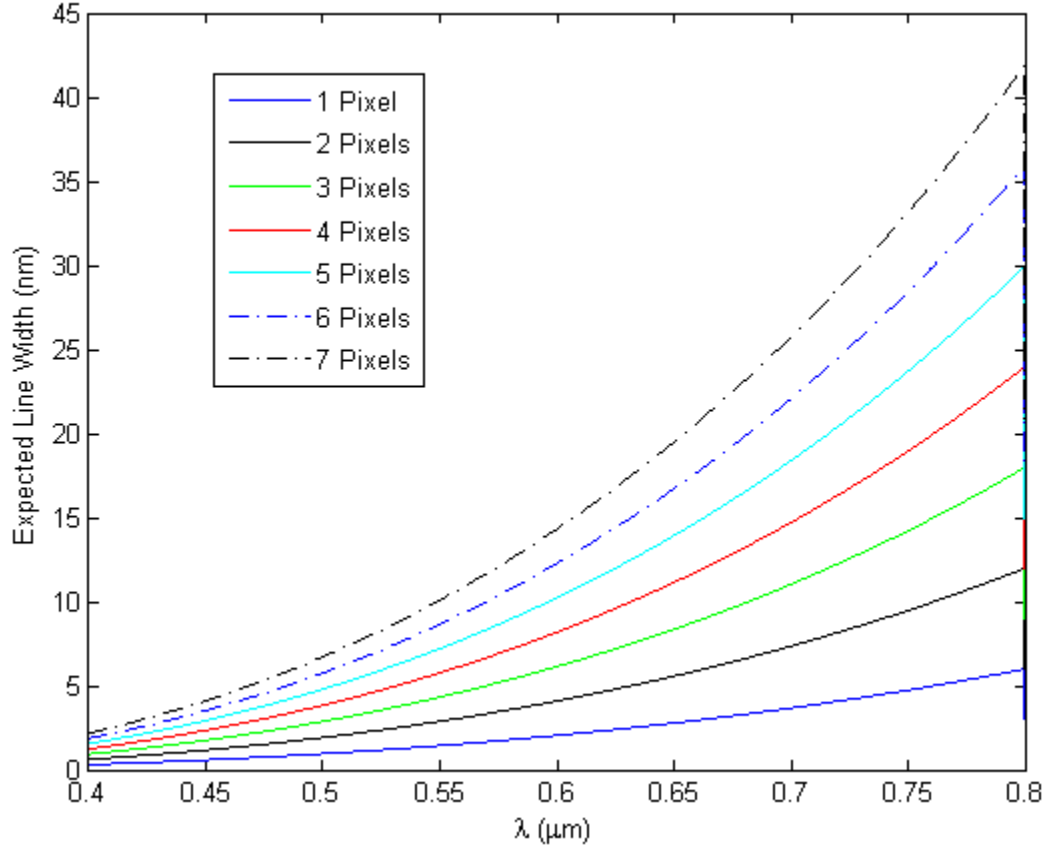
Figure 3.6: Plot of the expected line width based on wavelength and spot size. The legend indicates the diameter of a spot on the FPA.

a different spot diameter. If the spot diameter is divided by the focal length of L_3 by the

relation $y = f_3\theta$ (Equation (2.1)), the angle subtended by that bundle of light is calculated.

When θ is divided by the slope of the dispersion curve at the particular wavelength, the

bandwidth should be approximately the FWHM of the line.

3.4   Spatial Resolution

Just as spectral resolution tells the system's ability to distinguish between 2

wavelengths, the spatial resolution is how well it can resolve objects. The modulation

is useful in determining the system performance [11]. Modulation is defined by

$$v = \frac{I_{max} - I_{min}}{I_{max} + I_{min}}, \tag{3.3}$$

where v is modulation, I_{max} is the maximum intensity in the scene, and I_{min} is the minimum

intensity in the scene. The modulation was used to calculate the Modulation Transfer

Function (MTF), a common standard when assessing spatial resolution. MTF is defined as

the ratio of the modulation of the image to the object modulation. It is plotted on the vertical

axis with the horizontal commonly being spatial frequency. Spatial frequency units that

would universally work are cycles/radian. Because of the tendency for optics to degrade

images, MTF can never be greater than unity. An MTF of 1 means items are perfectly

resolved. It declines to 0 at the cutoff frequency where the system can no longer resolve

objects.

The MTF of CTEx was measured using the Air Force bar chart as the object. Since it

only used black and white areas, its object modulation was assumed to be 1. To calculate

v_{image}, intensities of the white areas and black areas were measured in pixel counts. The

MTF of CTEx is in Figure 3.7.   The curve should decrease all the way to the cutoff

frequency. The raw frames showed the cutoff frequency to be between 3,400 and 3,900

cycles/radian. The non-zero values at spatial frequencies greater than that were from
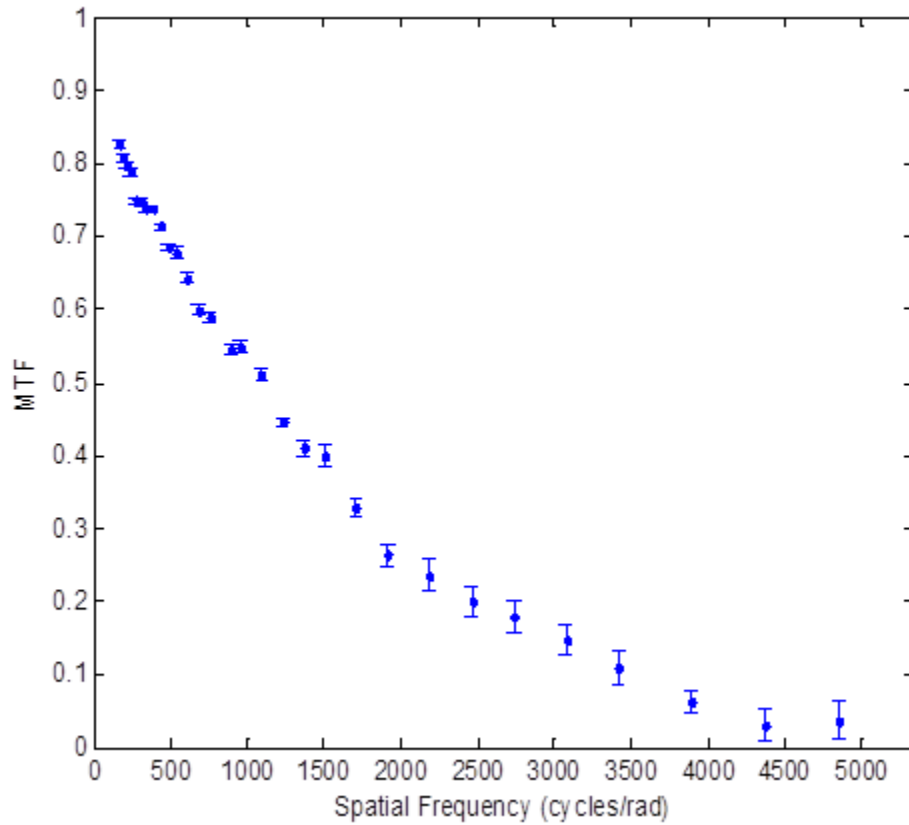
Figure 3.7: The MTF of CTEx. Examining the raw data showed the cutoff frequency to be between 3,400 and 3,900 cycles/radian. The non-zero values at higher spatial frequencies were a result of aliasing.

aliasing. Aliasing causes two signals to become indistinguishable. Hecht and other optics and imaging textbooks provide deeper discussions of MTF [11].

3.5 Collecting Data

The experimental setups throughout the project were as follows, unless otherwise stated. When simulating a point source, the light source (most often a pen lamp or white light source) was placed behind a 25 μm circular pinhole on an optical bench. The edges of the apparatus and the surface of the bench were cloaked with a black velvet cloth in order to

37

minimize stray light and reflections. The lamps and white light source were allowed several minutes to warm up and reach a steady emission state, per the manufacturer's instruction. The overhead lights were also turned off. The pinhole was located about 2 m from L_1. The angular breadth of the light source was then 12.5 μrad. The intensities of the pen lamps were fixed, but the white light source was adjustable. It was normally turned to an exposure time so the Phantom camera maximized its 8-bit dynamic range. The settings were normally a 49,900 μs exposure time at 20 Hz frame rate. The prism spun 0.6 Hz. When optical filters were used in CTEx, a small platform was built inside the hardware. The filters were placed on the platform directly behind L_2. They were flush with the lens so the light did not hit the filter at an angle. For some filters, that would have changed the transmissive properties.

Similar steps were taken when imaging the Air Force bar chart and the picture of an amorphous object. Instead of using a pinhole, the targets were taped to a cardboard box on the optical bench 2 m from L_1. The pen lamps and white light source were in between the target and CTEx, but out of the field of view. They illuminated the target with the overhead lights turned off. The focus was adjusted to look at a wavelength of interest and the camera was adjusted to maximize the dynamic range.

3.6   Independent Measurements

To validate much of the data collected, independent measurements of the spectra were often taken. AFIT had a small, portable Ocean Optics spectrometer. Its job was to measure only the spectrum to provide a baseline against which to compare the reconstructed data. The spectrometer was rarely collecting its data at the same time as CTEx. As long as the lamps or light sources were sufficiently warmed up, the emissions were assumed to be time-invariant. Therefore, the spectrometer data was taken either before or after the CTEx data. One good collection was often sufficient for each light source. It printed the spectrum by every 0.25 nm to a text file so it could be used and applied to other data sets.

When optical filters were used, they were placed in front of the collection unit of the spectrometer in order to collect the most accurate information possible. The transmissions of the filters were also measured independently. Even though the filters were labeled, they displayed characteristics that didn't seem to be consistent with what was expected. That warranted independent measurements. They were placed in a machine called a Carey spectroradiometer. It first measured the intensity of a beam with nothing in its path, then again with the filter in the path. The fraction of the filtered measurement to the unfiltered was the transmission. It printed the transmissions for each nanometer over the visible range to a text file so it could be used and applied to other data sets.

3.7   Determining Prism Angle Offset

Even though the encoder recorded the angle of the prism's rotation in a text file, its initial value reset every time it was powered on. That is, no matter the orientation of the prism, it would boot up saying it was oriented at 131°, even though the dispersion axis could have been anything. In order to correct for this, the user had to apply an angle offset correction in the reconstruction algorithm. To determine that angle, first a line was drawn on the casing of the prism with a permanent marker (not on the glass itself). Before turning on the encoder, that line was lined up with a reference on the motor. That would let the user know the angle offset that would give the true axis of dispersion to within 10°. After the video was taken, the reconstruction algorithm was executed at a single wavelength that was known to be in the scene (546 nm in the case of a Mercury emission). A reference object was often placed in the scene that had a known spatial structure, like the bar chart. An array of offset angles based off the initial position was entered to add to the angles ($\theta(\lambda)$ in Equation (2.5) and Equation (2.6)) in the text file the encoder wrote. The data was backprojected and each image was inspected. The one that built the reference structure the best determined the single offset angle to use. It was then entered as the offset, added to each data point in the text file, and the algorithm was changed back to reconstruct over

the entire band instead of a single wavelength. The value of the offset angle was accurate to within 1° since an error of 2° resulted in a noticeably worse reconstruction, seen in Figure 3.8. Experience helped in determining the optimal value as well.
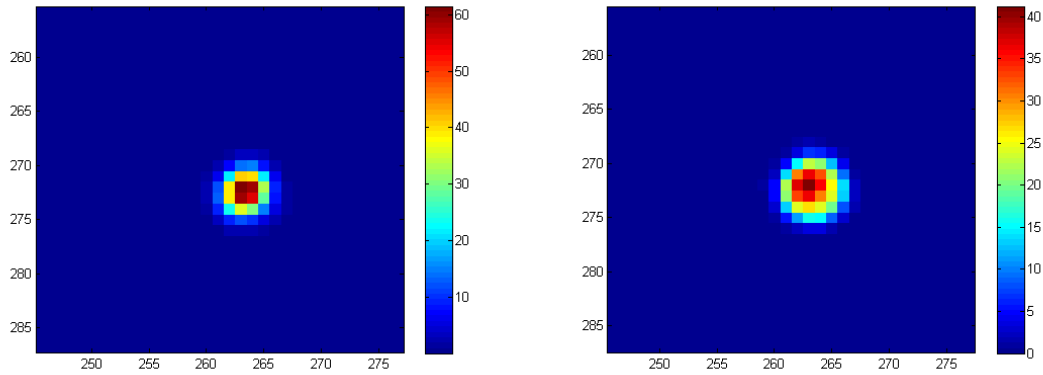
Figure 3.8: (L) The reconstructed image of the 641 nm emission from a Neon pen lamp within 1° of the proper offset angle. (R) The reconstructed image of the 641 nm emission from a Neon pen lamp within 2° of the proper offset angle . Selecting the proper angle to within 1° tightened up the spot and increased the maximum intensity in the scene.

IV.   Results and Analysis

This chapter will discuss the results of the experimental data.   It starts with explanations of common observations throughout the project. It then describes the results and compares to theory the CTEx reconstruction of various scenarios.   The scenarios are broken down by measuring image quality as a function of spatial complexity, as a function of spectral complexity, and finally as a function of temporal complexity. It ends by discussing the results of a transient event in a field experiment.

4.1   Common Themes

Throughout the project, several errors in the accuracies of reconstruction were consistent in almost every data set. The wavelengths associated with peak intensities were almost always shifted toward one end of the spectrum or the other. If a certain wavelength was out of focus, it resulted in a lower peak intensity and a wider spectral line width. The spectral response of the Phantom camera also contributed to a low relative intensity. Explanations of these phenomena follow.

4.1.1   Wavelength Error in Reconstruction.

In almost every case, regardless of the spectrum building technique, the reconstructed wavelength disagreed with either the theoretical or truth wavelength. Early in the research, it was assumed the difference was the result of an error in the calculated pixel shift per wavelength. Attempts were made to quantify the difference as a function of wavelength. The correction was to be incorporated into the algorithm so the videos would reconstruct at the proper wavelength. The results proved inconsistent, and it was discovered that the error was not the same in every case; it wasn't always even in the same direction. Instead, the difference between the reconstructed and predicted peaks was a function of the pixel nature of the FPA and the intensity pattern of the data. If frames that spanned slightly more than

41

1 complete revolution of the prism were used, the distribution of intensities in the halos were out of balance. The object was ensured to be at the center of the field of view. That was difficult to get perfectly, especially if the shape of the object was asymmetric. The imbalanced intensity pattern caused the peak to occur at some wavelength other than what it was supposed to be.

The position of light on the FPA was measured to see if the dispersion curve in Figure 2.3 agreed with the actual dispersion. The Neon pen lamp was reconstructed and the radii of the halos were measured in pixels. The pixel distance was converted to a real distance assuming a 20 μm pixel size. The true dispersion angle was calculated based on the distance with Equation (2.1) and compared with the modeled curves in Figure 2.3. The model was found to be accurate to within $0.001°$.

One possible explanation in the wavelength difference lies in the dispersion curve itself. The dispersion curve was merely a prediction and not based on data. When measured, the radii of the halos in pixels corresponded to the predicted dispersion for the particular wavelengths to within 0.5 nm, assuming a 20 μm pixel. The prediction was by calculating the nominal indices of refraction of the pieces of glass. Even though those indices are well known, small defects in the manufacturing of the glass may have adjusted them slightly. If the chemical makeup wasn't exactly what was reported, the indices of refraction might have differed from the curve in Figure 2.3 [14]. A refractive index error of as little as 0.01% in either piece of glass would result in a 2.1 nm wavelength shift. Since the same pattern was not seen in other scenarios, there is question as to how valid that might be.

Recall distortion results in an image taking on a barrel or pincushion shape, depending on the direction of the distortion. Because of distortion, objects furthest away from the optical axis are displaced more than objects near the axis. Those on the axis aren't moved at all. This could result in a reconstruction wavelength error for those off-axis objects. The

further from the axis (and further from the undispersed wavelength), the greater the error. To investigate whether or not distortion caused the wavelength error seen throughout the project, a Neon pen lamp scene was investigated. The lamp was imaged at the center of the field of view, on the extreme left, and on the extreme right. Graphs of the reconstructed spectra and wavelength error are in Figure 4.1 and Figure 4.2. The left graph shows the
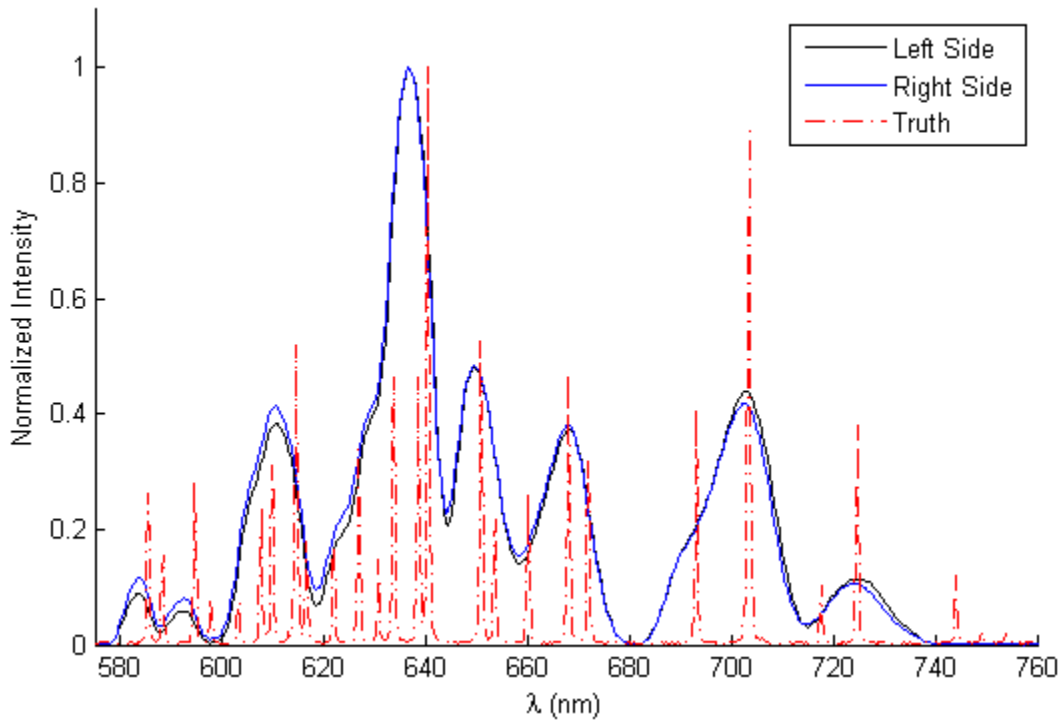
Figure 4.1: The reconstructed spectra for the lamp placed in the FOV's extreme left, right, and a truth spectrum.

reconstructed spectra of the left and right placements as well as the truth spectrum. The right graph is a plot of the error in reconstructed wavelength. If distortion was affecting the reconstructed wavelengths, all placements would follow an upward trend in the error plot. Light would have been distorted more as functions of distance from the dispersion axis
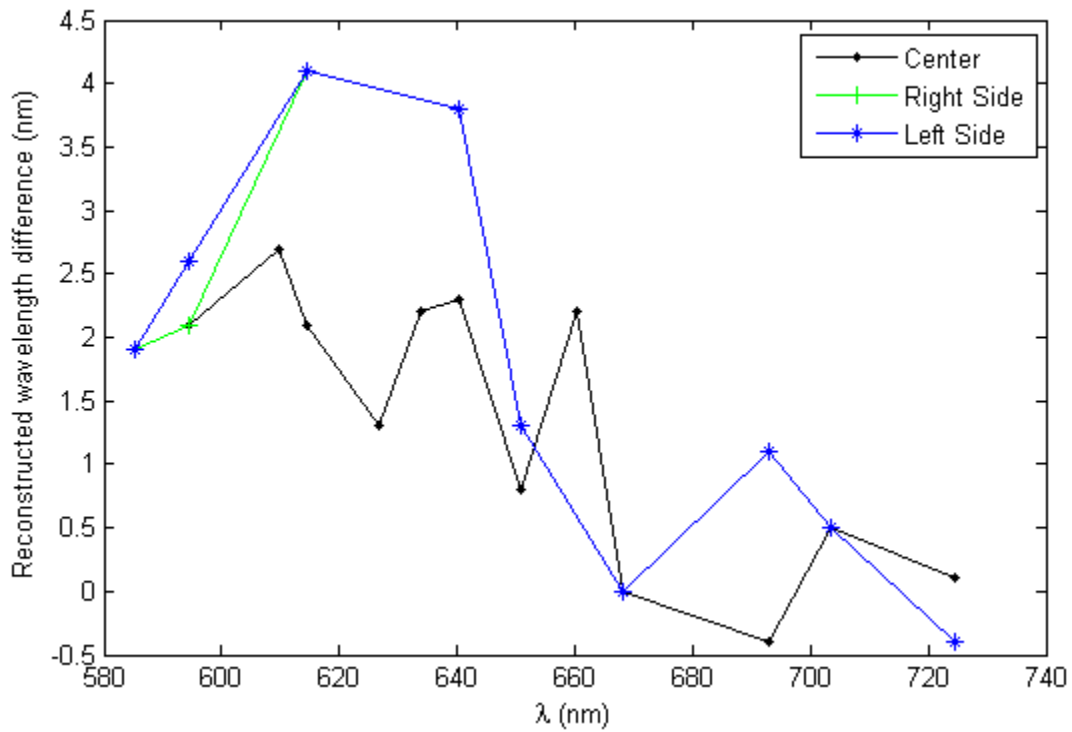
Figure 4.2: The error in reconstruction for each placement of the pen lamp. Since the error plot did not follow upward trends, distortion did not likely affect wavelength reconstruction.

and spectral separation from the undispersed wavelength. Since each line's reconstruction actually improved as the wavelength moved away from the undeviated, distortion was not likely causing the errors. An analysis of the pen lamp placed in the center of the FOV will be in the Spectral Complexity section.

4.1.2 Spectral Response.

Cameras do not detect every wavelength equally [22]. A simplistic example is a camera used in amateur photography detects the visible spectrum well, but isn't very useful for seeing anything outside that band. Even within a camera's detectable range, not all light is collected as efficiently as other light. The response at the edges of the band isn't usually as high as it is in the center. Even there, there are often fluctuations. Figure 4.3 shows the

manufacturer's nominal spectral response curve of the Phantom camera used in this project [25]. The spectral response is measured in A/W as a function of wavelength. It tells the
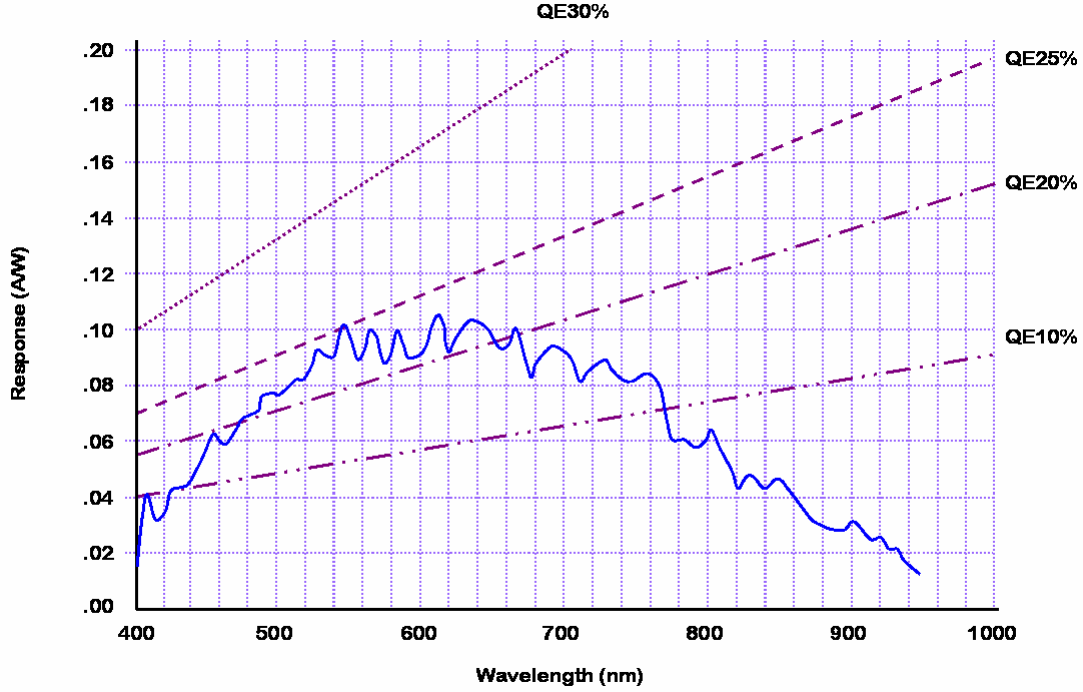
Figure 4.3: The manufacturer's nominal spectral response curve for the Phantom camera [25]. It is not constant in the visible range and even fluctuates greatly between wavelengths that are close together.

amount of current produced for each watt of a certain color of light incident on the camera's FPA. This isn't as intuitive of a measurement as quantum efficiency (QE) is. QE measures the number of photo-electrons produced at the FPA per incident photon as a function of wavelength, and is a percentage [22]. In fact, several QE lines are shown in Figure 4.3. The conversion from spectral response to quantum efficiency is

$$\eta = R\frac{hc}{q\lambda},\tag{4.1}$$

45

where η is quantum efficiency, R is spectral response, h is Planck's constant, c is the speed of light, q is the charge of an electron, and λ is the wavelength of the incident photon [22]. The shape of the QE curve will be different but similar to the one in Figure 4.3. What will be important later in the project are the fluctuations. Emissions could be seen, even in raw data, as having fluctuating intensity with respect to λ. The wavelengths at the extreme ends of the visible spectrum were not used as efficiently as those in the middle, leading to lower intensities. Broad-band light also fluctuated in intensity, even if the true emission of a source was constant.

4.2 Image Quality vs Spatial Complexity

This section investigates reconstructed image quality as a function of the spatial complexity in the scene. The first situation discussed is a pinhole that simulated a point source. Next is of an Air Force bar chart. It represented a very spatially simple 2-D scene with sharp edges. Finally, a textbook cover which shows a medical tomography reconstruction of a brain was reconstructed. It had soft edges and amorphous features. It was a scene which was expected to be the most difficult to reconstruct spatially.

4.2.1 Pinhole.

The simplest scene in terms of spatial complexity was of a point source of light. A 25 μm pinhole at a range of approximately 2 m and back-lit by a pen lamp was used to simulate a point source. Though not a true point, it only occupied a 3x3 pixel area or smaller on the FPA when in focus. During reconstruction, the point sources were manifested as concentric halos in off-wavelength images and as a point-like collection of square pixels in on-wavelength images, like in Figure 4.4. It is the 435 nm reconstruction of a Mercury pen lamp with 546 nm light in focus. The radii of the halos varied according to the slice along the λ axis of the hypercube. The halos in a particular slice of the hypercube were smaller for the colors closest to an on-wavelength reconstruction and larger for those further. The
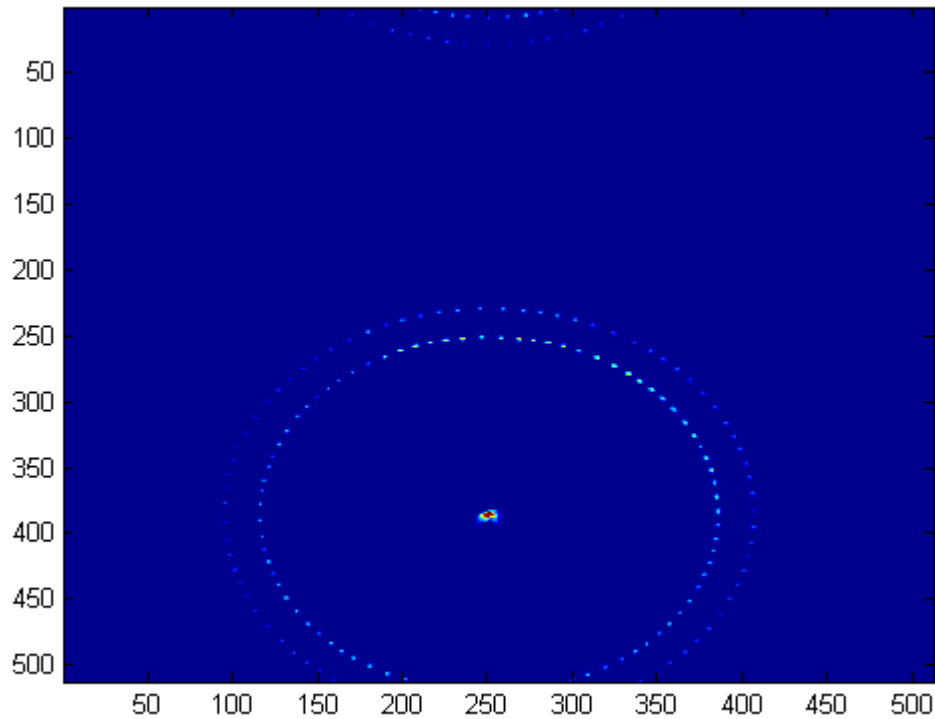
Figure 4.4: The 435 nm reconstruction of a Mercury pen lamp behind a pinhole. The inner-most spot is the 435 nm light. The middle halo is 546 nm and the outer-most halo is 578 nm. If the reconstruction were on any of these wavelengths, the corresponding light would form a point-like collection of pixels in the center of the halos. The radii of the halos can be traced to the spectral separation between the light and the reconstruction wavelength. The dots on the top of the figure are consequences of the periodicity of discrete Fourier transforms and are 578 nm data.

radii of the halos related to the spectral separation between the color of the light and the reconstruction wavelength.

The unfiltered backprojection algorithm was used to reconstruct the pinhole images. Since the pinhole simulated a point source, using edge and gradient techniques did not make

sense to build spectra. Cross-correlation and the MAE techniques weren't used because even the slightest discrepancy between the reconstructed and pristine images would have produced poor results. Therefore, only the mean intensity of the area around the center of the reconstruction was used to build spectra.

Figure 4.5 shows the unfiltered backprojection spectrum of a Mercury lamp behind the pinhole. The 546 nm line was in focus. The reconstruction produced a spectrum that was similar to the independent measurement with some very important differences. The most important difference was the error in wavelength. The peak intensity from the independent measurement was 545.8 nm and 543.6 nm in the reconstruction. The other differences are tabulated in Table 4.1. There was also no reconstruction information for the 405 nm line.

Table 4.1: Table of the differences in peak intensities for an unfiltered backprojection of a Mercury lamp behind a pinhole and an independent measurement

Reconstructed λ (nm)	Actual λ (nm)	FWHM (nm)
–	404.4	–
434.2	435.5	5.1
543.6	545.8	4.6
576.0	576.7/578.7	5.4

It was so badly out of focus or dispersed so that the energy from it was spread out over a larger area of pixels. Since energy must be conserved, the average intensity on each pixel was low enough to be subtracted out as noise. 405 nm was also in a region of low spectral response in Figure 4.3.

Another difference was in the widths of the lines. Though the independent spectrometer did not show the lines as delta functions, they were narrow compared to the
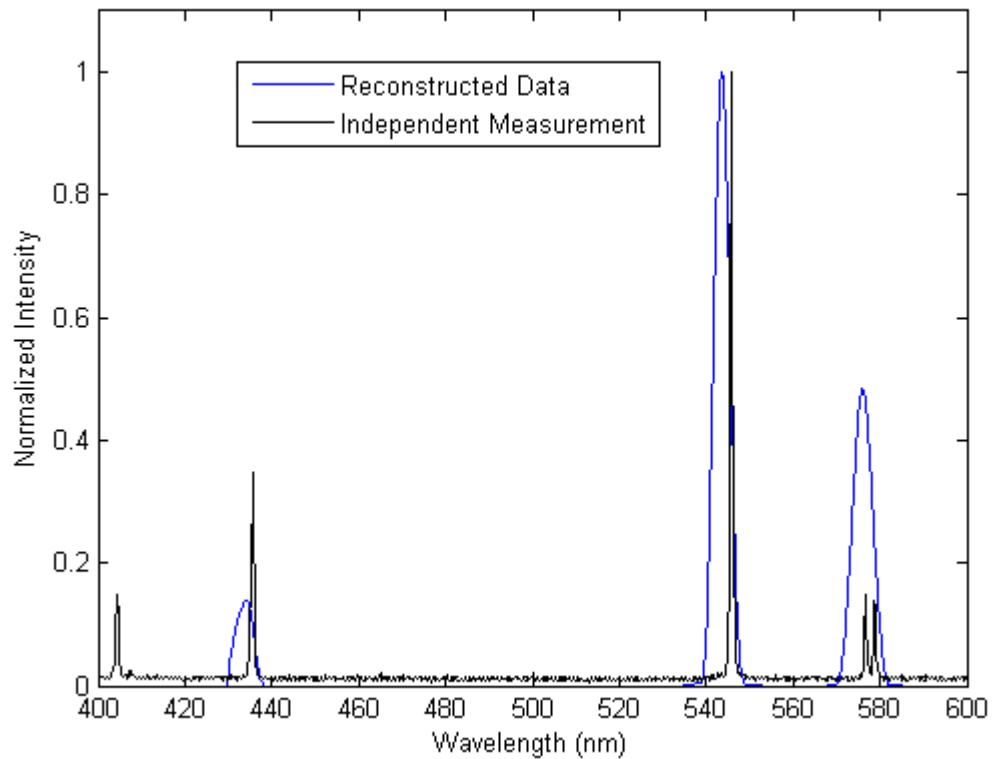
Figure 4.5: A comparison of the spectrum from an independent spectrometer measurement and using the Mean Intensity technique from an unfiltered backprojection. Though the spectra were similar, there were some major differences, including differences in the wavelength at which peak intensities occured. There was also some missing spectral information in the backprojection because 405 nm light was so far out of focus, it was subtracted out as noise. It was also in a region of low spectral response.

widths of the reconstruction. In addition to the optics degrading the lines that were in focus, the size of the pixels on the camera, dispersion of the prism, and the mean intensity technique combined to widen the lines. Recall the mean intensity technique measured the mean pixel count of all of the pixels over a given range in the image. If a 3x3 pixel area was selected, spectral information began to be measured when even the smallest bit of the

49

collapsing halo encroached on the area. It ceased measuring the spectrum when the last bit of the halo left the area, shown in Figure 3.3.

Each bit of energy was measured for a minimum of 3 pixels (3 to travel perfectly vertically or horizontally through the area) and a maximum of 4.24 pixels (the diagonal distance of the area). When reconstructing for shorter wavelengths, shifting the image by a single pixel (in the shift-and-add technique) corresponded to a smaller wavelength shift than it did for longer wavelengths (Figure 2.3). For instance, 1 pixel at 435 nm contained only a 0.45 nm range of light. 1 pixel at 700 nm had 3.37 nm. Therefore, the algorithm required fewer distinct wavelength reconstructions to move the blue light through the region of reconstruction than the red (Figure 3.6). If everything was in focus, the short wavelengths should then have the smallest line widths (Table 4.1 also lists line widths). The 435 nm had a larger width because of the chromatic aberration discussed earlier.

Finally, the relative intensities of the lines weren't consistent with the independent measurements. The relative intensities of each curve were normalized by the maximum intensity for each measurement. The reconstructed data were divided by their own maximum values, and likewise for the the independent data. Since the 546 nm peaks were the brightest in each, they were both assigned values of 1. 435 nm was lower than the spectrometer measurement because of its defocus. The energy over more pixels resulted in a lower mean intensity on each pixel. To test this, the areas underneath each curve were compared. The ratios of the widths of the 546 nm line to the 435 and 578 nm lines for each measurement were calculated and presented in Table 4.2. The ratios of the green widths

to the blue widths agreed to within 9% for the Ocean Optics and CTEx measurements. Since the spectrometer and Phantom camera each used a silicon CCD [21], it is possible they had similar spectral response curves. The 578 nm doublet's ratios weren't nearly as

50

Table 4.2: Comparison of areas underneath spectral curves for the independent spectrometer and the CTEx pseudo-spectrum. The ratios were calculated by dividing the area of the 546 nm curve by the other emissions' curves. They were similar for the 435 nm line but not for the 578 nm doublet.

λ (nm)	CTEx Area ratio	Ocean Optics Area ratio
435	4.7	4.3
546	1	1
578*	1.6	3.4

close. Either the spectral responses differed at that wavelength, or there is some other phenomenon occurring.

The 578 nm doublet was clearly not resolved by the reconstruction because there wasn't even a visible saddle. Since all of the energy from the 2 peaks was condensed into one curve, its mean intensity was larger than the independently measured spectrum. It was even more than the sum of the maxima for the two doublet peaks, however. Since this wavelength was the longest measured for Mercury in this project, the difference in shift distance from one wavelength to the next was the smallest. Energy stayed in the area for calculation longer, leading to a higher mean intensity and wider FWHM.

4.2.2   Air Force Bar Target.

The next level in complexity is using a scene that has a very simple spatial structure. As seen in Figure 3.1, the bar chart provides arrays of alternating white and black bars at at wide variety of spatial frequencies. The chart was 100 mm^2 and placed approximately 2 m from the objective lens. Video of the chart was recorded while it was illuminated by a Mercury pen lamp, a white light source, and the overhead fluorescent lights. Additionally,

combinations of optical filters were placed in front of the prism for the pen lamp and white light source recordings.

4.2.2.1 Unfiltered Backprojections.

When using the unfiltered backprojection on the bar target illuminated by a Mercury pen lamp, the reconstructed image was very clear for the brightest peak at 546 nm. Figure 4.6 shows the reconstructed image of this scene at 545.8 nm, which, to the eye, was the clearest reconstruction in the cube. The figures appeared upside-down because
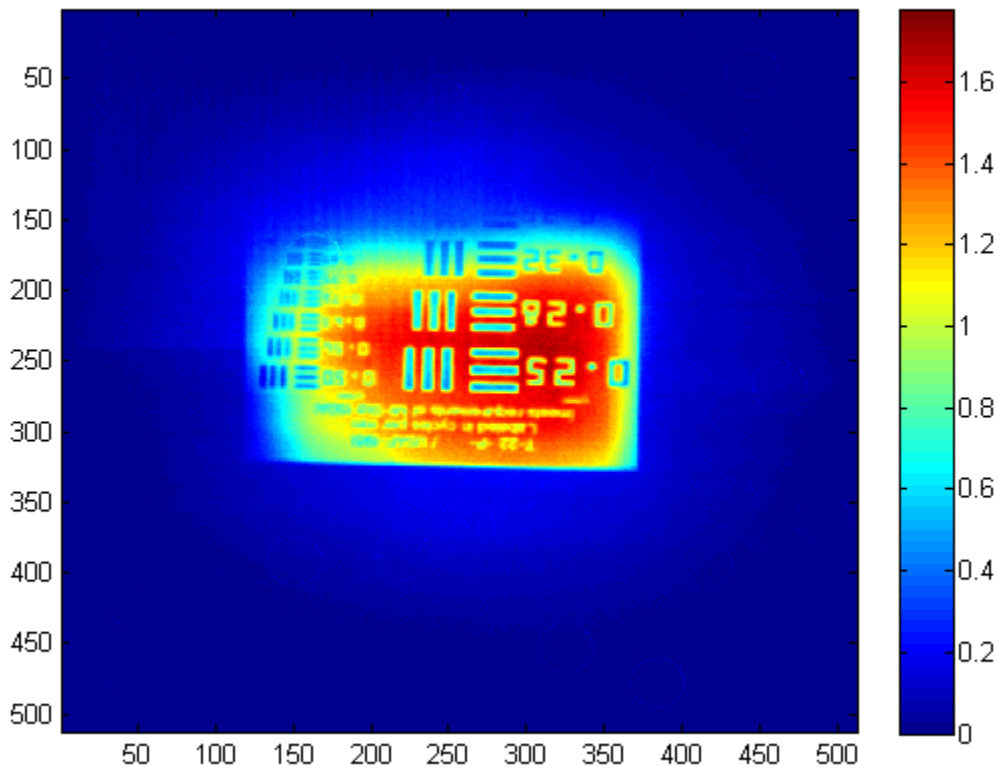
Figure 4.6: An unfiltered, backprojected reconstruction of the bar chart illuminated by a Mercury pen lamp at 545.8 nm. The figure is upside-down because the optics flipped the image.

of the inverting of the image by the optics. The color scheme is an intensity scale from MATLAB, with red being the most intense and blue the least. The numbers on the x and y axes represent the pixel positions on the FPA. The periodic vertical bars above pixel 250 are from fixed-pattern noise in the camera. Though the energy from the 435 and 578 nm emission lines was present, the quality of the reconstruction caused the signal from the brightest line to drown the rest out in the spaces that were white on the actual chart. The bars with the smallest spatial frequency (or largest size) near the center of the FOV have very sharp contrast and hard transitions between the dark bars and the bright background. The bars with the larger spatial frequencies (or smaller sizes) near the fringes of the targets have much softer transitions and fuzzy edges. This was the result of some amount of vignetting near the edge of the field stop. Additionally, the spatial resolution of the optical system limited the size at which objects can be resolved. The concentric intensity bands were also because of vignetting and can be seen in the raw images too.

Figure 4.7 shows the reconstructed image of the same scene at 435.8 nm.

Figure 4.5 and Table 4.1 clearly show there is an emission at this wavelength, though the reconstruction does not produce the bar chart. This wavelength was not in focus during the recording, so a pristine reconstruction was not expected. This line was also dimmer than the 546 nm line. In this case, the artifacts were bright enough to wash out the image. The structures near the (x, y) pixel (200, 260) indicate there may be energy from the 435 nm line surviving, though they can also be artifacts. The swirls and lines further out from the center of the FOV are also artifacts, and are likely the dark bars from the 546 nm emission.

4.2.2.2   Backprojected then Filtered Images.

Figure 4.8 shows the backprojected then filtered image of the same video used to reconstruct Figure 4.6 at 546 nm with different μ values. Again, the reconstruction displays the major spatial features of the original bar chart, including the text across the top of the chart. The filter successfully eliminated the wavelengths from other light outside of the
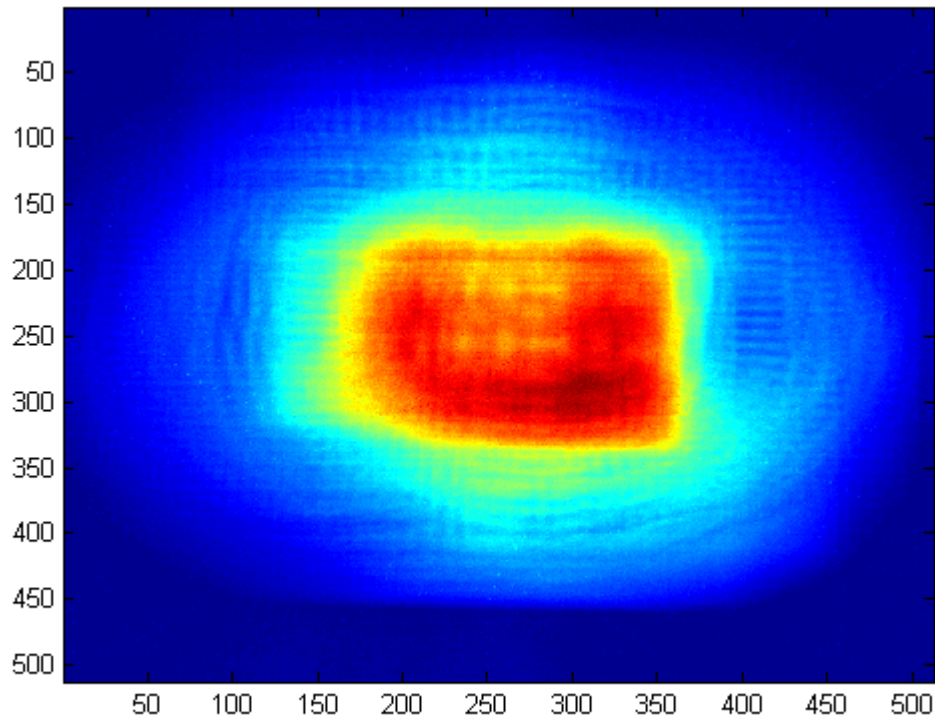
Figure 4.7: An unfiltered, backprojected reconstruction of the bar chart illuminated by a Mercury pen lamp at 435.8 nm. Even though there should be a good reconstruction at this wavelength, the artifacts from the brighter 546 nm wash out the image.

immediate spectral range of the reconstruction. The intensities inside the black spaces are 0, which was expected for a black area. The nonzero intensities in the black spaces in Figure 4.6 were artifacts from other wavelengths. When $\mu = 0.1$, the image became blurry. This indicates that using too low of a filter constant distorts the image. The succeeding images weren't blurry, but they did become more grainy with increasing μ. The overall intensities of the scenes also decreased as μ increased.

Backprojecting then filtering an image for a bright line that was in focus worked much better than it did for a dimmer, out of focus line. Figure 4.9 shows the backprojected then

54
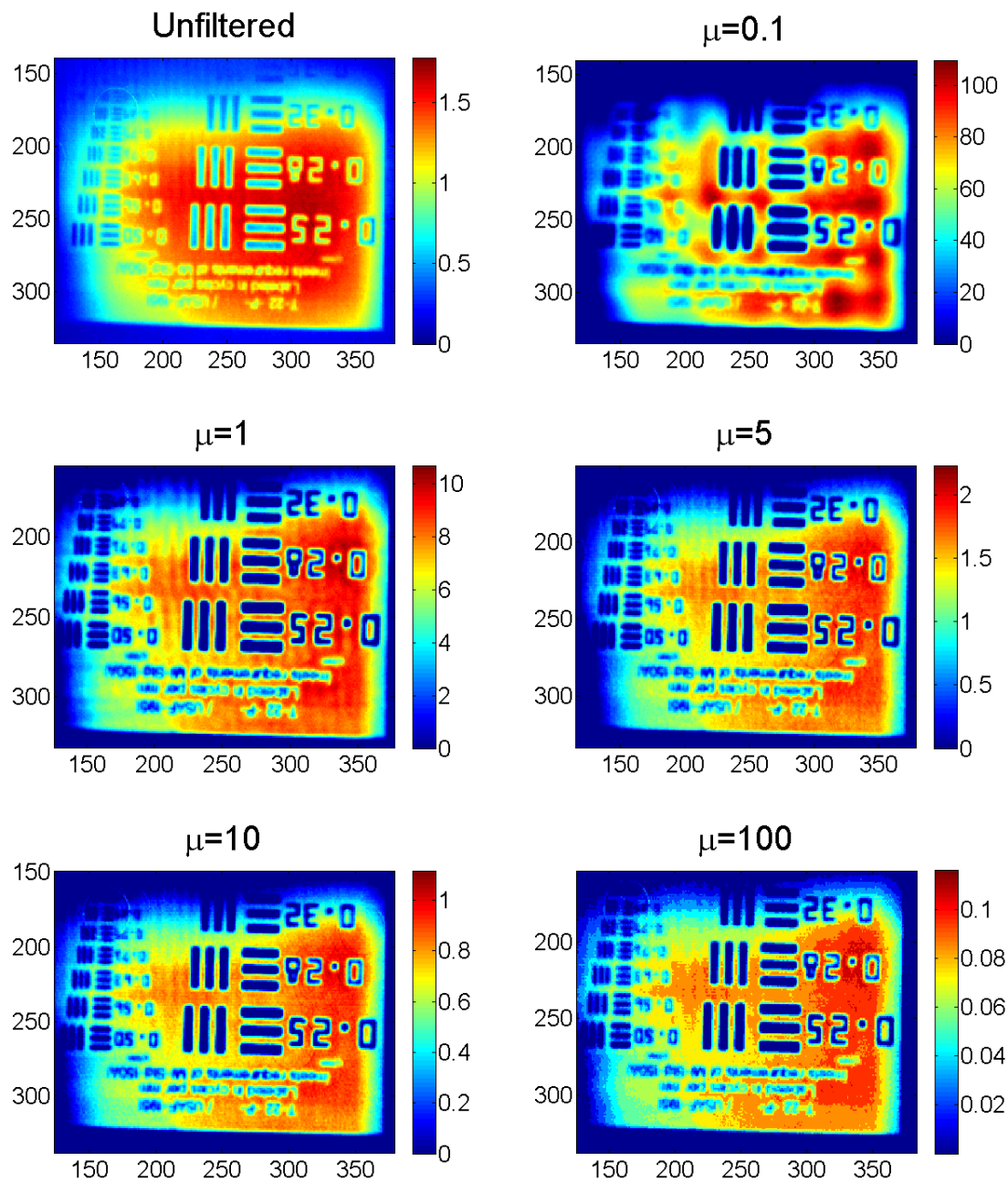
Figure 4.8: A comparison of backprojected then filtered images with a Mercury pen lamp with different μ values.

filtered image of the 435 emission when it was out of focus. This is the same slice of
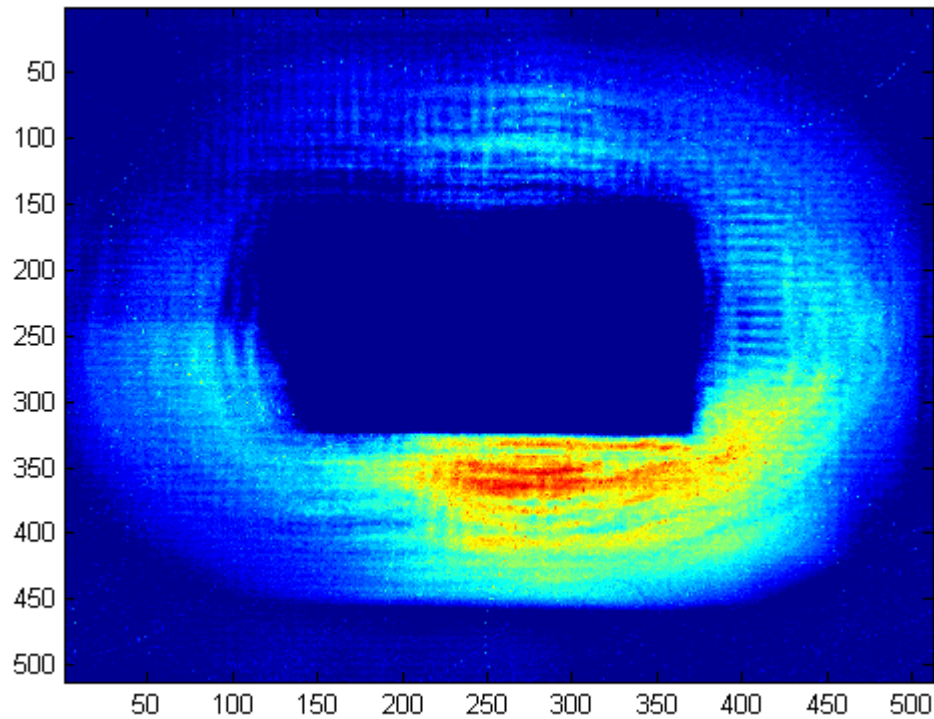
Figure 4.9: A backprojected then filtered reconstruction of the bar chart illuminated by a Mercury pen lamp at 435.8 nm.

the real hypercube as Figure 4.7, only filtered. The swirls were again around the rim of the higher intensity region. Those artifacts appear as regions of higher spatial frequency. The higher intensity (red and yellow) region in Figure 4.7 was more uniform and can be considered lower spatial frequency. It is not clear why the brightest central areas were completely deleted in the filtered image while the lower intensities around the outside survived.

4.2.2.3 Spectrum and Additional Peaks Due to the Bar Target.

Figure 4.10 shows the spectrum of an unfiltered backprojected of the bar chart illuminated by a Mercury lamp. Because of the chromatic aberration, the scene was imaged

once with 546 nm in focus and another time with 435 nm in focus.   The spectra were
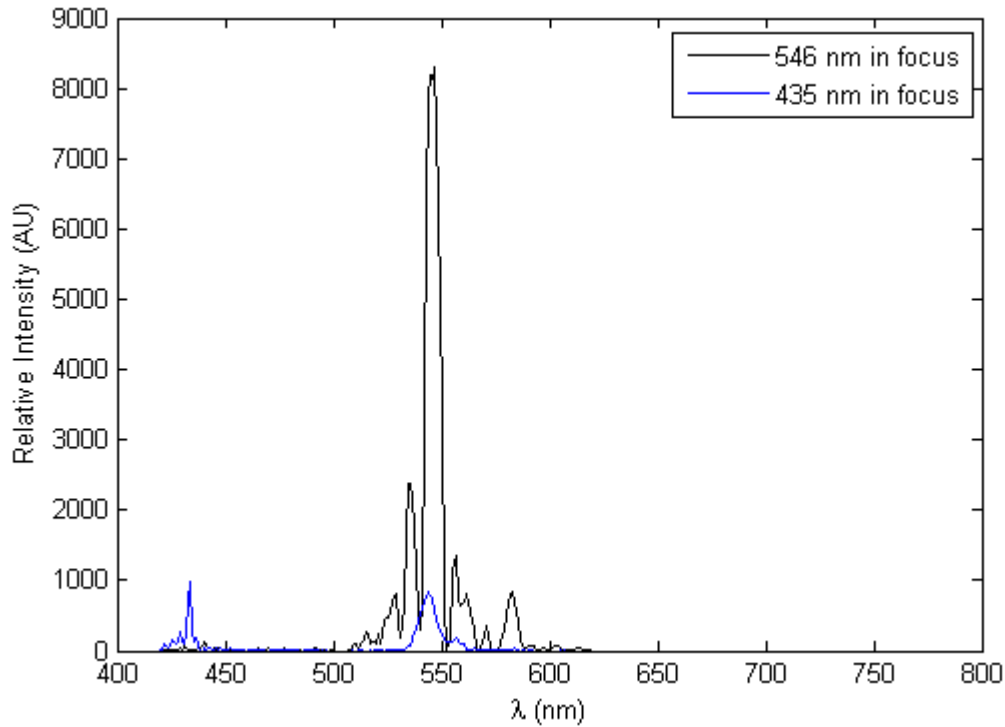
Figure 4.10: Spectrum of a Mercury lamp shining on a bar chart built with the gradient technique. It compares the spectra of 2 different CTEx data sets rather than comparing a CTEx measurement to an independent measurement. The black line is the spectrum with 546 nm in focus and the blue is when 435 nm was in focus. The smaller peaks near 546 nm were from artifacts of the bars that survived reconstruction.

built with the gradient technique. The 546 nm case produced a large intensity peak at the expected wavelength, and probably another peak at the doublet. Because of the lack of structure quality seen in Figure 4.7, the reconstruction showed no spectral information for 435 nm. Defocus clearly degraded the intensity of an object in a scene. When 435 nm was in focus, it had the highest peak intensity, though it was only slightly brighter than the 546

nm light. There was no noticeable reconstruction for the doublet. Since the independent spectrum measurement in Figure 4.5 showed the green (546 nm) line to have been much brighter than the blue line, it makes sense for it to be almost as bright when out of focus. If a lens with an achromatic doublet (focuses on 2 distinct wavelengths at a time) was in the system to focus on both of those wavelengths, it is expected the reconstructed spectrum would more closely match that in Figure 4.5.

An interesting consequence of using the bar chart must be discussed. Refer to the 546 nm focus spectrum in Figure 4.10. As expected, there were local peak intensities at 435 (very small), 546, and 578 nm (also small). There were significant lobes flanking the peaks as well. These were because of the artifacts of the bar chart during reconstruction. As the reconstructed wavelength approached a Mercury line, the ring of bar chart images closed down on the central point. A shift distance occurred where the right-most vertical bar of one image perfectly overlapped the left-most vertical of another image 180° away. The images formed a single bar with 2 dimmer bars each to the right and left (see Figure 4.11). Since a section of the bars fell in the area designated to build the spectrum, the algorithm measured the gradients of those features, with a peak falling at the point where 2 bars overlapped the most. When the reconstruction got even closer to the on-wavelength value, 4 bars lay perfectly atop one another to form another local peak. It was brighter than the last because the 4 bars that created two had a higher gradient than 2 bars creating one. The tallest peak, of course, occurred when every image in the video combined to form one at the proper wavelength. The process repeated itself in reverse as the reconstructed wavelength moved past the Mercury line, explaining the lobes at wavelengths longer than 546 nm.

4.2.3 Amorphous Object.

The final step in evaluating the quality of CTEx's images versus spatial complexity was to image a scene of something with less contrast and fewer sharp edges than the bar chart, or even amorphous. The copy of Hsieh's *Computed Tomography* textbook had a CT
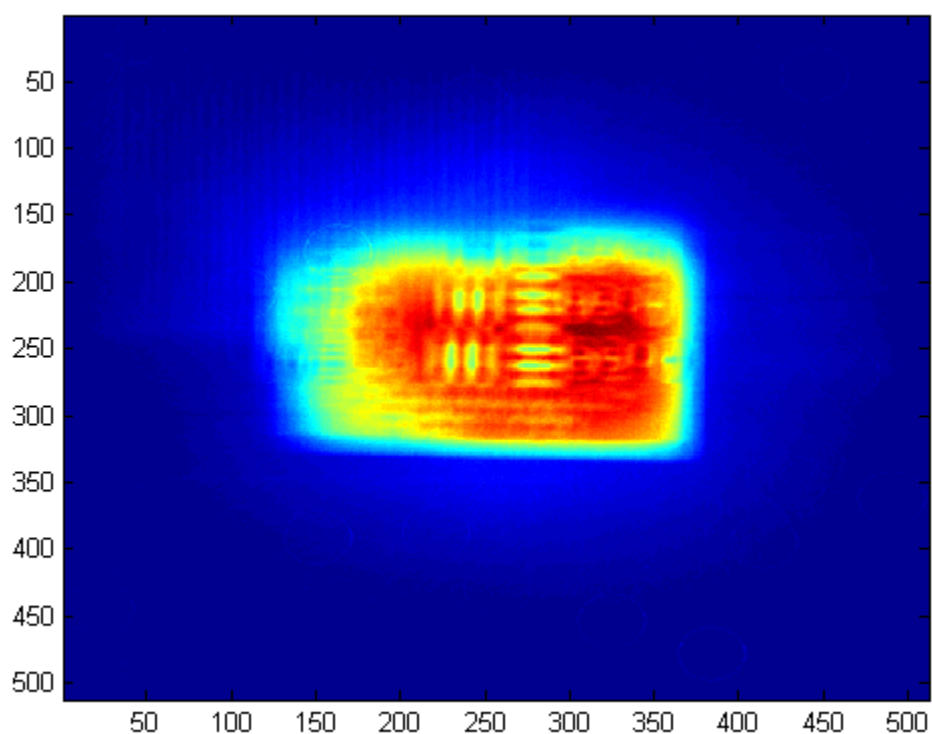
Figure 4.11: An off-wavelength reconstruction of the Mercury-illuminated bar chart at 535 nm showing the 4 bars. They led to smaller intensity peaks adjacent to the on-wavelength peak.

image of what appears to be a brain on it. The object had a combination of defined spatial structure and areas without much definition. A photograph of the area of the textbook used is in Figure 4.12. The square around the brain structure, as well as the white band around the border of the brain provided spatial structure. The areas inside the band were less defined and provided the greatest challenge in assessing the image quality in the laboratory. As with the other scenarios, the book was placed 2 m on the optical bench in front of the L_1. It was illuminated by a Mercury pen lamp, a white light source, and the overhead fluorescent lights with combinations of spectral filters. The picture was also

59
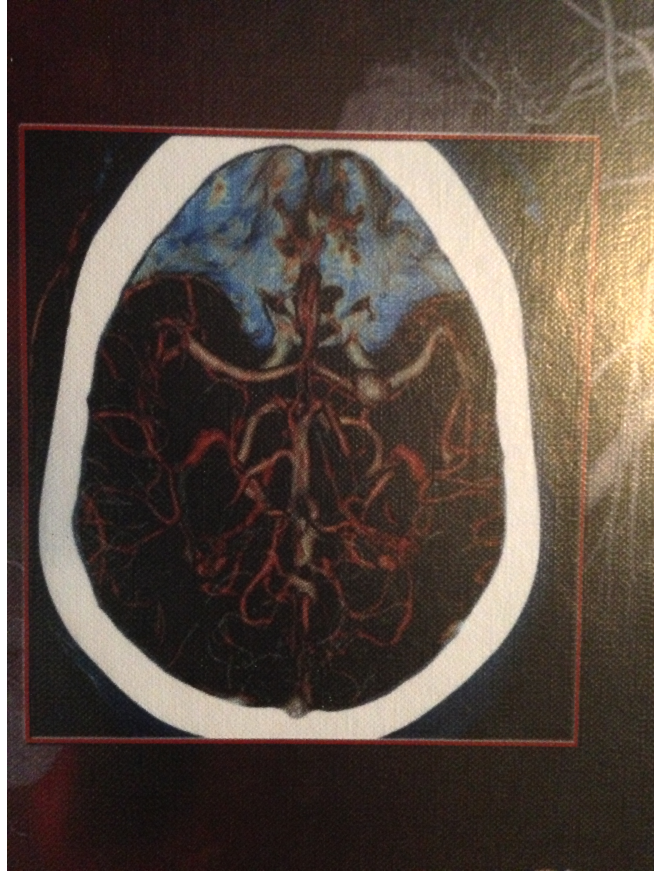
Figure 4.12: A photograph of the area of Hsieh's *Computed Tomography* textbook imaged as the most spatially complex laboratory scene. The square and border of the brain provided some contrast and sharp edges, while the objects inside the white border were less defined.

chosen because it provided enough white space, dark or black space, and areas of color. The colors provided unexpected challenges. For instance, when illuminated with the Mercury pen lamp and filtered so only the 546 nm light survived, only the white band was clearly defined. Some of the solid structure near the top of the brain also survived. The other stringy structures in the image did not reflect the green light very well.

As with the bar chart scenario, the algorithms reconstructed images that looked like the truth image, but did not provide accurate spectra. The pixels had higher overall intensities in the unfiltered images compared to their counterparts in the filtered images in an on-

wavelength reconstruction. The backprojected then filtered reconstructed image at 546 nm is in Figure 4.13. The unfiltered image showed more artifacts in the colored area, but
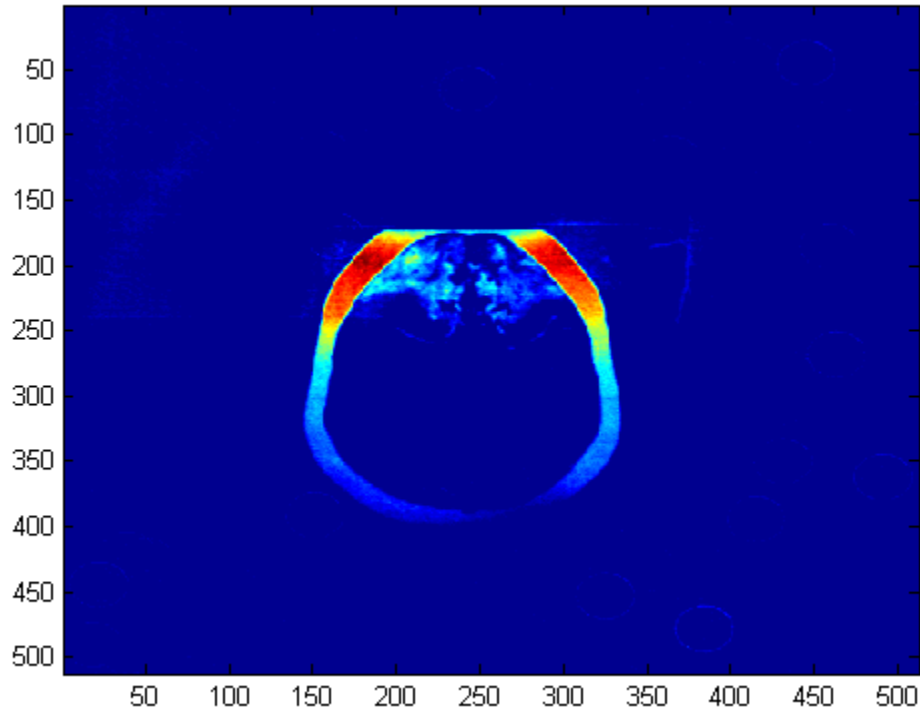
Figure 4.13: A backprojected then filtered image of the textbook illuminated by a Mercury pen lamp for the emission line at 546 nm. The unfiltered image looked almost identical, though some of the structure inside the brain near the top of the area was brighter.

overall was very similar.

As the reconstructions were displayed wavelength by wavelength, the filtered and unfiltered images had different patterns in the emissions other than 546 nm. Large areas where artifacts existed in the unfiltered images were blank in those that had been filtered, as seen in Figure 4.14. It is the unfiltered and filtered reconstruction of the picture illuminated by Mercury at 435 nm but with 546 nm in focus. The filter constant μ for this
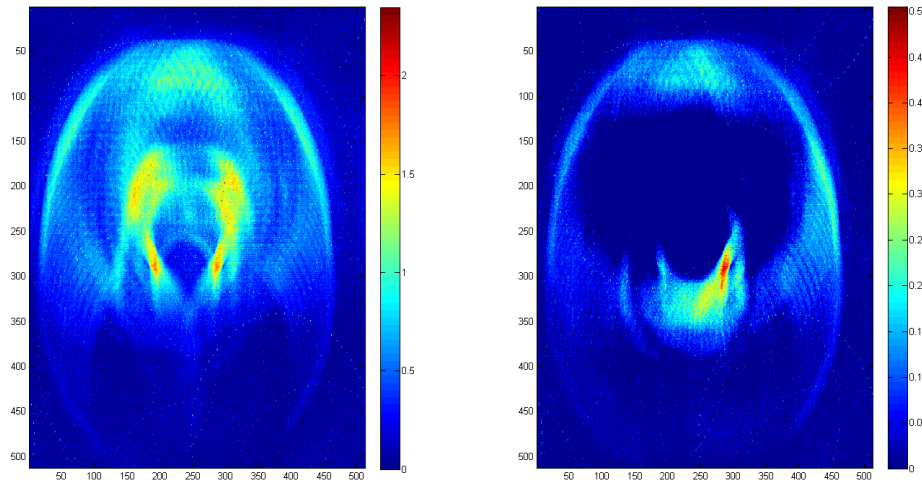
Figure 4.14: (L) Unfiltered reconstruction of the textbook cover at 435 nm out of focus. (R) Filtered reconstruction of the textbook at 435 nm out of focus. The filter constant μ was 5. The filter deleted a lot of the energy in the scene, including where intensities were the highest.

reconstruction was 5. This slice was picked for 2 reasons: to show the area of blank space caused by the filter, and to demonstrate there is absolutely no discernible reconstruction at a wavelength where there should have been one. Aside from an overall lowering of the intensities from the unfiltered to the filtered, much of the energy was deleted. The general outline of the blank space in the filtered image can be seen in the unfiltered. There did not appear to be a pattern associated with the deleted information. It included both higher and lower intensity pixels, as well as higher and lower spatial frequencies. The outline of the space might be identified as a region of relatively low spatial frequency, as in Figure 4.9. In that case, everything inside the borders was also deleted: high and low intensities and spatial frequencies.

The filtered image also contained spurious information that was not in the unfiltered image. Near the (x, y) pixel location (250, 320), the pixels were brighter compared to the

surrounding areas in the filtered compared to the unfiltered, and the intensity pattern took on a different shape. Both the blank spaces in the filtered images and the inconsistent intensity patterns in the artifacts were present over a wide range of wavelengths in the hypercubes. The blank space evolved to take on the shape of the white band as the reconstruction neared 546 nm until it appeared as it did in Figure 4.13.

The other reason for showing Figure 4.14 at 435 nm was to show the poor spatial reconstruction of the Mercury emission line. Even though this imagery was focused at 546 nm, the 435 nm light was clearly visible in the raw images, though a little fuzzy. Even if the structures inside the white oval were too dim, out of focus, and/or not reflective enough at this wavelength to image, it was expected the white oval itself would still be visible. There was no shape in either the filtered or unfiltered image to suggest anything was reconstructed. When video was taken of the brain with 435 nm in focus, pieces of the figure were successfully reconstructed, seen in Figure 4.15. The filter parameter μ was
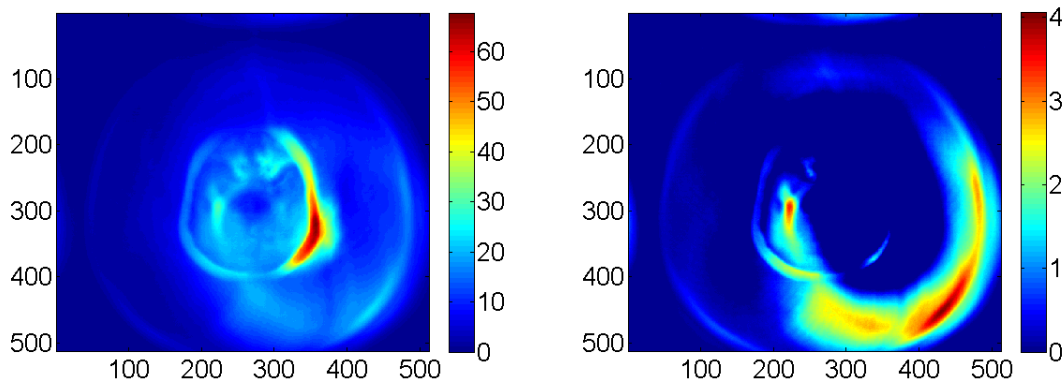
Figure 4.15: (L) Unfiltered reconstruction of the textbook cover at 435 nm focus. (R) Filtered reconstruction of the textbook at 435 nm in focus. The filter parameter μ was 5. The filter deleted a lot of the energy in the scene, including where unfiltered intensities were the highest.

63

5. The reconstruction was not nearly as good as it was in Figure 4.13 because the artifacts were almost as bright as the signal. In the backprojected then filtered image, much more of the brain image was lost. Most of the structure of the image was a ring of the same size as the outer-most portion of the light in Figure 4.14 with everything but the oval inside of it filtered. Based on this and the filter's behavior for the bar chart, it deleted intensities that didn't meet a certain threshold, even if the energy was from on-wavelength light. For both the filtered and unfiltered images, 546 nm was reconstructed with very few artifacts. Again, the unfiltered version had higher intensity throughout. More of the structure inside the oval was also present. If μ in Equation (2.17) was increased from 5 to 50, the patterns in the filtered image looked exactly the same. There was an overall reduction in image intensity and the picture was a little more grainy in the higher μ reconstruction.

The spectra in Figure 4.16 are for the case focused on 546 nm. The left figure is the

unfiltered spectrum and the right is the filtered. The region of reconstruction was everything inside the square in Figure 4.12. Considering what was seen in the hypercube for this case, the edge and gradient techniques were clearly the best tools for recreating a spectrum. In both cases, they produced peaks only from the 546 nm emission. The unfiltered peaks had larger line widths than the unfiltered because the artifacts produced false edges and gradients. They all reconstructed at 547 nm. In these plots, the 578 nm energy is lost. When the thresholds for the edges and gradients were lowered, that wavelength was very pronounced. Many other peaks that looked like the MAE information near 475 nm in these graphs also appeared, so the thresholds were kept low. At the higher threshold used in Figure 4.16, 578 nm did not reconstruct.

The mean intensity technique produced a peak near the correct wavelength, but in each case, the line width was very large. For any scene in which the target area is large, artifacts almost certainly fell in the region for measurement. The filtered line was more sharp and narrow at the peak than the unfiltered because of there were fewer artifacts. The mean
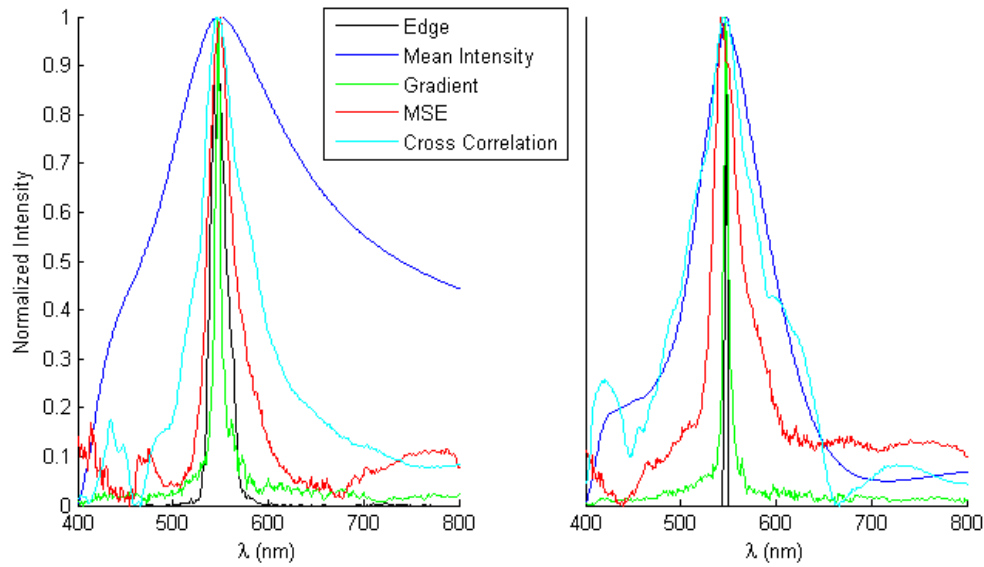
Figure 4.16: The spectrum of the brain illuminated by the Mercury pen lamp focused on 546 nm. The left spectrum is from the unfiltered backprojection and the right is from the backprojected then filtered reconstruction. The edge and gradient techniques were clearly the best for this case.

intensity line would not be a very good metric for determining the spectrum here because it suggested a very wide band of light with a peak at 546 nm.

The MAE performed similarly to the gradient and edge techniques, though the line shape was a little wider and the peak was shifted toward the blue. The wider line shape was because the images were similar for a wider range of wavelengths. Even well before and well after 546 nm, many features were very similar. The bumps in the unfiltered image near 475 nm and others were because the artifacts lined up so they did not contribute as much to the difference in images (Figure 4.17).

Finally, Figure 4.18 shows the spectrum of a white area of the image and a blue area using the mean intensity technique, still illuminated by the Mercury pen lamp. The regions

65
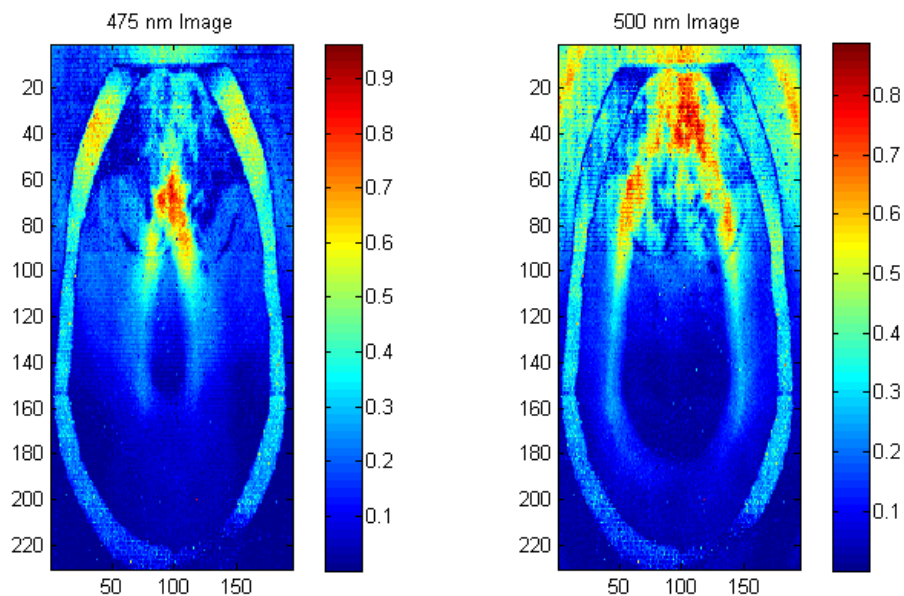
Figure 4.17: The images from the MAE calculation. The left figure shows the result of subtracting the reconstructed image from the pristine image near 475 nm. The artifacts lined up so they did not contribute as much to the difference in images. The figure on the right is near 500 nm, where the artifacts played a bigger role. The blue spaces contributed to a lower MAE.

chosen were both in the upper left part of the image. The white was a 3x3 pixel area of the skull. The blue was a 3x3 area of the brain. The white region reconstructed to a higher intensity because it reflected more wavelengths than the blue. Both had peak reconstructions near 546 nm, but also had smaller ones at the 435 nm line. The white area may have even reconstructed the 578 nm light as well. The blue pseudo-spectrum had peaks flanking the main lobe because of the bright artifacts of the skull portion in off-wavelength reconstructions.
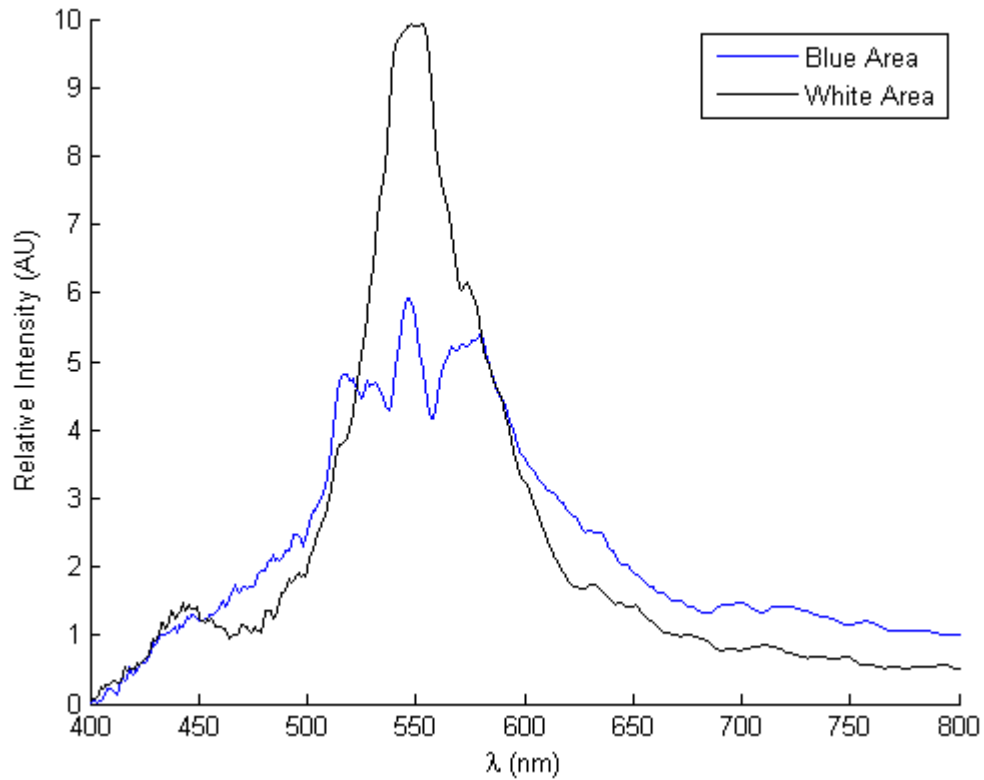
Figure 4.18: The pseudo-spectra of a white and of a blue area using the mean intensity technique, illuminated by the Mercury pen lamp.

4.2.4   Apparent Effects of the Filter and Cone of Missing Information.

Though a backprojected then filtered reconstruction often showed the scene with the dark spaces dark and the light spaces light, as in Figure 4.8, it did not every time. When the bar chart was illuminated by a Neon pen lamp, which had many more spectral lines than Mercury, some reconstructed images still showed the basic structure of the chart. It was missing intensities, however, in the white spaces, as seen in Figure 4.19. The filtered reconstruction shown was for the 703 nm line in Neon. Even though Table 3.1 shows that line to be the 5th brightest emission, an independent spectrometer measurement of the pen lamp's spectrum showed it to be the 2nd brightest, behind 640 nm. Most of the intensities

67
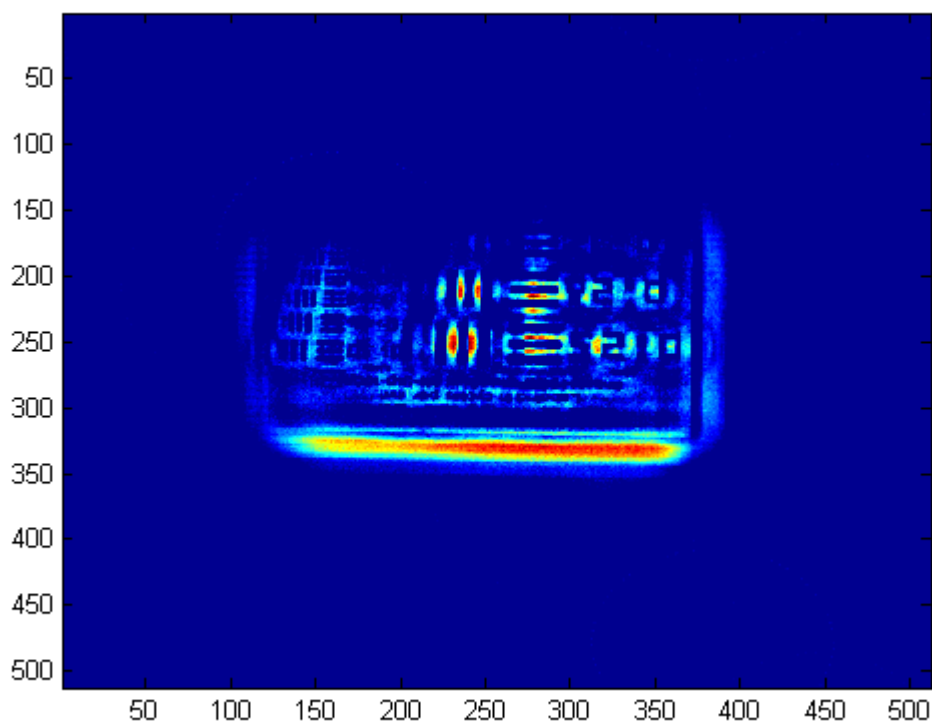
Figure 4.19: A backprojected then filtered image of the bar chart illuminated by a Neon pen lamp for the emission line at 703 nm. While some of the basic structure of the chart can still be seen, many of the white space intensities were filtered out.

in the white spaces did not survive backprojection and filtering, but the energies near edges did. This wasn't the case for every emission line. For the 640 nm reconstruction, the image looked nearly identical to Figure 4.8.

This effect was thought to be from the cone of missing information. A simple model to help understand the cone better was developed in MATLAB. First, a simulated hypercube in real space of the bar chart was created. It first consisted of 200 spectral planes, from 550-749 nm, each having 0 values in every pixel. An image of the bar chart was found on the internet. Its dimensions were 400x400 pixels instead of the 512x512 pixel recorded images.

The image of the bar chart was inserted in the planes corresponding to the wavelengths of a Neon spectrum. The intensity of each plane was scaled to the relative intensities of the independent measurement.

The cube was 2D Fourier transformed across both spatial dimensions, then 1D transformed across the spectral with MATLAB's *fft2* and *fft* commands, respectively. The boundaries of the cone was established inside the Fourier cube. The radii of the bases were 200 pixel units in Fourier space at the highest spectral frequency magnitudes. The waist of the cone connected at 0 spectral frequency. All of the data inside the cone was deleted to establish the cone of missing information. Finally, the Fourier cube was inverse transformed back into real space, first by 1 dimension across ζ, then by 2 dimensions across ξ_1 and ξ_2. The result was a (simulated) real data cube as if it had been backprojected and reconstructed. This model also simulated ideal sampling of the data outside the cone. It corresponded to infinite projections, no noise, and uniform illumination of the target.

Figure 4.20 shows the 703 nm slice of the simulated cube with the cone missing. Like in Figure 4.19, the areas of white space have been eliminated from the figure.

The edges have also been outlined even sharper. Recall that in Fourier space, high spatial frequencies give the real image sharp edges. Low spatial frequencies give energies and information in between sharp edges in a signal or image. Since the higher spatial frequencies survived outside the deleted cone, the edges were well defined. All of the white space from Figure 3.1 showed up as empty after the cone was removed. In Fourier space, the white area was represented by the lower spatial frequencies, many of which were deleted. Additionally, off-wavelength slices of the real cube did not remain blank after the cone was deleted. They resembled what was seen in Figure 4.11, though still blank between the bars' artifacts, as in Figure 4.20. These effects were only seen in the backprojected and filtered images; the unfiltered images retained information in the white spaces. It is not clear why the filtered images seemed to be affected more than the unfiltered.
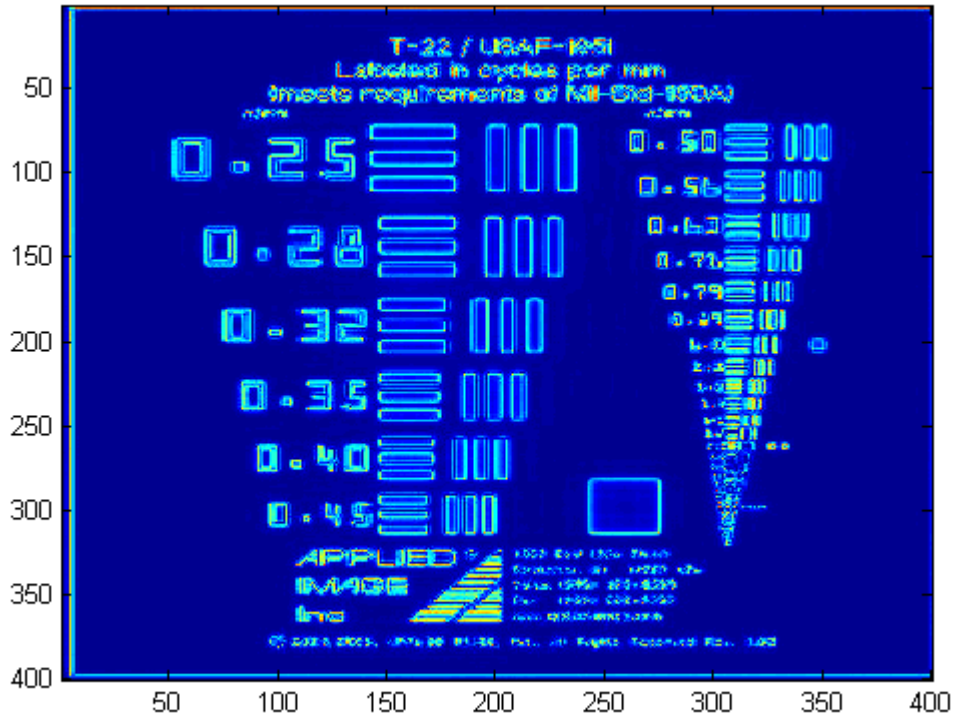
Figure 4.20: A simulated image from a data set in which the cone of missing information has been removed. The high spatial frequencies contribute to define the sharp edges.

Unlike the spatial frequencies ξ_1 and ξ_2, whose higher values survived and lower values were deleted, the spectral frequencies, ζ, were the opposite. The lower frequencies survived outside the cone, while more of the higher magnitudes fell inside the cone. The higher magnitudes would have allowed sharp spectral edges, i.e., the only information would be in the on-wavelength bins like in the original cube. With those removed, the spectrum took on edges that were much softer. As a result, the information was spread across a wide range of wavelengths by the low magnitude ζs. This was seen in both the unfiltered and filtered backprojections. Therefore, the strange appearances of the off-wavelength reconstructions were due in part to the cone of missing information. In

70

hyperspectral imaging, the intensities through the cube of one pixel that had white space should look exactly like a Neon emission spectrum in this example. Instead, it was a random assortment of intensities, consistent with what is seen in the cube with the cone deleted. An example spectrum is in Figure 4.21.
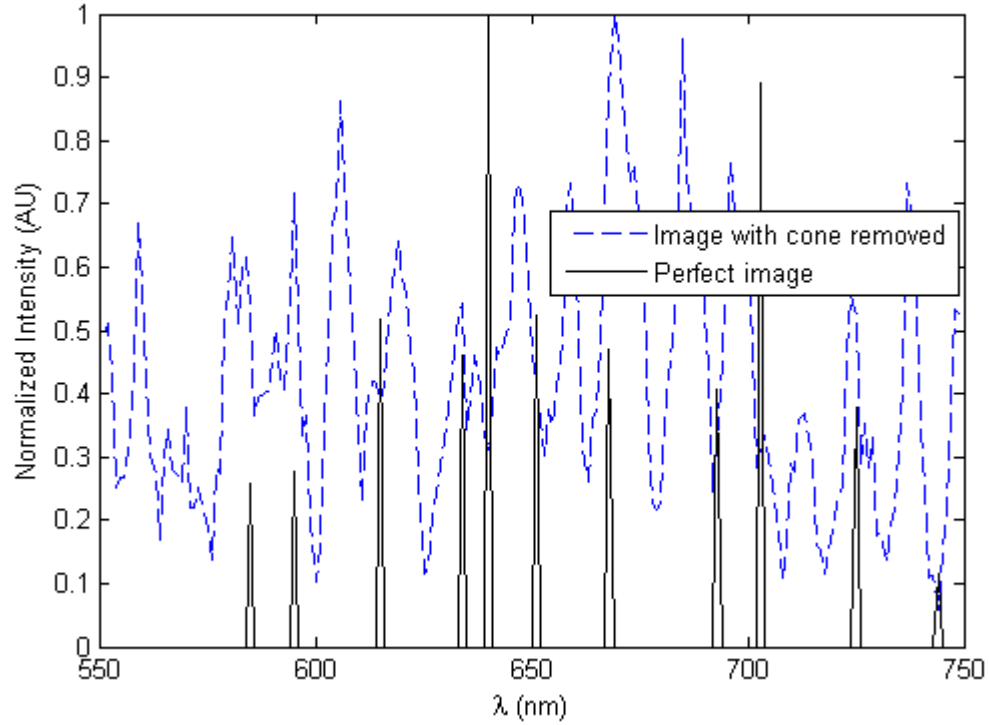
Figure 4.21: The spectrum of a randomly selected pixel that occupies white space in a simulated bar chart illuminated by a Neon pen lamp. This spectrum was taken through a hypercube from which the cone of missing information was deleted in Fourier space. The black peaks represent a true Neon emission spectrum.

4.2.5   Spatial Complexity Summary.

Table 4.3 summarizes the results of the spatial complexity section.   CTEx

successfully reconstructed 75% of the emission lines in the visible spectrum with the

Table 4.3: Summary table of the spatial complexity performance of CTEx. The image quality is purely qualitative.

	Pinhole	Hg Bar Chart (546, 435 focus)	Ne Bar Chart	Brain
Spectral Lines	75%	50%, 50%	28%	25%
Avg FWHM (nm)	5.0	9.0, 4.0	5.2	6+
Avg λ Error (nm)	1.7	2.0, 1.5	2.6	1.0
Image Quality	Great	Great, Fair (Poor w/ filter)	Good	Good (Fair w/filter)

pinhole. It only built half of the lines in both the bar chart with 546 and 435 nm in focus. It only built a unique line for 25% of the emissions in the complex brain scene. The average FWHM of the lines with the pinhole was 5.0 nm and accurate to within 1.7 nm. Its line width was 9.0 nm for the 546 bar chart and 4.0 nm for the 435. The widths were very large for the brain, but the peaks were the most accurate of all scenarios. The image quality of the pinhole was great for all scenarios. It built in-focus lines for the bar chart well, but significantly worse when using filtered backprojection on out of focus lines. CTEx did well imaging the brain, but only fairly when the filter was applied at out of focus light. The image quality metric was purely qualitative.

Figure 4.22 shows a summary of the main takeaways from the spatial complexity section. These images are of the Mercury lit bar chart focused at 546 nm. Only the reconstruction for that wavelength reproduced the bar chart. 435 nm had very poor focus, and no discernible bars were visible. The off-wavelength reconstruction also failed to make a perfect image, though the artifacts show some outlines of the bars as wavelengths
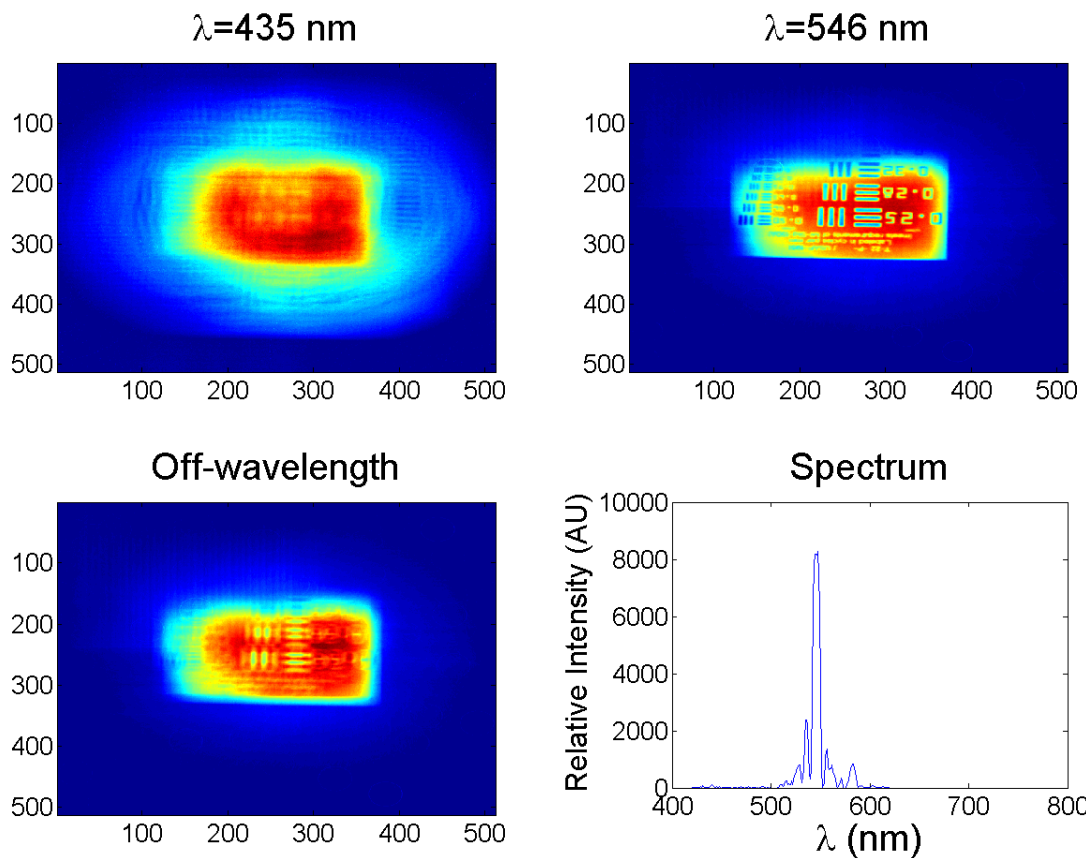
Figure 4.22: Summary of reconstructed bar chart reflections of a Mercury pen lamp. 546 nm was in focus, and it had a strong reconstruction. 435 nm was out of focus, and no discernible bars were visible. The off-wavelength reconstructions also did not reproduce the bar chart.

approach 546nm. The spectrum confirms no data at 435, and weaker reconstructions at wavelengths flanking the main lobe at 546 nm.

4.3   Image Quality vs Spectral Complexity

This section analyzes the results of experiments of increasing levels of spectral complexity. First, single atomic emission lines were examined, followed by the full spectral emission of a pen lamp. Varying degrees of filtered white light were then explored,

followed by unfiltered white light. Finally, the emission of the a fluorescent light bulb was used as a real world item. When possible, the scene was of a light source behind the pinhole. This allowed the spatial and spectral information to be separated to the greatest extent possible. Since each affected the other, separating them allowed for as much of an independent comparison of the system's ability to measure the reconstructed images' qualities as a function of spectral complexity.

4.3.1 *Atomic Lines.*

The most simple spectral scene was of a single very narrow atomic emission line. This was accomplished using a Mercury pen lamp emission with a filter combination that only passed 546 nm light. Mercury was used because there was enough spectral separation between emission lines to ensure the correct filter combination could be used to isolate only one line. One of the filters used in this section was a 530 nm long pass filter. Its transmission for wavelengths shorter than 530 nm was nominally 0, and constant for wavelengths longer than 530 nm in the visible spectrum (Figure 4.23). The other filter was labeled as a 550 nm short pass filter, only allowing wavelengths shorter than 550 nm to pass. After finding peculiar results in other tests leading up to this, the transmission of every filter used was independently measured with the spectroradiometer as described in Chapter 3. The 530 nm long pass filter proved to be as labeled. The transmission at shorter wavelengths was near 0 and about 0.6 at longer, with the transition spanning about a 40 nm band. The other filter did not transmit as expected. While it blocked the light longer than the labeled wavelength, the transmission was not constant for shorter λ. The machine used to measure the transmission of these filters was not equipped to hold two at the same time, so the combination was not measured directly. Instead, their transmissions were multiplied together. The result was a fairly uniform curve that looked like what a band pass filter would be expected to look like. The peak transmission was not ideal, however, because it was 537 nm. That was shorter than 546 nm, the wavelength of the Mercury emission line to be measured. Even though the
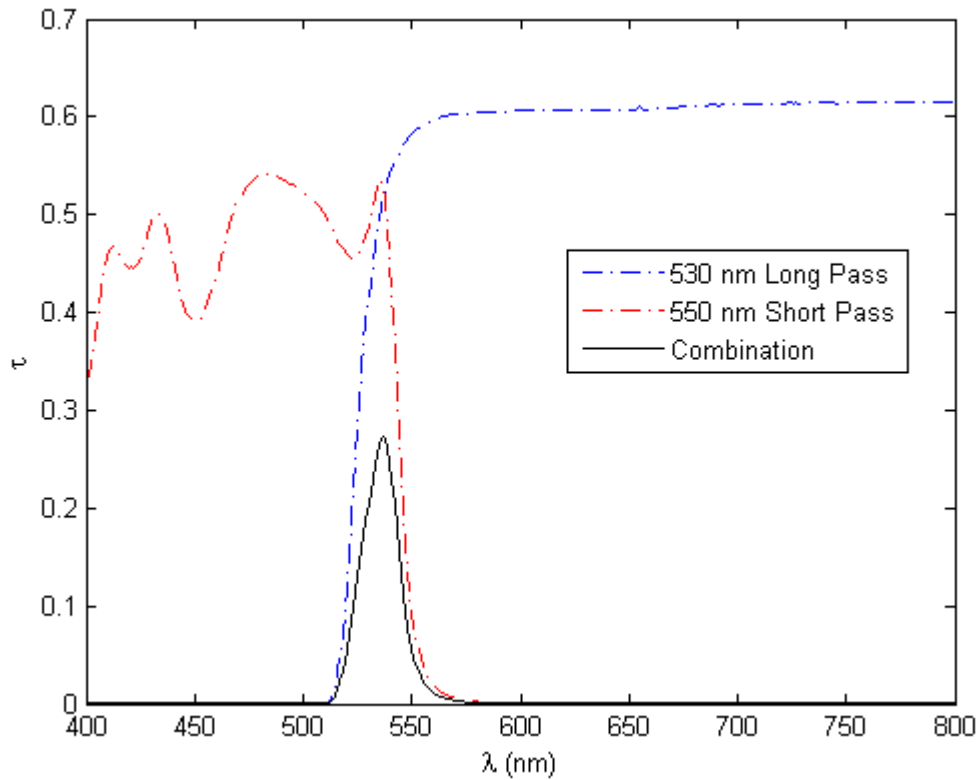
Figure 4.23: The measured transmissions of the 530 nm long pass and 550 nm short pass filters, and their combined transmission. The 550 nm short pass did not perform as expected, as the transmission was not constant for the shorter wavelengths.

emission line was very narrow [1], the shape of the line was distorted by the filter. Some of the more blue light (and noise) was artificially more intense than it should have been compared to the peak.

Figure 4.24 shows the reconstructed spectrum of the filtered Mercury light and the theoretical spectrum. The reconstruction used was the unfiltered backprojection, and the spectrum was built with the mean intensity technique. It cannot be called a truth measurement because it was not independently measured in its entirety. The transmission of the combination of filters was calculated as described above, and the spectrum was
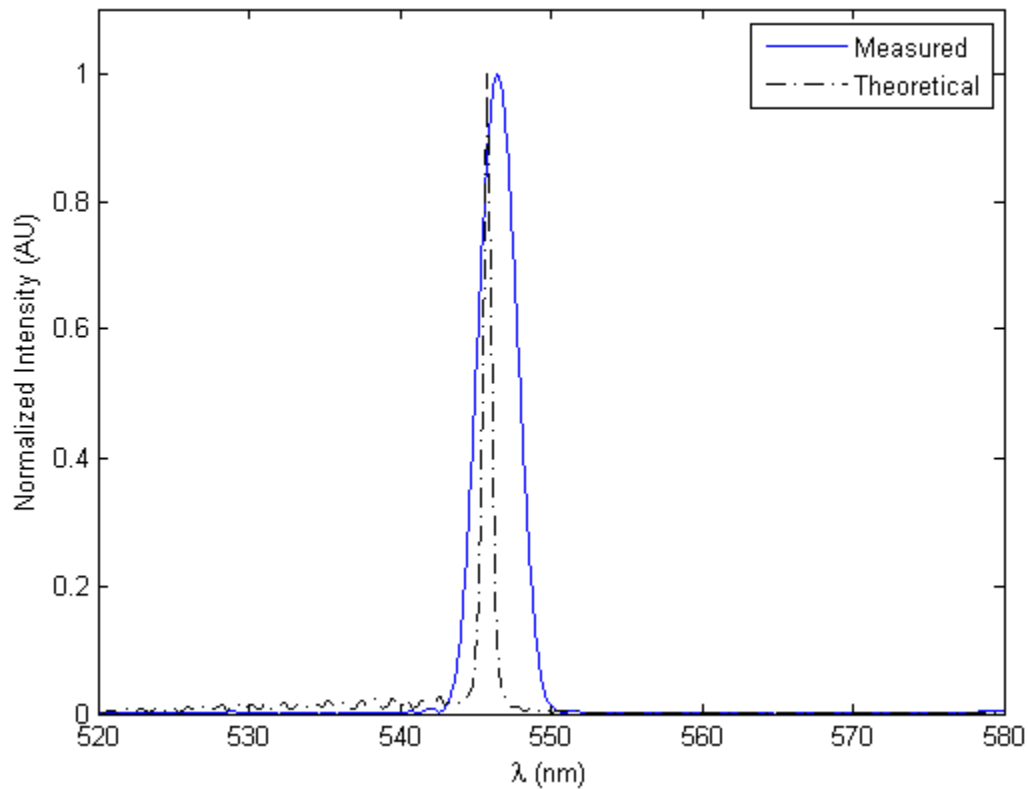
Figure 4.24: A comparison of the reconstructed spectrum using the mean intensity technique and the theoretical measurement of the 546 nm emission line of a Mercury pen lamp. The spectrum was measured with the mean intensity technique. The difference in measured and theoretical peak wavelengths was 0.6 nm.

independently measured with an Ocean Optics spectrometer. The intensity values of the spectrometer were multiplied by wavelength by the filter combination's transmission. The small oscillations in the theoretical line to the left of the main lobe were from noise in the Ocean Optics measurement. The peak of the theoretical curve fell at 545.8 nm. The measured peak was 546.4 nm, and that data was reconstructed every 0.2 nm. Even though the actual emission line was very narrow, the filtered independent measurement's FWHM was 0.6 nm. The FWHM of the reconstructed line was 3.0 nm.

The wider FWHM in the measured spectrum was because of the finite size of the spot on the FPA. Figure 4.25 shows a zoomed in view of the reconstructed image at the peak wavelength. The footprint of the entire emission line fell on a 4x4 pixel square, with a
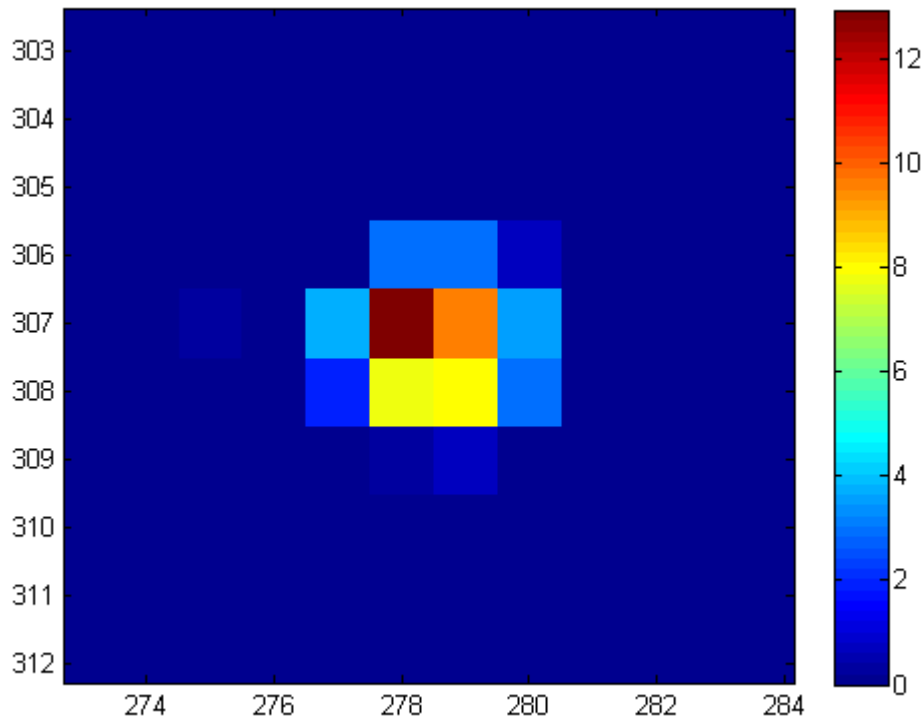
Figure 4.25: A zoomed in image of the 546.4 nm reconstruction of a Mercury pen lamp. The pixel nature of the focal plane array contributed to line widths. The color scale is in arbitrary units of pixel brightness.

vast majority of the energy in the central 2x2 pixel area. In fact, the region used in the mean intensity technique was that 2x2 area. For this case, a spot size of 2 pixels predicts the width to be 2.8 nm from Figure 3.6. The measured width was 3.0 nm.

4.3.2 *Pen Lamp.*

The next level of spectral complexity still involved the emissions of a pen lamp but with its entire visible spectrum. Since it was shown in the previous section the CTEx system could reconstruct a single emission line, a spectrum with more lines spaced more closely together was desired. The Mercury spectrum's lines were spaced far apart (much greater than the spectral resolution of the system), so Neon was chosen. Table 3.1 shows Neon has emission lines concentrated in the red end of the spectrum. Mercury's emissions were all shorter than 600 nm, and it was postulated that the spectral resolution would be better in that regime because of the dispersion of the prism. Neon has lines that are within 10 nm of each other. The results would indicate whether or not the system can resolve these wavelengths in the red.

A 12 nm bandpass filter centered at 641 nm was placed behind L_2. This isolated what was expected to be the brightest emission line at 640.2 nm. The focus of the system was then optimized for that point. The spectrum of the pen lamp was again measured independently by the Ocean Optics spectrometer, and is shown as the dashed black line in Figure 4.26. The spectrum created from the unfiltered backprojection using the mean intensity technique is shown in the solid blue line. Both the CTEx and the independent spectra were normalized so each one's maximum intensity was 1. The CTEx data was reconstructed every 0.5 nm, and the area was 3x3 pixels. Most of the independently measured peaks were matched to a peak from the reconstruction. The biggest spectral difference in peaks was 2.7 nm in the area of 614 nm. Up until the 668 nm emission line, each of the CTEx reconstructions fell at shorter wavelengths than the truth measurements. They were an average of 2.0 nm shifted to the blue. Every peak after that was within 0.5 nm of the spectrometer measurement. The entire spectrum had an average wavelength error of 1.4 ± 1.0 nm. The average line width was 8.9 ± 3.2 nm. The true and reconstructed wavelengths and reconstructed line widths are in Table 4.4. If it was not possible to get

78
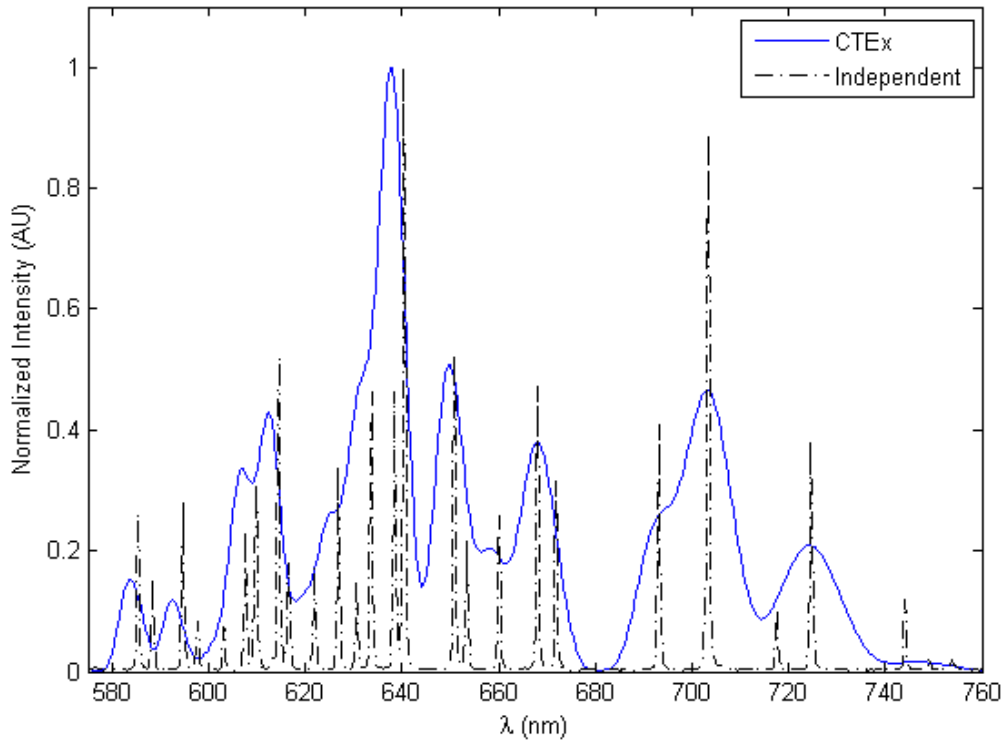
Figure 4.26: A comparison of the reconstructed spectrum and an independently measured spectrum of the emission of a Neon pen lamp. The CTEx spectrum was consistently at slightly shorter wavelengths than the truth measurement up until 668 nm. Though the entire visible spectrum was measured, this scale was chosen to show detail. All other wavelengths were of 0 intensity. The area of reconstruction was 3x3 pixels.

the FWHM of a line, its half width half max was multiplied by 2. Those lines are indicated with a *. The predicted widths were from Figure 3.6 with a 3x3 pixel area.

In addition to reasons discussed earlier, the distribution of energy was another potential explanation to the wavelength difference between the measured and truth spectra. Notice in Figure 4.26 that the CTEx curves that were offset to the blue end also had some peaks from the independent measurement adjacent to them. Most of the adjacent peaks were not resolved, but they still contributed to the energy used to build the blue curves. They tended

Table 4.4: Table of the line widths and differences in peak intensities for an unfiltered backprojection of a Neon lamp behind a pinhole and an independent measurement. The widths with a * indicate the half width half max multiplied by 2. The predicted widths are from Figure 3.6 with a 3x3 pixel area.

| | | | FWHM (nm) |
Reconstructed λ (nm)	Spectrometer λ (nm)	Difference (nm)	Measured, Predicted
583.5	585.4	1.9	5.8, 5.6
592.5	594.6	2.1	5.2, 5.8
607.0	609.7	2.7	7.6*, 6.5
612.5	614.6	2.1	5.8*, 6.7
625.5	626.8	1.3	-
631.5	633.7	2.2	-
638.0	640.3	2.3	8.6, 7.9
650.0	650.8	0.8	7.8, 8.4
658.0	660.2	2.2	-
668.0	668.0	0.0	10.2, 9.2
693.5	693.1	-0.4	10.0*, 10.6
703.0	703.5	0.5	12.0*, 11.2
724.5	724.6	0.1	15.7, 12.5
-	-	Avg=1.4	Avg=8.9, 8.4

to be at wavelengths slightly shorter than the measured peaks, which would have shifted the energy to the blue. After the gap at 680 nm the peaks became more spectrally separated. 2 out of the 3 measured and independent peaks agreed nearly perfectly. The discrepancy in the 724 nm light also had an adjacent peak at a slightly shorter wavelength.

While every peak in the spectrometer measurement was a sharp line, the reconstructed spectrum was a series of softer and wider lines. The lines at 580 nm were also much more narrow than those in the 725 nm range. The most narrow FWHM occurred at the 584 nm emission, and was approximately 6 nm. Conversely, the widest was at the 724 nm emission at about 16 nm. The reason for this can be explained by the dispersion curve in Figure 2.3. The longitudinal dispersion of the prism changed much more slowly in the red end of the spectrum than it did in the blue end, so the range of wavelengths on a single pixel was more in the red spectrum than in the blue. When the algorithm shifted the image to the next wavelength, that might have equated to a distance of less than 1 pixel. Therefore, that next wavelength may have been on the same pixel, causing the line to broaden. Additionally, the focus was set so the 641 nm emission line was sharpest. The red wavelengths were further away spectrally, so their focus quality was worse than blue, also seen in Figure 4.27.

There were also not as many unique lines that were resolved according to Rayleigh's criterion in the reconstructed spectrum as there were in the independent spectrum. Figure 4.27 illustrates the reason why.   This is a raw image taken from a frame of

Neon emission video used to build the spectrum. The upper-right area was the 584 nm emission and the lower left was the 724 nm. In most cases, there did not appear to be a clear distinction between individual emissions. The distribution of energy across the spectrum was almost continuous, causing very few wavelengths where the spectrum actually went to 0. A notable exception was the gap between the 671 nm and 693 nm emission lines. The CTEx spectrum showed at least 8 distinct peaks. There were several other humps that didn't meet Rayleigh's criterion as being distinct, but could still be matched to a line in the truth spectrum from the independent measurement.

Finally, the plots in Figure 4.26 were normalized so each maximum intensity was 1 on an arbitrary scale. Their relative intensities were forced to match up at the point of best focus, 641 nm. With perfectly imaged points in the rest of the scene, the other
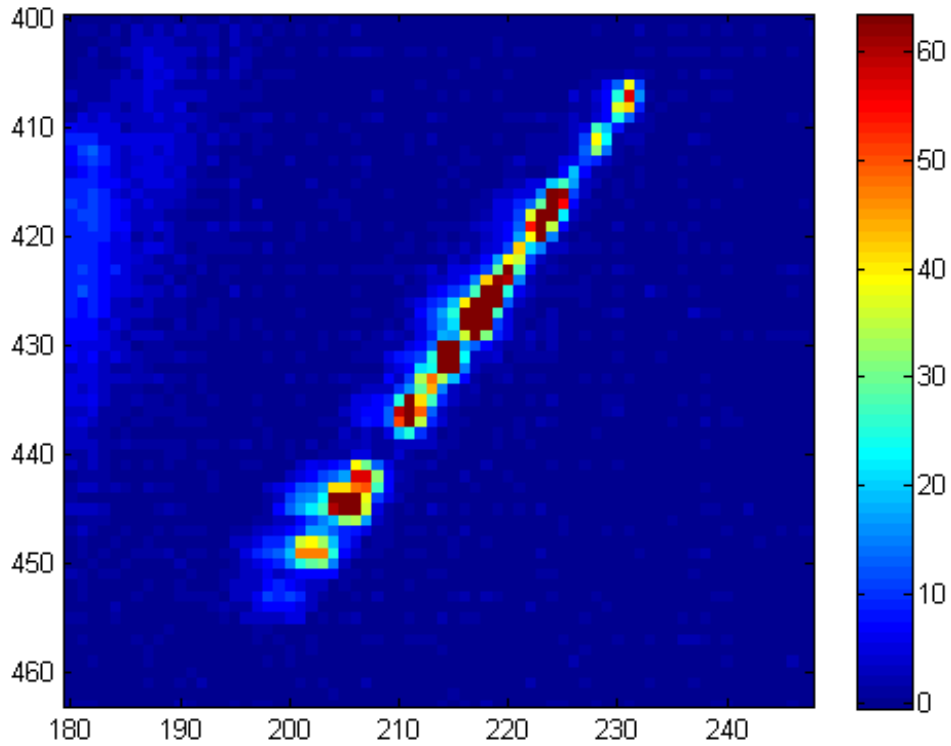
Figure 4.27: A zoomed in view of a raw frame from the Neon pen lamp behind a 25 μm pinhole. The shortest wavelengths are in the top right and the longest are bottom left. The almost continuous distribution of energy across the spectrum was why many lines peaks from the CTEx reconstruction in Figure 4.26 were not resolved.

intensities were expected to match as well. Some CTEx peaks came very close to matching the independent intensities, and others weren't even close. The lines were shorter and wider because of the widening inherent in the spectrum building method, the dispersion relationship discussed previously, and because of the focus. The peak at wavelengths longer than 740 nm might not have even registered in the reconstructed spectrum. Not only were they very dim, but the spectral response of the camera was at its lowest there (Figure 4.3). The discrepancy in peaks was bigger the further away from 641 nm the

spectrum was, as was the amount of defocus. The focus and the dispersion curve's effect on spectral resolution, as well as the reconstruction technique's limit on line width, all likely contributed to the disparity in peak intensities and widths.

4.3.3 Filtered White Light.

More spectrally complex than reconstructing the emission from a pen lamp is to reconstruct a white light source that has been optically filtered. The white light source was a Fiber-Lite brand source. Its spectrum was measured with the Ocean Optics spectrometer and is shown in Figure 4.28.   The spectrum shown was averaged over 10 separate
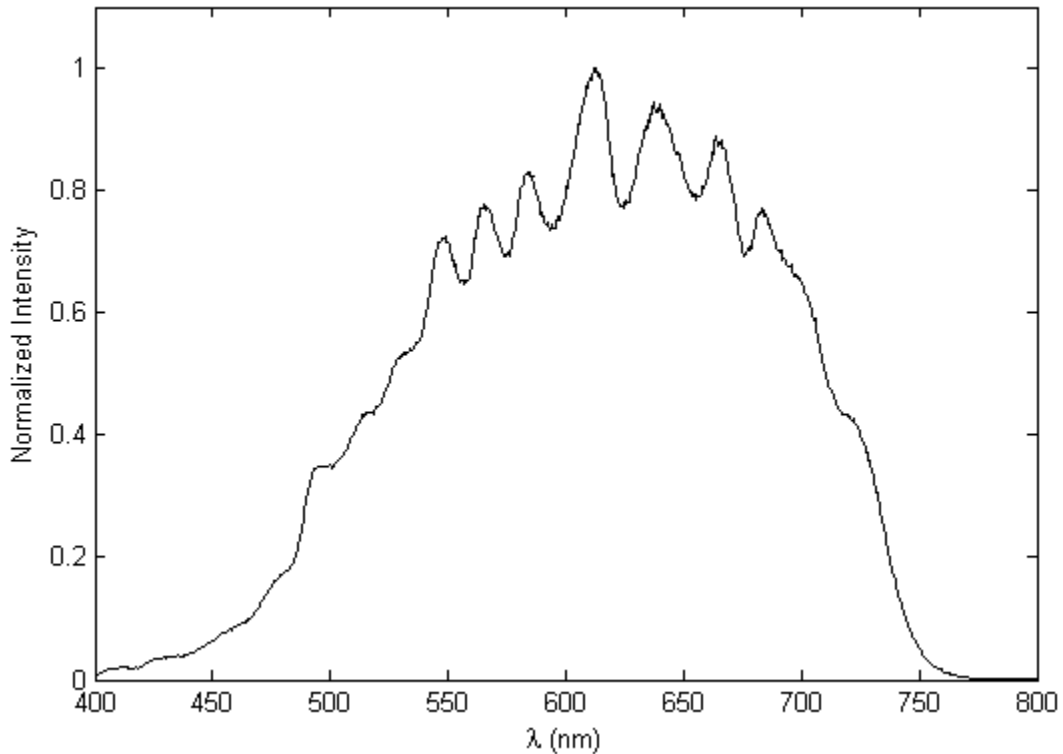
Figure 4.28: The spectrum of the Fiber-Lite white light source measured with the Ocean Optics spectrometer multiplied by the spectral response of the camera. The spectrum is averaged over 10 separate measurements to smooth out some of the instrument noise.

measurements to smooth out some of the noise. The small individual spikes were noise that survived averaging, and longer humps were multiplied in from the spectral response of the camera. Since the spikes were no more than 2 nm wide (well within the spectral resolution determined in Table 4.1), more measurements weren't taken to further reduce the noise. This smoother curve was used for every white light source in this section.

4.3.3.1   12 nm Band Pass Filter.

Several different filter combinations with different bandwidths were used to evaluate the system's ability to reconstruct the filtered white light source, each with increasing bandwidth. The first tested was the white light source and the 12 nm bandpass filter centered at 641 nm used in the Neon pen lamp experiment. The left plot in Figure 4.29 shows the comparison.   The reconstructed spectrum was built with the mean intensity
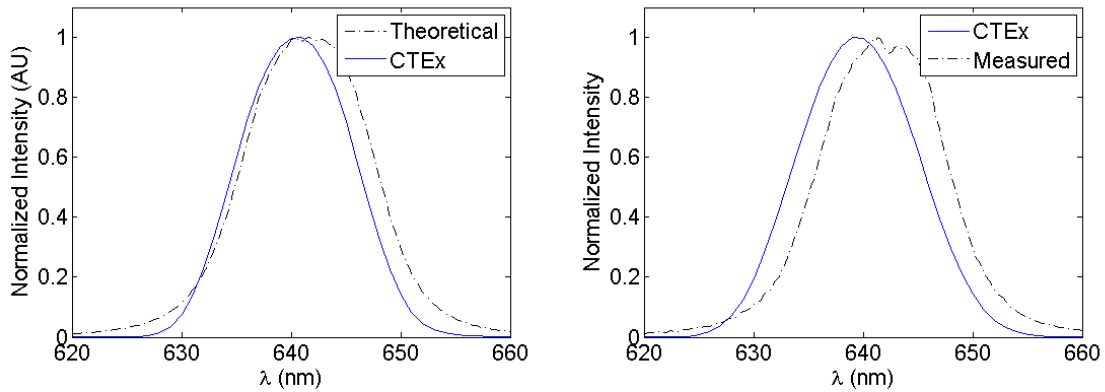
Figure 4.29: (L) The comparison of the theoretical curve of the white light source with a 12 nm bandpass filter and the curve measured from the CTEx reconstruction. The FWHM of the measured curve was smaller than the theoretical curve. (R) To test repeatability, a separate data set was taken. The line widths were roughly the same. The CTEx curve was always expected to be wider than the theoretical curve.

technique using a 2x2 pixel area. It was reconstructed every 0.5 nm. The theoretical curve

was achieved by multiplying the measured transmission of the filter by the spectrum of the white light source. The peaks of the curves were only 0.6 nm apart, but the theoretical FWHM of the theoretical curve was wider than the CTEx curve - something the model (and intuition) did not predict. The width of the experimental line was approximately 12.3 nm. The width of the theoretical line was 13.4 nm. The theoretical curve represented the best case scenario. There were no optics to deform the image. There was no reconstruction algorithm that may have contained wavelength errors, nor a prism with a slowly changing dispersion curve in this spectral region. If a beam is not perfectly collimated, it will appear to have a larger bandwidth after passing through a filter. This is one possible explanation, but not likely since the effect was not consistently seen throughout the project.

To see if these results were repeatable, another data set was taken. The plot is the right side of Figure 4.29. For that plot, the actual spectrum of the filtered white light source was used. Instead of measuring the spectrum and filter transmissions separately and multiplying them to get a theoretical curve, the spectrum was measured with the Ocean Optics spectrometer while the filter was in place. The top of the curve had a little more noise in it than the previous run because there weren't multiple data sets to average it out. The result was a line that was slightly more narrow (13.2 nm). The maximum intensity was a little bit different, probably a result of the noise. The center of the curve was still at 641.9 nm, the same as the first measurement. The CTEx experiment was also run another time. The white light source was placed behind the pinhole and the filter behind L_2. Extra care was taken to ensure the light in this band was at its best focus possible. The FWHM widened out to 13.0 nm, and the center of the line shifted slightly toward the blue end; the wavelength difference was still within the range seen in other experiments. Still, the optical principles predicted the shape of the line to be wider than the ideal case, and it was not.

The areas used to develop the CTEx curves were 2x2 pixels. The area was selected because a zoomed in view of the reconstructed region looked similar to the image in

85

Figure 4.25, but a little brighter outside the central region. The assumption was the light going through a pinhole and a filter with only a 12 nm bandwidth would look like a pen lamp emission. However, the pen lamp emission lines were essentially delta functions. The white light source was continuous over the band. Any light outside the central bright point was actual spectral data, and not a blurring of the energy from the optics. A wider area needed to be included in the mean intensity calculation. When it was expanded to a 4x4 pixel area (the approximate area of the spot in the raw data), it produced the plot in Figure 4.30. The plot with the 2x2 pixel area was included for comparison. It was again
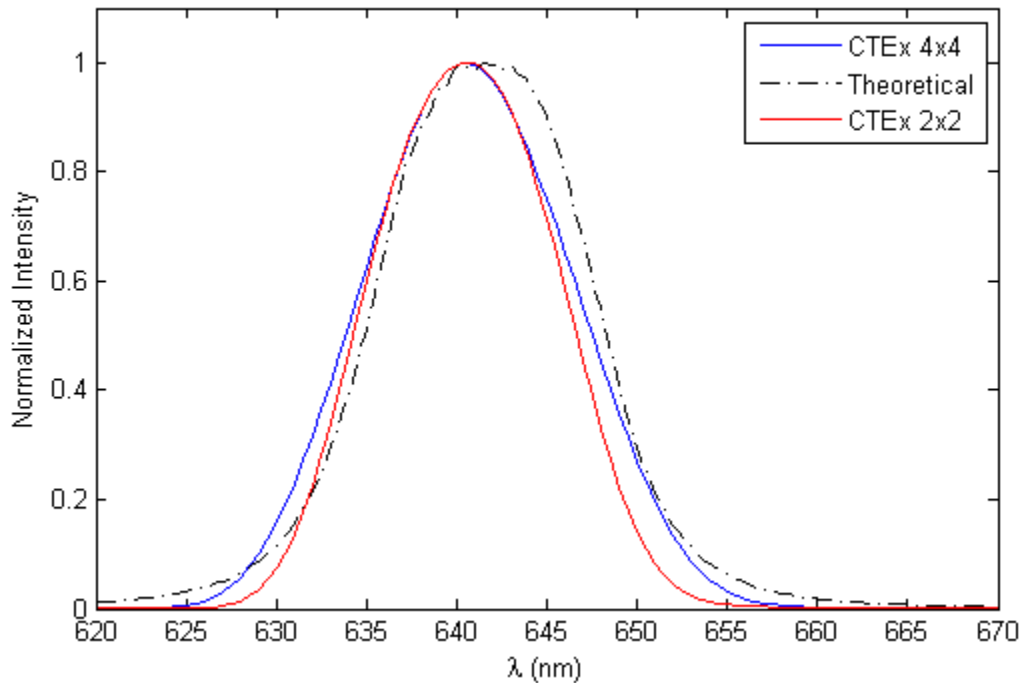
Figure 4.30: The 4x4 and 2x2 pixel CTEx spectra and the theoretical spectra of a white light source filtered by a 12 nm bandpass centered at 641 nm. Since the 2x2 area line width was smaller than the theoretical width, it was the wrong choice of area to use. The 4x4 line width was bigger than the theory.

graphed with the theoretical curve for this situation to show a comparison of the line widths. The reconstruction showed the same blue shifts as before. The 4x4 reconstruction's width, 13.6 nm, was bigger than the width of the theoretical and truth lines of 13.4 and 13.0 nm, respectively. The 2x2 reconstruction's width was 12.2 nm. All results are in Table 4.5.

Table 4.5: Table of the line widths and differences in peak intensities for an unfiltered backprojection of a Mercury lamp behind a pinhole and an independent measurement. Using a bigger area made the reconstructed lines wider than the theoretical, as it should have been.

Line	Peak Wavelength (nm)	Line width (nm)
Theoretical	641.6	13.2
4x4	641.9	13.6
2x2	641.9	12.2
7x7	641.9	22

Because of degradation from the optics alone, it would be impossible for the line width to be more narrow than the true width. Though it finally agreed with expectations, it is not known how accurate the measurement was. The region only included the brightest pixels. If the area selected covered every pixel that had an intensity greater than 0 in the reconstruction, it would have covered a 7x7 pixel space. The line width of that was $\approx$ 22 nm. In every case, it was difficult to know which pixels were signal and which were artifacts. Selecting the proper area was extremely important to achieving accurate results, even in the simplest spatial case of a pinhole.

4.3.3.2   50 nm Band Pass Filter.

Another scenario of slightly more complex spectral features was to use the 500 nm long pass-550 nm short pass filter combination. The center wavelength was different and the bandpass was larger, but the behavior was expected to be very similar to the previous iteration. The transmission curve of the combination is in Figure 4.31.   The
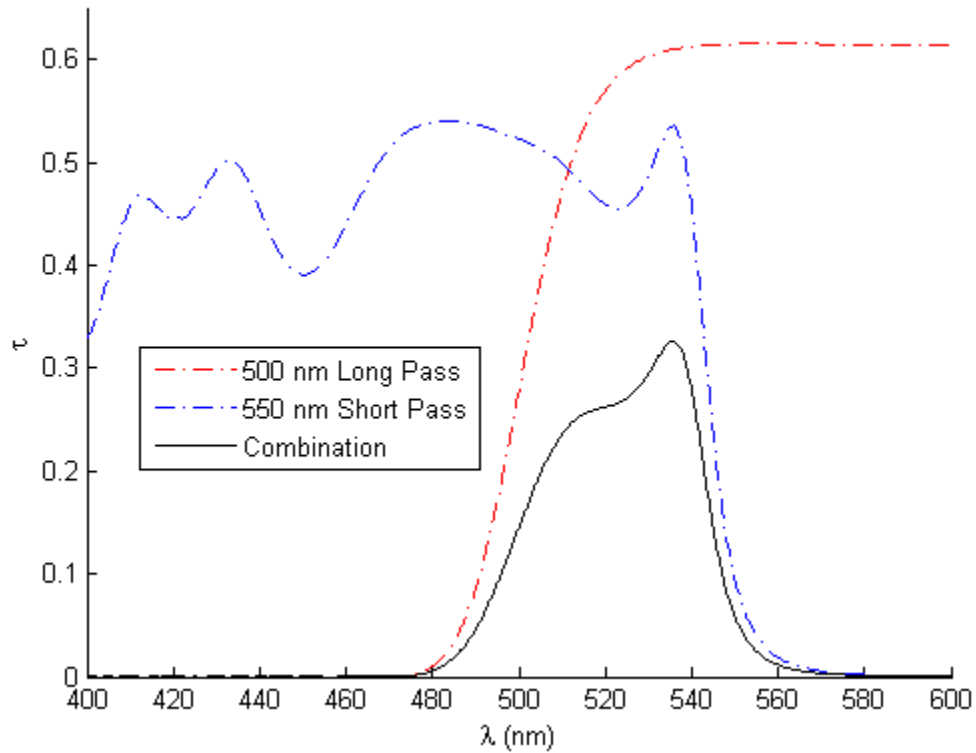
Figure 4.31: A plot of the transmissions of the 550 nm short pass filter, the 500 nm long pass filter, and their combination. The odd transmission curve for the short pass filter was responsible for the asymmetric transmission of the combination. This combo was selected to determine if the CTEx system could reconstruct a similar spectrum.

combination curve was calculated again by multiplying the transmissions of the individual filters. The jog in the transmission near 520 nm provides an interesting feature to test how

well CTEx preserves line shape. Had the transmission been of similar shape to Figure 4.23, a discussion would not have been necessary. The typical experimental configuration with the white light source and the 25 μm pinhole was used. The 546 nm light remained in focus because it was easy to confirm. The wavelengths in focus were expected to have a higher relative intensity compared to the theoretical curve based on what was learned in the previous sections. It was also impossible to know exactly when the center of the band was in focus because the continuous source did not provide any spatial markings.

The theoretical and reconstructed spectra are shown in Figure 4.32. The camera
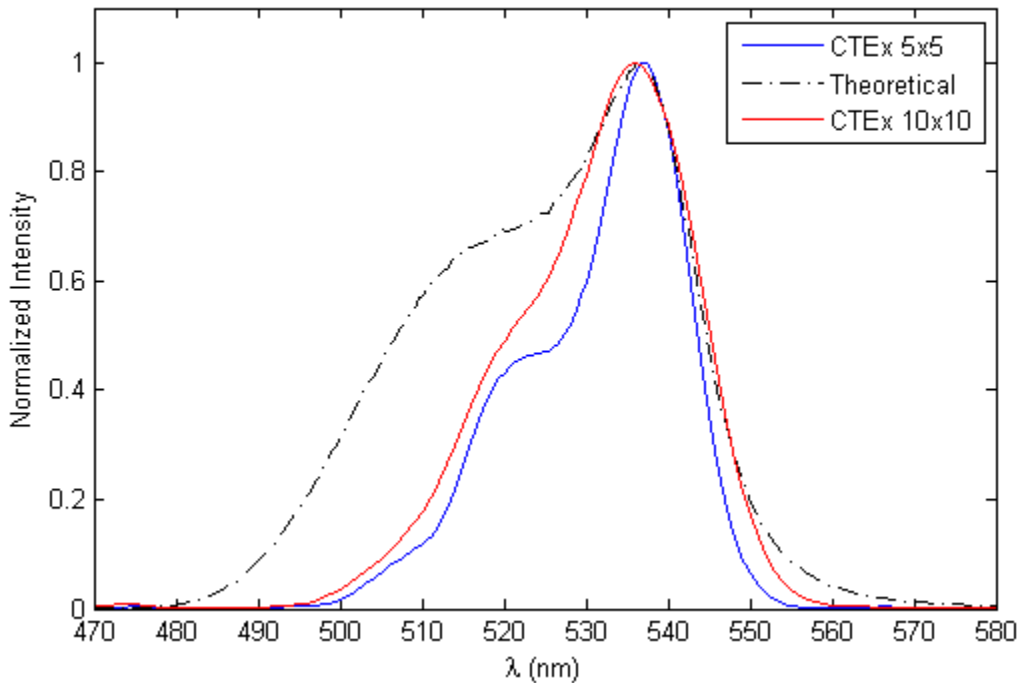
Figure 4.32: A plot of the CTEx and theoretical curves of filtered white light. The filter bandwidth was 50 nm centered at 525 nm. The 5x5 pixel area reconstructed curve mimicked the shape of the theoretical, but it was much more narrow, and the jog occurred at a lower intensity. When the region was increased to 10x10 pixels, the jog almost disappeared. The camera response was included in the figure.

response was included in the theoretical spectrum. The reconstruction clearly shows a similar shape to the theoretical spectrum. The jog from the asymmetric shape of the filter combination's transmission was present at roughly the same wavelength and the peak intensities were a mere 0.2 nm apart. A glaring difference was in the overall width of the lines. The theoretical line predicted a much wider curve than the reconstructed one produced. The area of mean intensity shown was a 5x5 pixel area. Originally, a smaller area was used, which revealed the unique shape. After realizing from experience that area was likely too small, it was increased to 10x10 pixels. In that area, the jog all but disappeared. The curve had a gradual and nearly constant increase until it reached a maximum at 536 nm, followed by the sharp decline seen in Figure 4.32. The jog also occurred at a smaller intensity relative to the maximum in the reconstructed data. That was most likely because it was out of focus, reducing the mean intensity, and because the area used to calculate the mean intensity was too small. The linewidth was more like the theoretical's as the area of mean intensity increased, but affected the shape's integrity. The curve's similar shape to the theoretical proves AFIT's CTEx system is capable of discerning intensities that change with wavelength in a continuous spectrum. Questions still remain which region of pixels to choose when building the spectra.

4.3.3.3   550 nm Short Pass Filter.

Examining the spectrum in Figure 4.32 begged the question of how CTEx would reconstruct the filtered white light spectrum with only the 550 nm short pass filter in place. Figure 4.33 shows the the CTEx reconstructed spectrum using mean intensity, the theoretical curve, and the relative transmission of the filter for reference and a reminder. In this plot, the white light source data was not only multiplied by the filter transmission, but also by the camera's spectral response curve. The area used for calculating mean intensity was 4x4 pixels. The peaks of the CTEx and theoretical peaks lined up well with the highest transmission near 540 nm. They also dropped to 0 almost perfectly with the filter curve.

90
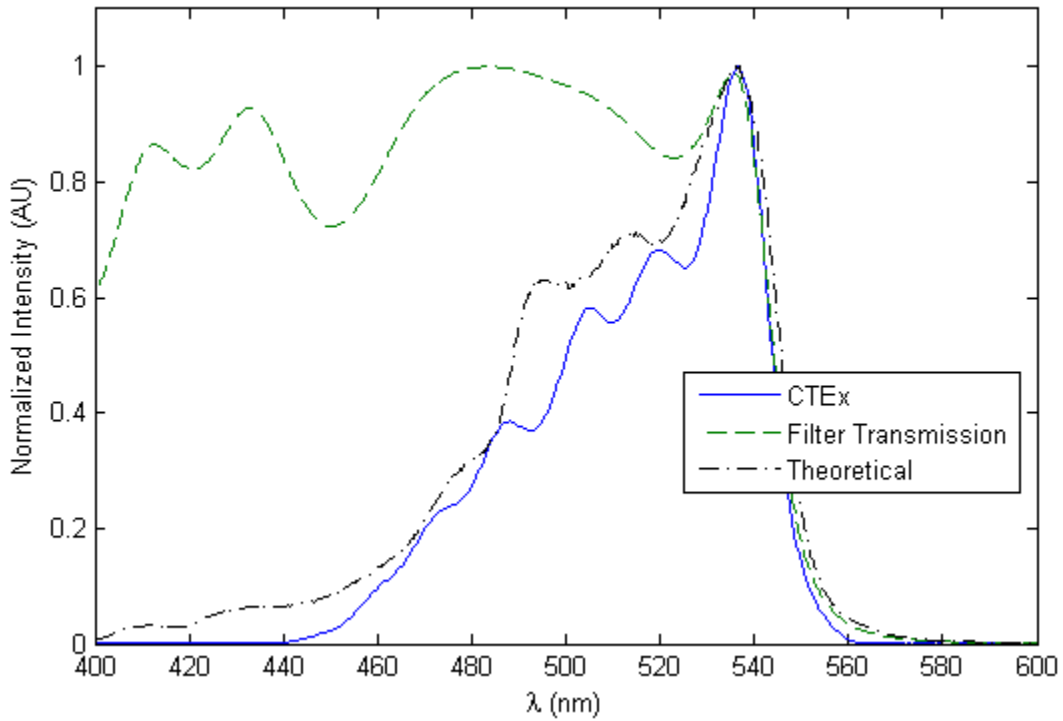
Figure 4.33: The filtered white light source with the 550 nm short pass filter in place. The reconstructed shape roughly matched the theoretical shape. The waves from the reconstructed shape were from the spectral response of the camera. The white light source data was multiplied by the camera's spectral response curve.

The spectra deviated rather quickly in the shorter wavelengths. The system was focused on the brightest section of the continuous emission, at 537 nm. Since the short wavelengths were out of focus, the energies from those wavelengths were spread out, and their relative intensities were smaller than the predicted curve's. That is why the envelopes did not match. The theory predicted the intensity decrease to 0 as the source spectrum did. CTEx went to 0 more quickly than the theoretical spectrum and took on a wave-like quality.

The waves did not correspond to waves in the filter. To investigate the source of the waves, the raw video data was examined. When zoomed in, the intensity of the spectral

91

data fluctuated with pixel position. Figure 4.34 shows a frame from the video with an extreme zoom in the x direction. There were only 9 out of 512 pixels in that dimension.
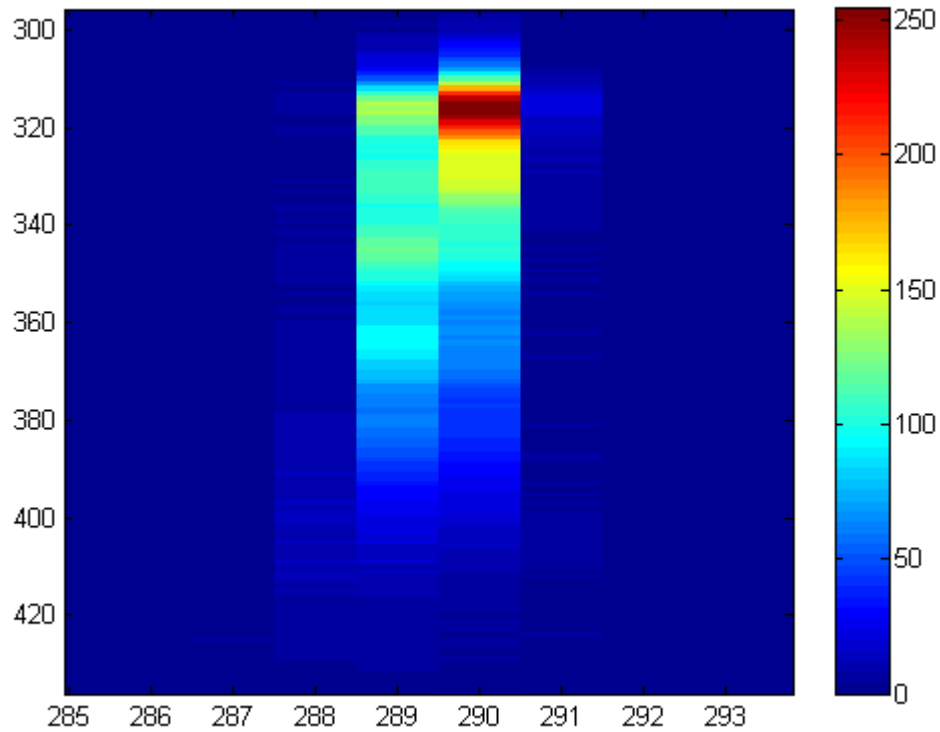
Figure 4.34: A zoomed in view of a frame from the raw data. In columns 289 and 290, fluctuating intensities can be seen, which explains the waves in Figure 4.33.

The frame was selected because of the angle of dispersion was 180° with the shortest wavelengths at the bottom of the frame. Essentially putting the data into columns made it easier to see intensity patterns. Column 290 contained the brightest pixels and showed a little bit of fluctuation, but column 289 contained the majority of the wavy data. The raw frame confirmed that an oscillating intensity was actually recorded and wasn't an error in reconstruction. Notice also that spectral data was present in 4 pixels. This was the width

92

of the data and confirmed using a 4x4 pixel area was likely the correct choice in this data set. Refer to the spectral response curve in Figure 4.3. According to the specifications from the camera's manufacturer, the spectral response of the camera was wavy for the entire visible spectrum. The waves in the CTEx curve roughly correlated to the theoretical white light source with the response accounted for. A more in depth discussion of the spectral response's effect will be in the white light section.

4.3.3.4   *665 nm Long Pass Filter.*

The final section on the filtered white light investigated how the system handled a white light source with the blue and green light filtered out and only red light surviving. A 665 nm long pass filter was used. The filter's transmission curve did not have any unexpected features like the 550 nm short pass filter did; it rose steadily, starting at 0 and reaching 50% transmission at 665 nm. It remained relatively constant for the remainder of the visible spectrum. Since the white light source had a steep decline starting just on the blue side of 700 nm, the filtered product was expected to have a relatively narrow bandwidth. Figure 4.35 shows the theoretical and CTEx curves for this case.   The theoretical curve was produced by multiplying the filter transmission by the white light source emission and spectral response as above. The theoretical and 2x2 area curves matched closely as they rose from 0 energy and fell back down to 0. The similarities ended there. While the theoretical curve dropped off evenly with the white light source, the CTEx curve had 2 large humps. The first hump that seemed to correspond to the maximum intensity of the theoretical curve was shifted toward the red when compared to where the smooth theoretical curve would have been. There did not appear to be any second local maximum in the theoretical curve. As with the 550 nm short pass filter, the ripple was due to the spectral response of the camera.

When a larger area was used, the intensity of the 2nd local maximum increased to nearly the same value as the global maximum. The red curve did not completely level

93
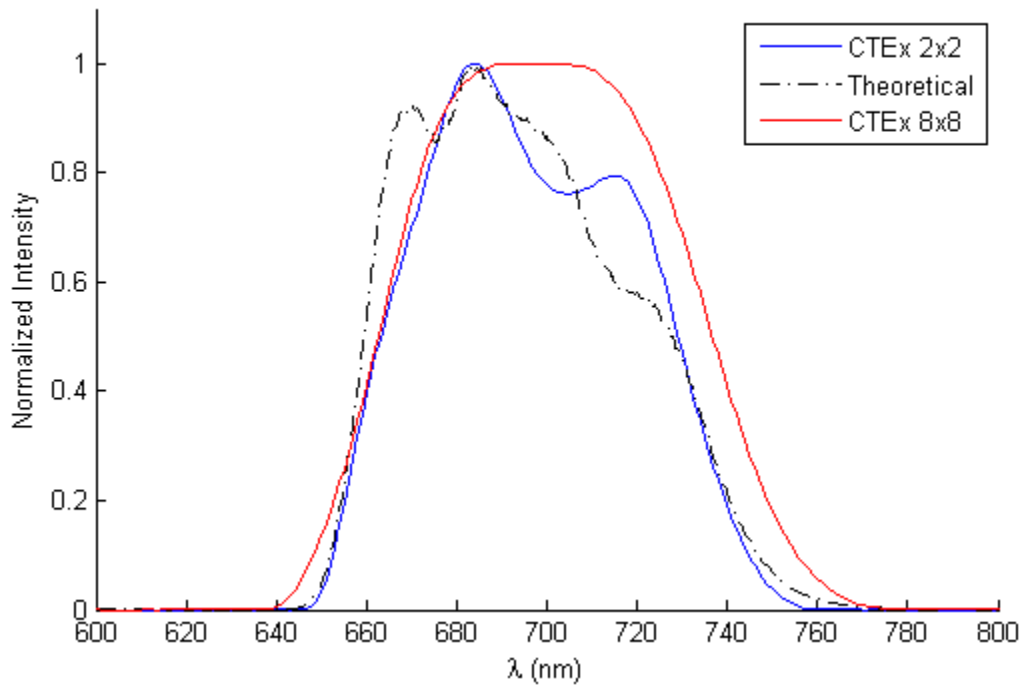
Figure 4.35: The theoretical and CTEx-created spectra of a white light source behind a 665 nm long pass filter. The blue curve used a 2x2 pixel area to match the theoretical shape. The red used an 8x8 area to match the light's footprint on the FPA.

off. The dip was still present, though very hard to detect without the use of MATLAB's value finding feature. Not only did the relative intensity of the secondary peak increase; the intensity relative to the max of the entire CTEx curve increased, as evidenced by the curve not rising and falling with the theory as closely as the curve with a smaller mean intensity area. The technique was adequate for finding the relative locations of spectral information when reconstructing a point source, but selecting the proper area remained paramount if reconstructing the exact spectrum was desired.

4.3.4 White Light.

The most complex spectral scenario done with laboratory light sources was of a white light source without optical filters. Since there were no filters with odd transmission

curves or to block any of the light, the shape of the spectrum was initially expected to at least follow the envelope of that in Figure 4.28. After running the experiments with the filters, it was evident that the CTEx spectrum might have not matched perfectly with the independent measurement, but it would have been close. Figure 4.36 shows the results of the reconstruction. The solid lines were reconstructed with a 4x4 pixel area using the
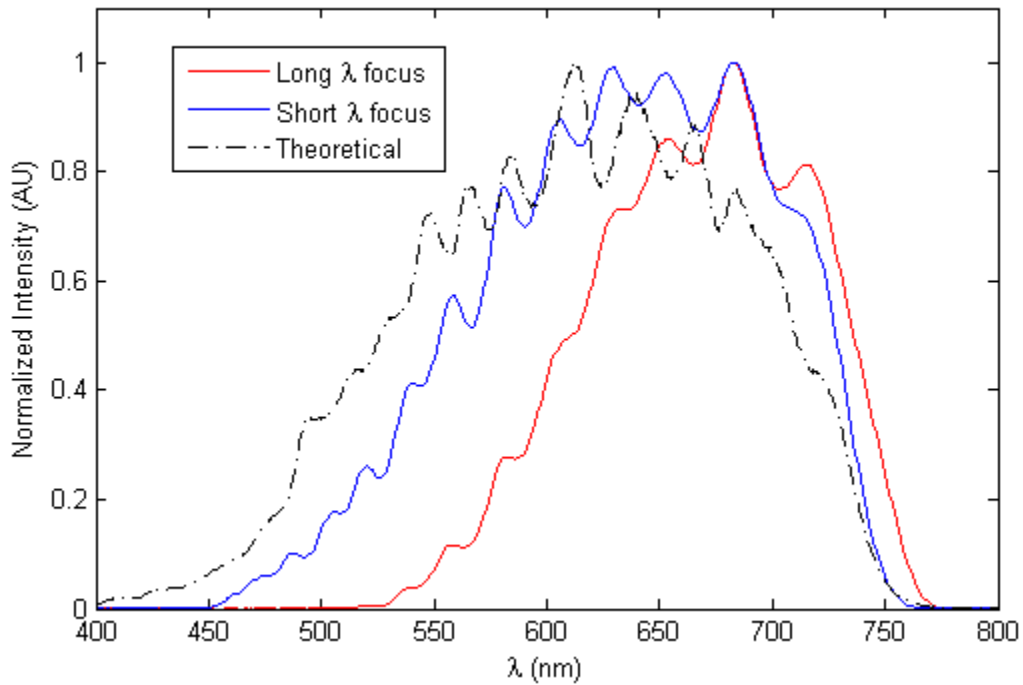
Figure 4.36: A plot of the white light source theoretical spectrum, the CTEx reconstructed spectrum at a short wavelength, and at a long wavelength. The fluctuating curves were consequences of the camera's spectral response curve, but did not line up exactly with the theoretical spectrum. Despite being focused at two very different points, the two CTEx spectra had maxima at the same wavelength. They were different from the predicted maximum intensity, which was in between the two wavelengths used to focus CTEx.

mean intensity technique. The dashed line was the theoretical spectrum, and is a reprint

of Figure 4.28. It is shown again for easier comparison and reference. At first, only the red curve was presented. It looked a lot like the spectrum in Figure 4.35 at wavelengths longer than 665 nm, but it extended beyond the edge of the theoretical curve - much more than in Figure 4.35. This was because the foci of the two measurements were different. While Figure 4.35 was focused on 641 nm, the red line in Figure 4.36 was focused on the best overall focus of the scene. That was obviously at some wavelength longer than 665 nm, so the colors further toward the edge of the spectrum were imaged with higher intensities, pushing the envelope out. When the short wavelengths in the curve fell well inside the theoretical curve, another data set with a blue wavelength in focus was taken. The blue curve represents that data. It was taken with the same parameters as the curve in Figure 4.33 with the filter removed. Its shape had the exact features of that curve at wavelengths shorter than 550 nm when compared to the theoretical line. At the red end of the spectrum, the blue curve had the same hump that extended beyond the theoretical curve, then followed it closely to 0 intensity.

The spectral response curve is wavy over the entire visible spectrum. Based on the system's demonstrated spectral resolution, the wavy features in Figure 4.3 roughly matched the CTEx waves in Figure 4.36. To further demonstrate the waves resulted from the spectral response instead of reconstruction errors, Figure 4.34 shows fluctuating intensities. It was a scene taken from the raw data and zoomed in to show the detail in the recorded data. Similar features were observed in the raw data for Figure 4.36. Another noteworthy feature was the red and blue curves having relative peak intensities at the same wavelength (683 nm) despite being focused on two different points in the spectrum. The peak intensity in the theoretical curve was at 613 nm. Even though the response dropped sharply after its max, it was still predicted to have a high reconstructed intensity. The local maximum of the blue curve at 629 nm had a normalized intensity of 0.9912, very close to the global maximum.

The red curve also had a local max there but was at a much lower intensity. It is not clear why the waves in the theoretical and CTEx curves did not match up.

4.3.5 Overhead Fluorescent Light.

In the final portion of the spectral complexity section, a real-world scenario was investigated. Instead of a laboratory grade light source, a commercial overhead fluorescent lamp was imaged. The spectrum of the lamp was independently measured with the Ocean Optics spectrometer and is shown as the dashed line in Figure 4.37. The lamp clearly had

Mercury vapor in it. There were large emission lines at 435 nm, 546 nm, and a doublet centered at 578 nm. Their relative intensities were similar to those in Figure 4.5. There were other lines from some other elements inside the lamp as well.

CTEx was focused on the 546 nm emission line because it was one of the most prominent features and easily verified by the Mercury pen lamp. It built a spike with the mean intensity technique at 543 nm. It was shifted towards the blue end like had been seen prior to this experiment. The shift was a little bit more than usual. The spike at 542 nm in the truth measurement was a culprit. Though its intensity was only about half of the Mercury emission line, it still added to the wavelength inaccuracy in peak intensity. The width of the CTEx line encompassed both the Mercury and other emission line. It did not detect the 435 nm at all. Since that light was out of focus, it was not expected to reconstruct to a peak as high as in the independent. It was expected to be on the order of the same wavelength in Figure 4.5, though. It also showed light at the 578 nm doublet. Its intensity was higher than the truth measurement, but also the width was wider. There were emissions from the other species inside the lamp near the wavelength that fell under the curve but weren't resolved by CTEx.

The most intense emission in the independent measurement came at 611 nm. Since that light wasn't in focus, it was not reconstructed as the brightest line. There was a dimmer line near 486 nm. It is difficult to say with certainty whether or not CTEx recognized it.

97
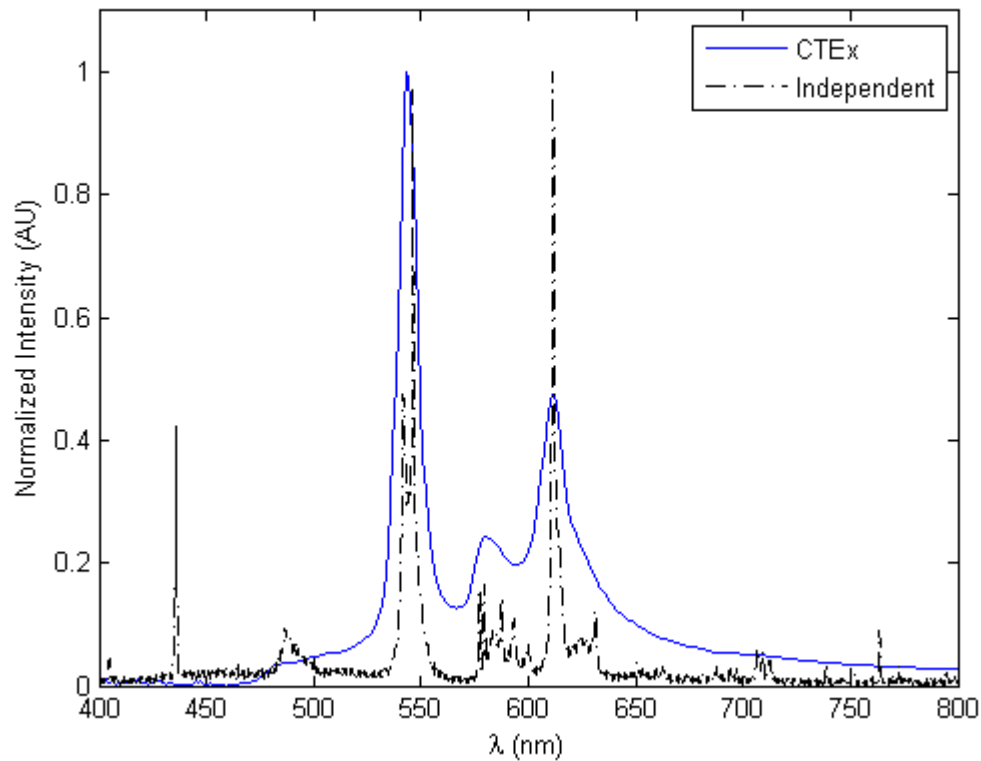
Figure 4.37: The independently measured spectrum of an overhead fluorescent lamp and its CTEx reconstruction. The truth spectrum had the same features as the Mercury pen lamp along with some other emission lines. CTEx was able to rebuild the major features of the spectrum, but it missed on some of the smaller lines. The lamp was imaged to test the system's ability to measure a real world spectrum instead of from a laboratory-grade instrument.

The curve started to rise from the floor about 10 nm prior, but it never returned to the floor. Instead, it slowly increased until the light from the 546 nm emission took over. Figure 4.38 shows a frame from the raw video taken of the scenario. The 546 nm light was in the center of the frame. The spike at 611 nm was lower and to the left of that. In the shorter wavelengths, higher and to the right, there was an extremely faint line of
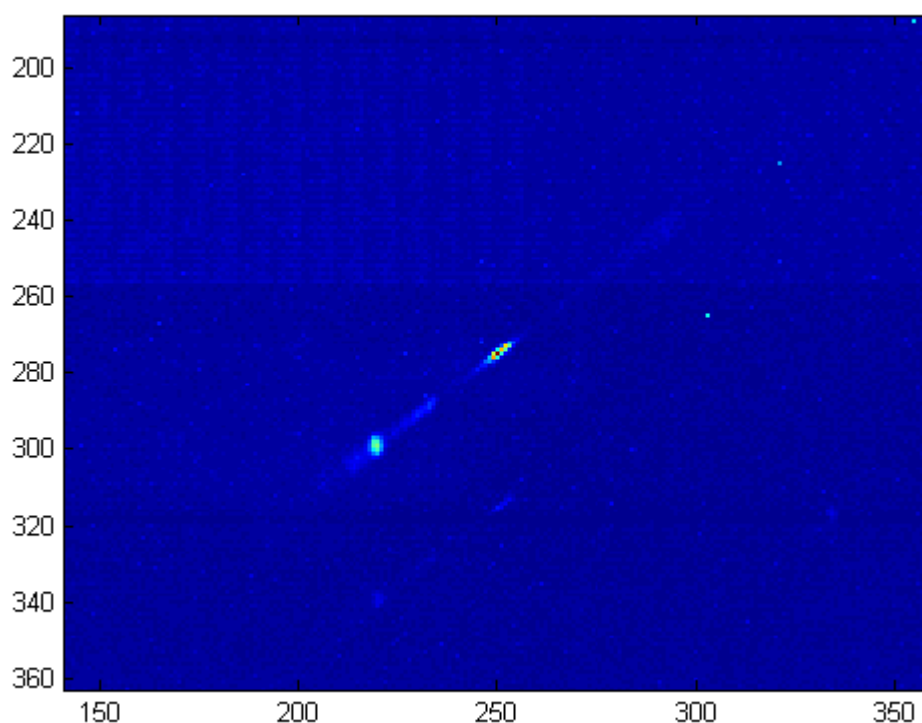
Figure 4.38: A frame from the raw data used to produce the spectrum in Figure 4.37. The 546 nm light was in the center and the 611 nm light was below and to the left. The faint band of light above and to the right indicated that the fluorescent lamp did possess broadband characteristics, likely from the excitation of phosphors coating the bulb.

light. It existed in each sequential frame and was easier to notice while watching the video, but it was definitely there. There was also an area brighter than the rest of the light that likely was from that odd hump near 486 nm. It was so dim, however, that it might not have provided much useful information. The existence of that band of dim light and others at longer wavelengths confirmed that the spectrum did indeed possess broadband characteristics. The light was likely produced from the excitation of phosphors in the coating of the fluorescent light bulb [10].

4.3.6   *Spectral Complexity Summary.*

A summary of peak wavelength differences between CTEx and truth/theoretical lines for the spectral complexity section are in Table 4.6.   The average line widths and

Table 4.6: Summary of wavelength error and line widths for the spectral complexity section. The true line widths that were atomic emissions were from Figure 3.6. The X-Corr was the middle value of the 1-D normalized cross-correlation vector between the truth and reconstructed spectra.

Source	Mean λ error (nm)	Mean line width (nm)	True line width	X-Corr
Atomic Lines	0.6	3.0	2.8	0.61
Pen Lamp	1.5 ± 1.0	8.9 ± 3.2	8.4 ± 2.4	0.44
12nm BP	-1.2	12.9	13.3	0.98
50nm BP	0.3	8.2	37.8	0.92
550nm SP	0.3	43.8	57.0	0.99
665nm LP	0.5	65.7	68.3	0.98
White Light	71.2	150.5	184.4	0.78
Fluorescent	0.6 ± 2.4	15.9 ± 5.8	7.2 ± 1.5	0.78

truth/theoretical measurements for each scenario are also reported. The true line widths for atomic lines, the pen lamp, and the fluorescent light were taken from Figure 3.6. The column of X-Corr was the middle value of the 1-D normalized cross-correlation vector between the truth and reconstructed spectra.

4.4   Image Quality vs Temporal Complexity

The 3rd leg investigated how time affected image quality. The first section discusses the prism speed. It addresses the questions of how much the prism can spin in one frame of

data before the image is severely degraded. The next is about how much the shape of the object being reconstructed can change before it can no longer be reconstructed. Finally, the number of frames required for an adequate reconstruction is characterized.

4.4.1 Motion Blur.

When the prism spun, the individual wavelength images rotated in a circle about a point where the theoretical undeviated wavelength would be. When an image was recorded, there was a finite amount of time associated with each frame called the exposure time. In a digital camera, the exposure time is analogous to the amount of time the shutter is open in a film camera. Since the image moved in the exposure time, there was some amount of blur in the image. The less the image moved, the less blur there was.

If a reconstructed image is made up of individual blurry images, it will not form a pristine image. Motion blur will have the same result as an image out of focus. With a perfect prism, 547 nm would have no motion blur because its radius of rotation is 0. A wavelength further away from the undispersed will have more blur. To test motion blur's effect, a Mercury pen lamp illuminated the Air Force bar target. A 500 nm short pass filter was placed in front of the prism so only the 435 nm line made it to the camera, and that wavelength was in focus. Several videos were recorded, each with the prism rotating at a different rate. Figure 4.39 shows raw images of the bar chart at 0° per frame and 12° per frame. Figure 4.40 shows the image degradation as the prism spun faster, resulting in greater motion blur.

Each image was reconstructed using unfiltered backprojection, and the spectra were attained with the edge technique. The tallest peaks for each rate were the wavelengths of best reconstruction. The smaller peaks can be attributed to the periodic nature of the bar chart. The figure shows the peak intensity decrease as motion blur increased. at 6.2° per frame, the maximum instensity was less than half of the max at 0° per frame. By the time the prism spun 12° per frame, the peak intensity fell into the noise. The maximum
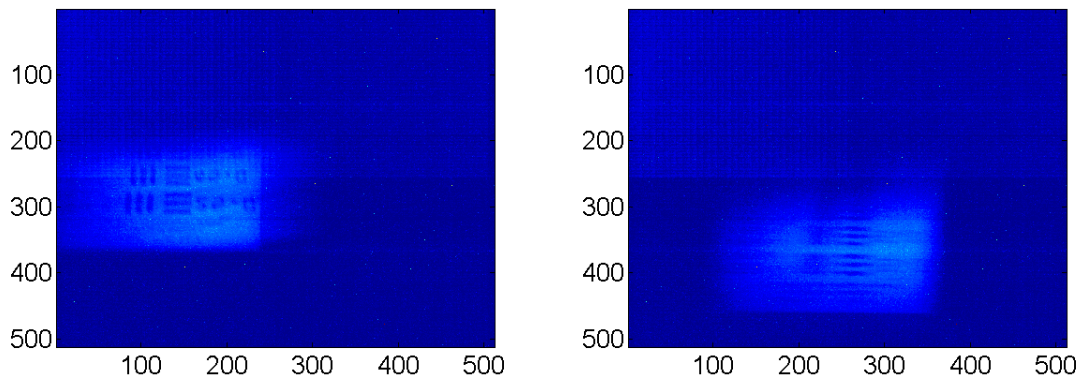
Figure 4.39: Raw frames of the prism spinning at 0 and 12° per frame. Notice how degraded the faster spinning image was compared to the one not spinning at all.

reconstructed wavelengths also appear to have been shifted towards the blue end of the spectrum as motion blur increased, though it is unclear why.

Figure 2.3 shows that the blue wavelengths are deviated more than the red, so they should be affected more by motion blur. To measure the blur in the red region, a 665 nm long pass filter was placed in front of the DVP while imaging the bar chart illuminated by a Neon pen lamp. Since Neon has so many emission lines greater than 600 nm, 2 bright lines were still visible. The image was reconstructed over a 20 nm range so only the brighter line at 703 nm produced a peak. Figure 4.41 shows the same for the red as Figure 4.40 does for the blue. As the prism spun at a higher rate, motion blur affected the reconstructed image quality. Since blue is deviated through this prism more than red, it blurred more. At 6.2° per frame, the peak was about 66% of the stationary case. At 12° per frame, the 703 nm peak wasn't in the noise, but it was still much lower than the peak for a stationary prism. This figure indicates that motion blur tended to "redden" a reconstruction in the red.
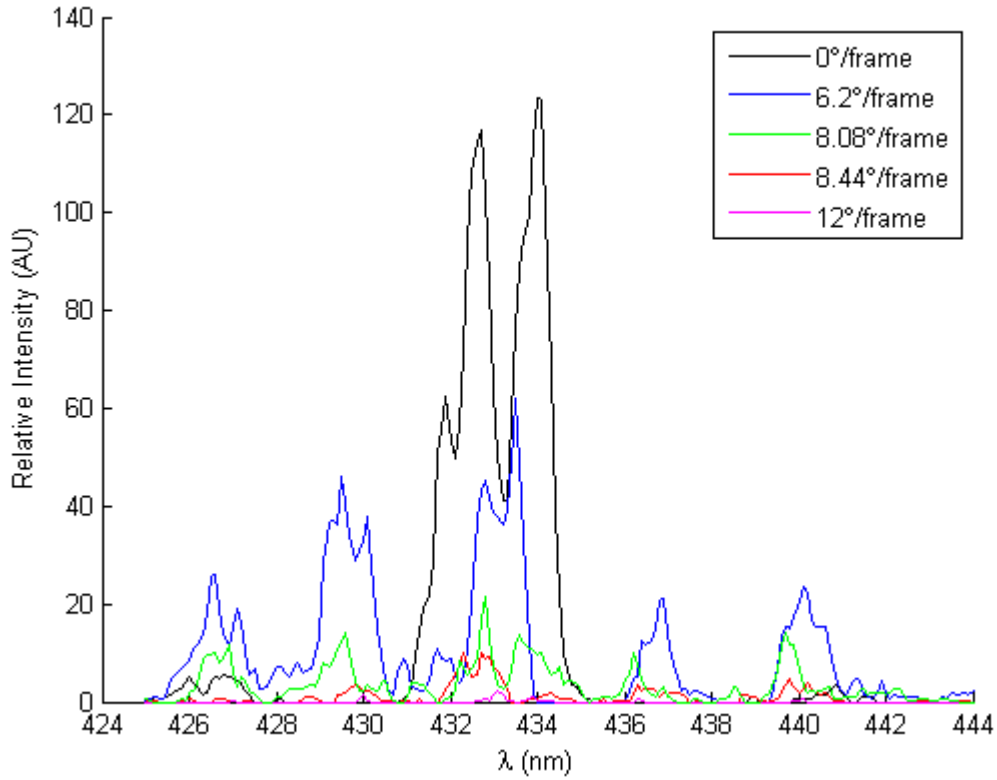
Figure 4.40: Reconstructed spectrum of the 435 nm line of a Mercury pen lamp while illuminating the Air Force Bar Chart with varying prism rotation rates. As the prism rotated more quickly, motion blur caused a degradation in the image reconstruction quality, which manifested itself with lower peak intensities in the spectrum. The secondary peaks for each rate were consequences of reconstructing the bar chart. The figure indicates motion blur shifted these wavelengths more to the blue end of the spectrum.

4.4.2 Changing Scene.

A likely real-world application for chromotomography would be to image an event that changes either spectrally, spatially, or both. To simulate a spatially changing event in the laboratory, a 25 slide show was developed in Microsoft PowerPoint. Each slide was presented on a laptop located 2 m from L_1. The prism spun at a rate such that it

103
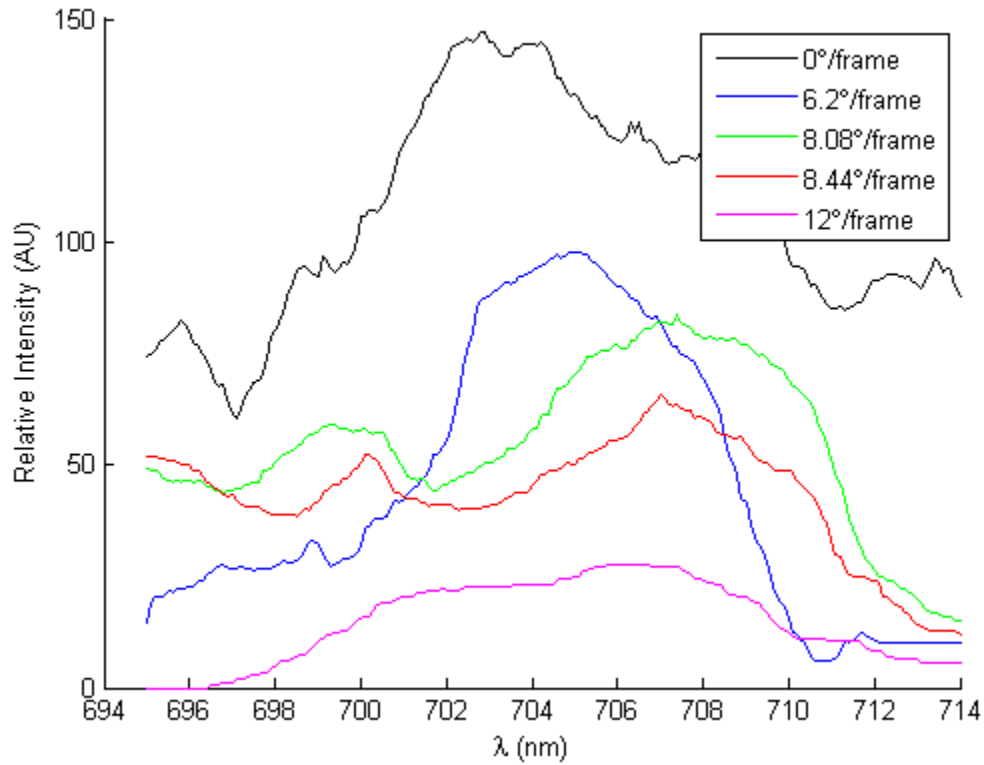
Figure 4.41: Reconstructed spectrum of the 703 nm line of a Neon pen lamp while illuminating the Air Force Bar Chart with varying prism rotation rates. As the prism rotated more quickly, motion blur caused a degradation in the image reconstruction quality, which manifested itself with lower peak intensities in the spectrum. The figure indicates motion blur shifted these wavelengths to the red end of the spectrum.

would complete 1 full revolution per slide as they automatically transitioned to the next. Enough energy was captured to make use of as much of the camera's 8-bit dynamic range as possible. The first slide consisted of a black background with a white ellipse whose major axis was in the horizontal direction. The second slide had the same background and horizontal axis, but the vertical axis was slightly longer. The trend continued as the shape turned into a circle and into another ellipse, all the way to slide 25. The horizontal axis

never changed. Next to each of the ovals was a white rectangle whose dimensions and positions never changed. It was used as a known spatial reference to aid in determining the correct prism offset angle when reconstructing the hypercubes. The 1st and 25th frames of the slide show are shown in Figure 4.42.
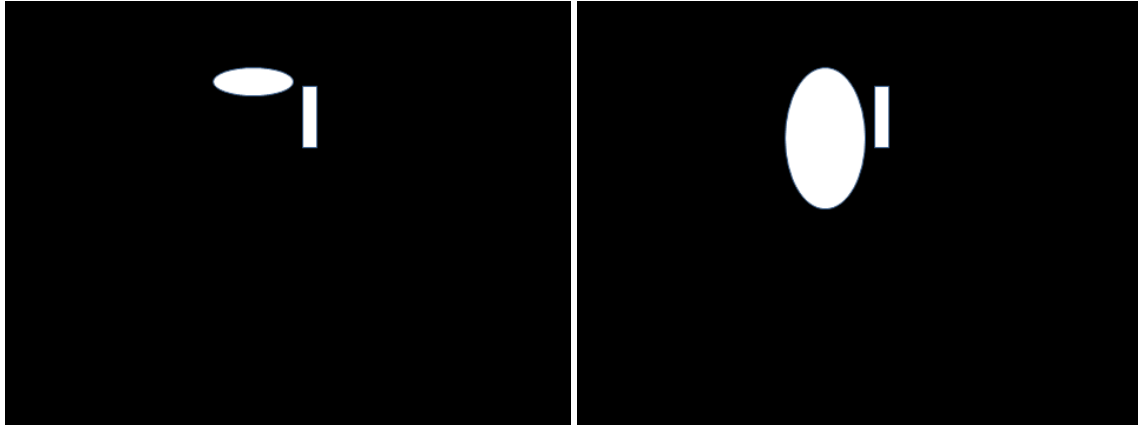
Figure 4.42: The first and last frames of the PowerPoint video used to create a changing event. Each slide was on the screen for 2 seconds before automatically flipping to the next. In each subsequent frame, the vertical axis of the oval elongated slightly. The white rectangle was used to determine the prism offset angle during reconstruction.

A black background with a white shape was chosen to provide maximum contrast. It was thought that by using different filter combinations on the white object, several spectral scenarios could be used to further understand the system's ability to measure spectra. The reconstructed images at 550 nm of the scene with one shape and the scene with all shapes is in Figure 4.43. The spectrum of the white portion of the monitor's composite of RGB bands is shown in Figure 4.44, as measured by the Ocean Optics spectrometer. The regions used to measure the spectra included the entire shape of each oval, and are marked by the black rectangles. Since the screen was relatively dim, the integration time on the
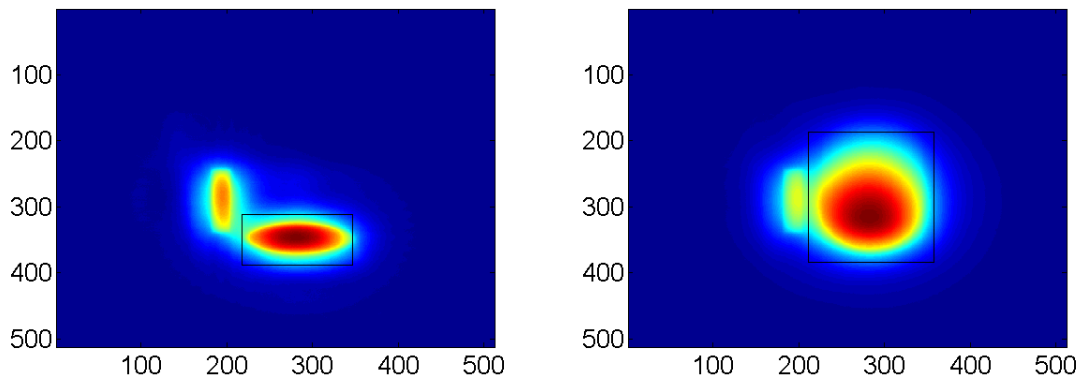
Figure 4.43: (L) The reconstructed image of the scene with one shape at 550 nm. (R) The reconstructed image of the scene with 25 shapes at 550 nm. The picture with one shape had sharper edges, so it was considered a better reconstruction.

spectrometer was long: 1,000 ms vice the 300 ms normally used with in this project. That introduced a lot of noise in the system and increased the noise floor. The spectral features were barely noticeable. To tease spectral peaks from noise, 10 measurements were taken with the spectrometer and averaged together. The noise floor was rescaled to 0 by subtracting every data point by the minimum in the averaged set. There was a peak in the blue and a broad range in the green and yellow. There was a smaller peak near 640 nm that represented the red light from the screen. There was only one small peak in the extreme long wavelengths. The reconstructed spectra that follow were created using the edge technique. The edges were the sharpest features, so the edge technique made the most sense to use. The gradient wasn't used because no matter the threshold used, the algorithm recognized every pixel as worthy of counting. When plotting the image of the gradient, there were no distinguishable images. It is impossible to create a single pristine image for a scene that is changing in time. The cross-correlation and MAE techniques weren't used because of that. The mean intensity was not a good technique for spatially complex

106
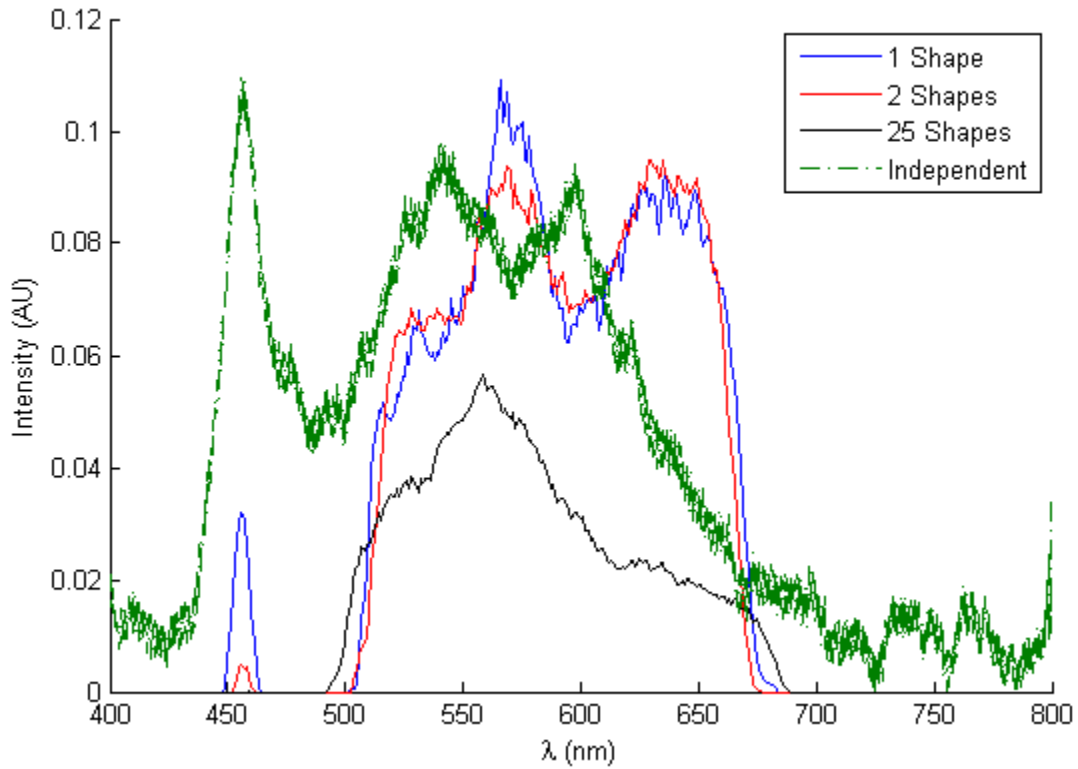
Figure 4.44: The Ocean Optics spectrum of a white portion of a laptop monitor. The CTEx spectra were from the unfiltered backprojection of a changing scene, built with the edge technique. An ellipse with one axis that grew in each subsequent frame was imaged. The reconstruction was done with only the first shape before it changed, only the first 2 shapes, and for all 25. As the scene changed more for each reconstruction, the image quality was degraded.

scenes because the artifacts inside the region of reconstruction always contributed to a false positive.

To assess the ability to image a changing scene, the spectrum of the white area was produced for three different recording durations. The first was a reconstruction of only the first shape, which was 40 frames. The second contained 80 frames and the first two shapes.

107

The expectations were for the image quality to be reduced. The two similar yet different shapes were all superimposed to form one image after the unfiltered backprojection. The portion of the shapes that overlapped were then twice the intensity of that same region in the image with only one shape. To provide an apples-to-apples comparison between reconstructed spectra, those pixels were divided by 2. The third situation involved all 25 slides, which was more than 1,000 frames. The shapes took up a much larger area than the previous two, like in the right side of Figure 4.42. The region used to calculate the edges included the entire shape. The section that included the first ovals was much brighter than the last that was only occupied by the 25th shape. The pixels were divided by 25 to normalize the original section with the reconstruction with 1 shape. The comparison of the plots is also shown in Figure 4.44.

Each reconstruction used the same threshold when calculating the edges. The system was focused on the broad-band area between 550 and 600 nm. The peak of the curve with 1 shape was at 566 nm. The 2 shape curve was shifted to the red slightly and the 25 shape curve to the blue. There was a peak at 550 nm in the theoretical spectrum, but it was not the global maximum. Confirming expectations, the single shape spectrum had the highest peak intensity, followed by the 2 shape, and finally the image with all shapes. The red and blue curves took on very similar shapes between 500 and 700 nm because the ovals were nearly identical. They both had another area of a local maximum in the red range of 650 nm, but the 2-shape peak was higher than the 1-shape. The edge detection software was able to pick up more edges there than expected. For one data set, this was not surprising since the shapes were so similar. Over several measurements, the peak likely would drop to below the single shape's max.

4.4.3   *Image Quality at Less than 1 Full Rotation.*

During a real-world scenario, an event might happen such that it finished before the prism had a chance to complete even 1 full revolution. This section simulated that with

a spatially static scene. The Mercury pen lamp was filtered so only the 546 nm emission illuminated the bar chart. There were no artifacts, and the image quality was evaluated by visual inspection and cross-correlation. The Phantom camera recorded a single video at 20 frames per second with a 49,900 μs integration time. The reconstruction software was adjusted so it only processed the frames needed to carry out the experiment; approximately 60 frames made up 1 revolution. Those frames encompassed 1/4 of a prism rotation, 1/2, 3/4, and 1 full rotation, all of the same scene with 60 frames per revolution. The rest of the reconstruction process continued as normal. Every frame that was recorded was included in each range for its reconstruction; a discussion of the sparsity of available frames is in the next section.

The prism rotated counter-clockwise in the image plane starting at 12 o'clock. A side-by-side comparison of the unfiltered backprojected images with only 3/4 and a full revolution of the prism is in the top 2 figures in Figure 4.45. The picture on the left is with the full rotation and the right with 3/4 of a rotation. The bright spots on the left were reflections from the lamp off of the glossy surface of the target. The images are similar with very minor differences. When it came to image quality, the 3/4 rotation image was surprisingly better. There was a little bit more detail near the edges of the field stop, especially in the set of bars in the top center. It was brighter compared to the surrounding areas than the full rotation. The differences were subtle and extremely difficult to see, but they were worth reporting. Overall, there was very little that varied between the two images as they were nearly identical. In this case, the extra frames needed to complete the rotation did not contribute to a markedly improved image.

The bottom 2 figures in Figure 4.45 shows a side-by-side comparison of the images with a half of a rotation and a quarter rotation. On the left is the former and the right is the latter. Like in the previous example, the images in this set were very similar, but had some differences in image quality when examined closely. The space between the largest
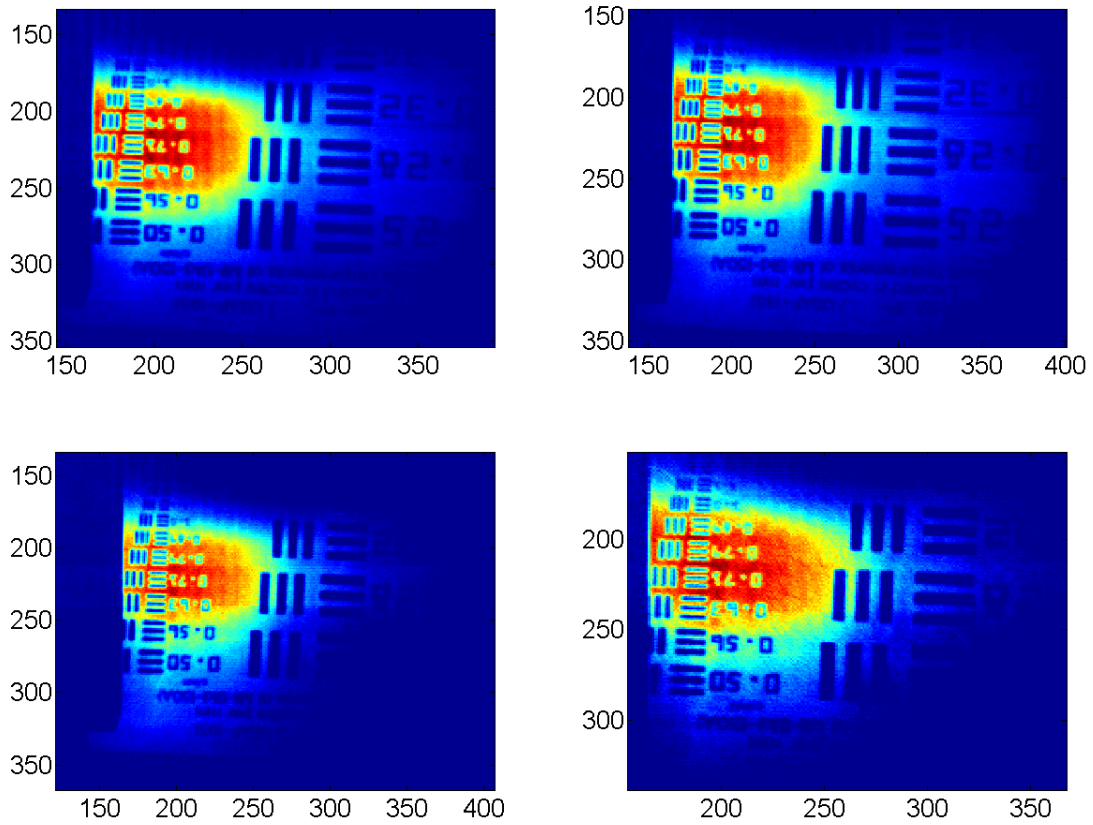
Figure 4.45: (Top Left) An unfiltered backprojection of the Mercury lamp illuminating the bar chart when the prism completed 1 full revolution. (Top Right) The reconstruction when the prism completed only 3/4 of a revolution. There was very little difference between these 2 images. (Bottom Left) The reconstruction when the prism completed 1/2 of a revolution. (Bottom Right) The reconstruction when the prism completed only 1/4 of a revolution. The biggest difference between successive images was between the 1/2 and 3/4 revolution graphs.

set of bars (slightly low of center) was filled in more with more of a rotation. The target was also imaged to its bottom edge in the lower left corner and further to the right of that. Those areas remained largely dark in the image with only a quarter of a rotation. Despite

110

these differences, there is not as big of a difference between these two as there was between the 1/2 and 3/4 rotations. In the poorly lit regions on the right sides, the image with 3/4 of a rotation were much more developed. The majority of the spatial frequency labels were readable. The bright red region on the left was also filled in more. The most intense pixels covered a larger area within the bright spot. The spot also extended further up and down in the image with more rotation. While there was not a lot of difference between 1/4 and a half rotation and likewise for the 3/4 and full rotations, there was between 1/2 and 3/4. The results of this experiment suggested at least 3/4 of a prism rotation is required to ensure a complete reconstruction if there were 60 frames per rotation. Figure 4.46 shows the cross correlation between each image in Figure 4.45 and a pristine image. The image with the

full prism rotation was nearly perfectly correlated. It even showed a spike at the 578 nm doublet. The largest gap in peaks was between the 3/4 and 1/2 prism rotation lines.

Figure 4.47 shows the same scenario but with the white light source filtered by the 12 nm bandpass centered at 641 nm. The system was focused to the best overall setting.

Because the image was of a spatially complex object (bigger than a point source) over a continuous band, it never came into sharp focus. Again, each figure was cross-correlated with a pristine image of the bar chart to evaluate how the fraction of a prism revolution affected image quality. It is shown in Figure 4.48. The results were surprising since the

correlation improved, however slightly, with decreasing fraction of revolution. Unlike in the Mercury example, none of the structures on the fringes of the images were lost. The continuous band caused all of the out of focus light to overlap the in focus light in close proximity. Since the normalized cross correlations were essentially equal, the line widths indicate which cases reconstructed the best. The full rotation had the most narrow line and the quarter rotation was the widest. Each of the images achieved maximum correlation at or near the band's center of 641 nm.
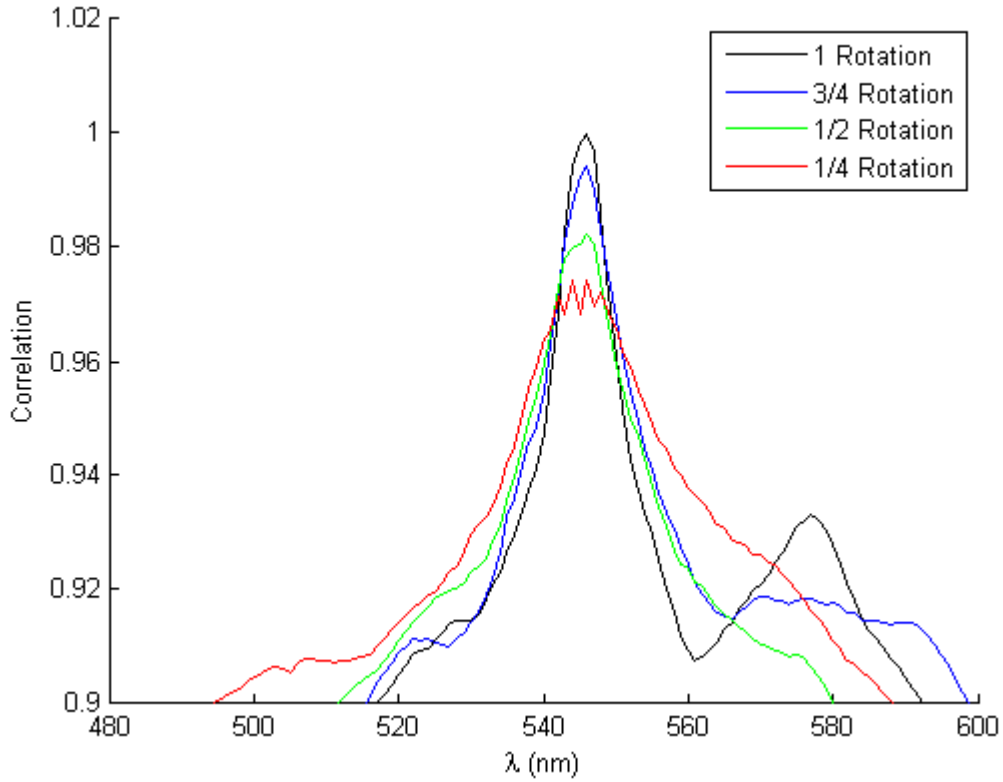
Figure 4.46: The cross correlation of the images with a pristine image. The full rotation was nearly a perfect match. It even showed a reconstruction at the 578 nm doublet. The biggest difference was between the 3/4 and 1/2 rotations.

4.4.4   Dependence on the Number of Frames In a Rotation.

The final section on time dependence involves the quality of the image as a function of the number of frames in a reconstruction. The same video was used in this experiment as in the previous. The range of frames was so that a complete revolution was unfiltered and backprojected. The reconstruction was done for every frame in the range, every other, every 3rd, and every 5th frame. Figure 4.49 is a side-by-side comparison of two of those scenarios.   The left side is of the reconstruction done with every frame - about 60. It is the same image as the left side of Figure 4.45. The right side is the reconstruction using

112
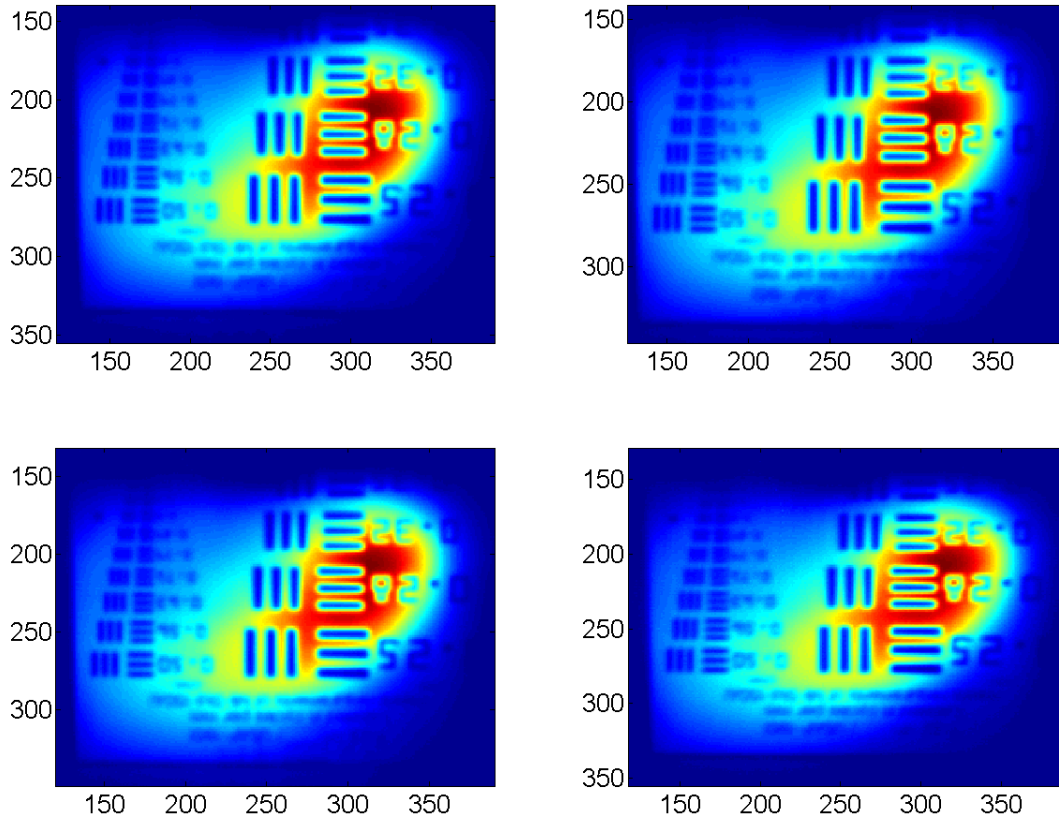
Figure 4.47: (Top Left) An unfiltered backprojection of the white light source with a 12 nm bandpass filter illuminating the bar chart when the prism completed 1 full revolution. (Top Right) The reconstruction when the prism completed only 3/4 of a revolution. There was very little difference between these 2 images. (Bottom Left) The reconstruction when the prism completed 1/2 of a revolution. (Bottom Right) The reconstruction when the prism completed only 1/4 of a revolution. There was very little difference between each image.

every 5th, or 12 total frames. These two were picked to show the difference between the best and worst cases investigated, but the results were properly scaled for the others. Both were zoomed in to show more detail in the images. Unlike the situations with less than a full revolution, the entire scene was visible in each. The images have the same intensity

113
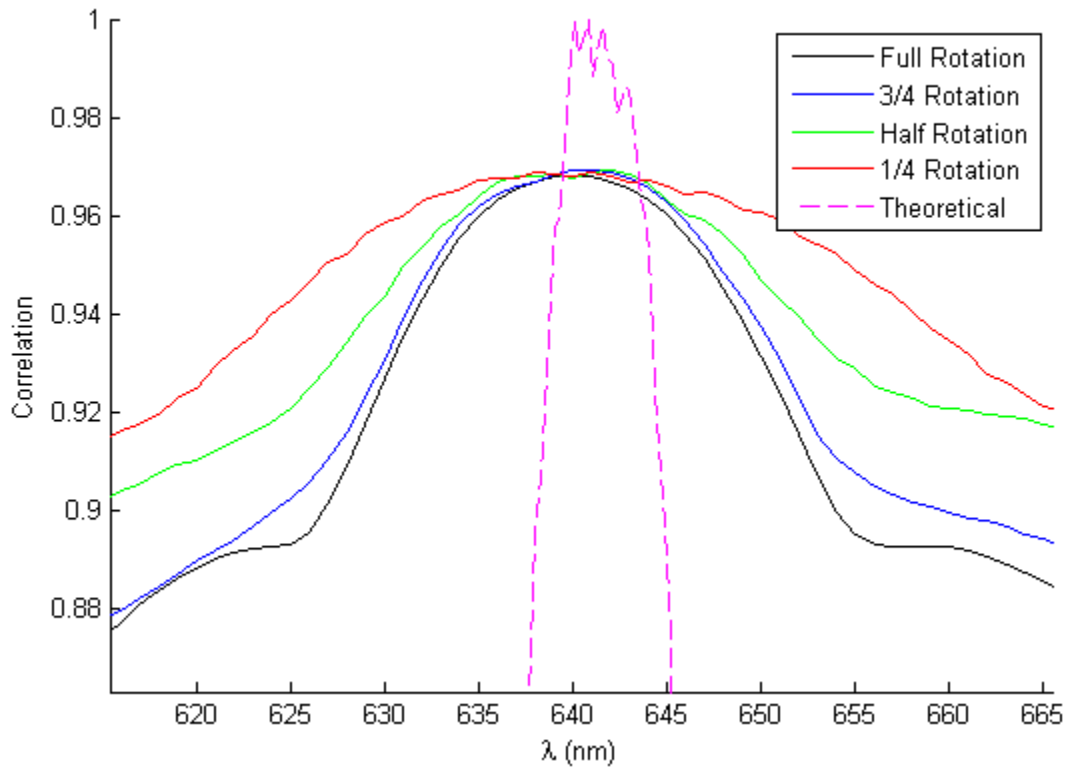
Figure 4.48: The cross correlation of the images with a pristine image. In this case, the image with only 1/4 of a rotation correlated best, though they were all very close.

pattern. The scales show the left image had a higher intensity in each pixel because it used more frames. It is also an image that is more clear. The right figure was more grainy. It did not have as many frames to average out the noise that might have been present. Since none of the features were seriously degraded compared to the full frame example, using 12 frames in a full revolution might be sufficient to adequately reconstruct a scene, depending on the spatial resolution required.

4.4.5 Temporal Complexity Summary.

Table 4.7 summarizes the results of the temporal complexity summary.   With this particular prism, the combination of the frame rate and rotation rate should be kept to

114
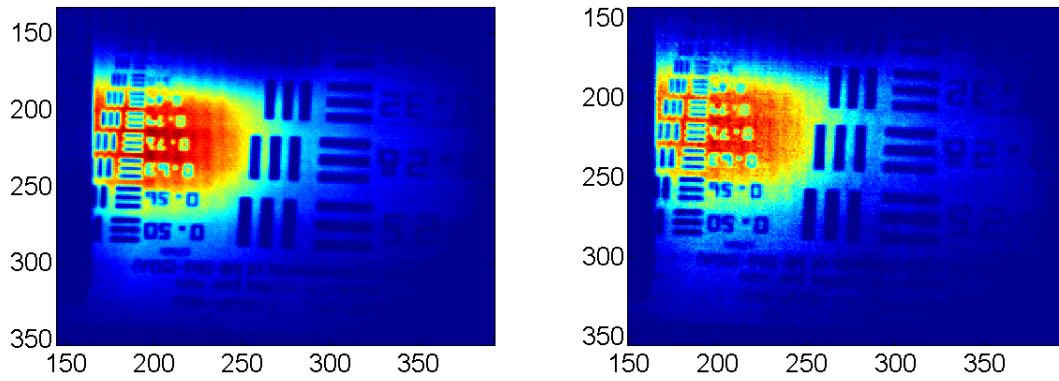
Figure 4.49: (L) An unfiltered backprojection of the bar chart with 1 prism revolution using 60 frames. (R) The same situation using only 12 frames. The image with sparse sampling was more grainy, but none of the features were seriously degraded. Using only 12 frames for a reconstruction might be adequate, depending on the spatial resolution required.

Table 4.7: Summary table of the temporal complexity section.

Scenario	Recommendation	Comments
Motion Blur	$\leq 6.2°$/frame	50% Intensity Reduction
Changing Scene	As little change as possible	"Change" difficult to define
< Full Rotation	$\geq 3/4$	w/ 60 frames per rotation
# of Frames	≥ 12	Slight reduction in quality

less than 6°/frame. At that point, the motion blur can reduce the overall intensities in a scene by more than 50%. Also, the spatial characteristics in a scene should change as little as possible. While defining what a change precisely means, it was found that scenes reconstructed best when only a very slight spatial change occurred. The more frames taken

115

of the scene, the better. Additionally, if a sufficient number of frames was obtained (60 in this case), using only 3/4 of those frames to reconstruct the scene offered very little degradation than if all of the frames were used. There was a big drop in quality between using only 1/2 the frames and 3/4 of them, though. Finally, as few as 12 projections in a full rotation was sufficient to reconstruct a quality image. Though that picture was a little more grainy than a rotation with 60 frames, features were not lost.

4.5 Field Demonstration

To bring everything in this project together, an experiment was devised that would include difficult parts of every scenario wrapped into a single event. The event was to simulate an actual scene chromotomography might be expected to image. It had complex spectral and spatial features. Its shape and intensity also changed in a short period of time. It was created by pouring some non-dairy creamer into a funnel and shooting compressed air though it to make it spread out in the air. A small propane tank was opened, the gas lit, and held up to the cloud of creamer. It ignited the cloud and created a fireball. The events lasted approximately 1 second. The fireballs were ~ 1 meter in diameter. CTEx was set up 25 m from the fireball. All of the data were taken at twilight or in the dark of night to reduce solar reflections. There was also a tarp in the background to create a uniform scene. A Mercury pen lamp was in the FOV to give a known spatial and spectral reference. CTEx was focused on the 546 nm emission line. The fireballs' spectra were also independently measured by the Ocean Optics spectrometer. Collecting the independent data was more art than science. It was a matter of timing the collection right and pointing it at the center of the fireball. For many runs, reliable spectra were not captured.

4.5.1 Unfiltered Backprojection.

One of the main ingredients in the creamer included Sodium, so the emission doublet at 589 nm was expected to be a prominent feature [23]. 2 reconstructed spectra and the independent measurement are included in Figure 4.50. This measurement was of only
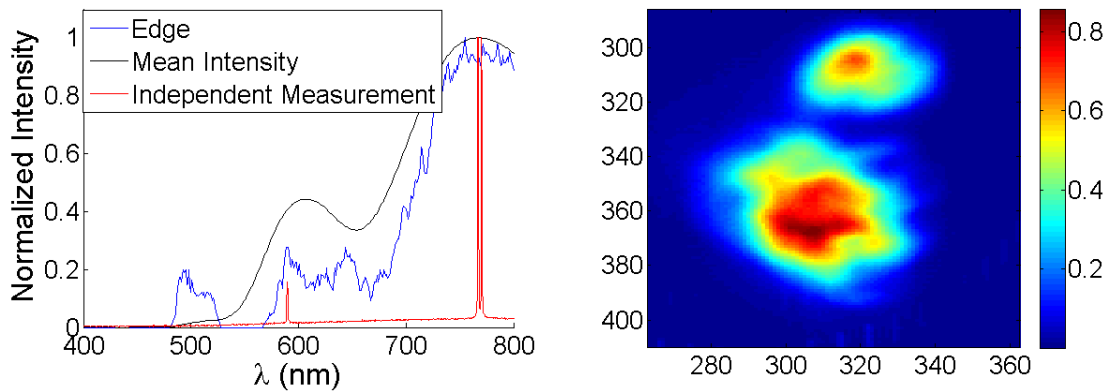
116

Figure 4.50: (L) The spectrum of an unfiltered backprojection of a fireball created with non-dairy coffee creamer and an independent measurement. (R) The reconstructed image at 770 nm of the fireball. The smaller fireball was used to build the spectrum and is at the top of the figure.

the coffee creamer with no other materials intentionally added to modify the spectrum. The red line was measured by the Ocean Optics spectrometer. An emission was detected from the Sodium doublet, but it was very dim compared to a Potassium emission at 767 nm. The spectrometer was also not able to resolve the two lines as there was only one peak in that region. The brightest emission was a doublet near 770 nm that was from Potassium [23]. The fireball was red in color, so this was a likely explanation as to why. The independent spectrum also indicated some gray- or black-body behavior. If the temperature of the fireball were 800K (525° C), the tail of the black-body curve would just be in the visible spectrum, giving it a red hue. The black or gray bodies were likely from soot that had already burned and remained at a high enough temperature to still emit. There will not be a discussion of blackbody theory here. For an in-depth tutorial, read the *Infrared and Electro-Optical Systems Handbook* [2].

The blue and black curves represent the unfiltered backprojection spectra built with the edge and mean intensity techniques, respectively. Creating these curves relied on lessons

117

learned in every laboratory scenario created for this project. Using the proper prism spin rate, frame rate, and exposure took several failed trials. After some calculation and drawing on experience, most videos used a 180 μs exposure time, recorded at 800 fps, and the prism spun at a rate of 13 Hz. Selecting the proper frames from the video and the area of reconstruction proved to be difficult. It required finding a section where the fireball's shape did not change significantly over the course of a revolution of the prism. Those frames also had to have spatial features that overlapped as little as possible. The selection included a little more than 100 frames and had 2 fireballs close together. The 2 fireballs were probably from 2 clumps of the powder that each ignited separately. The pen lamp was also visible throughout the scene and spatially separated from the fireballs.

The region selected to build the spectra was around the smaller of the two fireballs. Figure 4.51 is an off-wavelengths reconstruction at 604 nm. The small fireball is the halo centered on the black rectangle in Figure 4.51, which was the region of reconstruction.

The larger fireball begins in the rectangle, and arcs in a halo to the bottom of the figure. The spectra in Figure 4.50 show some level of agreement with the truth spectrum. The bumps centered around 500 nm were when the artifacts from the pen lamp crossed through the region of reconstruction. They showed spectral information in the vicinity of the Sodium doublet at 589 nm. While some of the intensity shown was that light, it was also from artifacts from the bigger fireball as it passed through the region.

That is also why the peak was shifted by 15 nm. The width of that curve was a combination of the odd shapes of the artifacts, the dispersion curve, and the defocus of the light since the 546 nm line was in focus. Finally, the brightest reconstructed peak was from the Potassium doublet near 770 nm. There were no artifacts in the area of reconstruction at that point, so all of the data was from that emission. The peak wavelengths of the spectrum based on mean intensity and truth data were almost identical. The edge curve was spiky
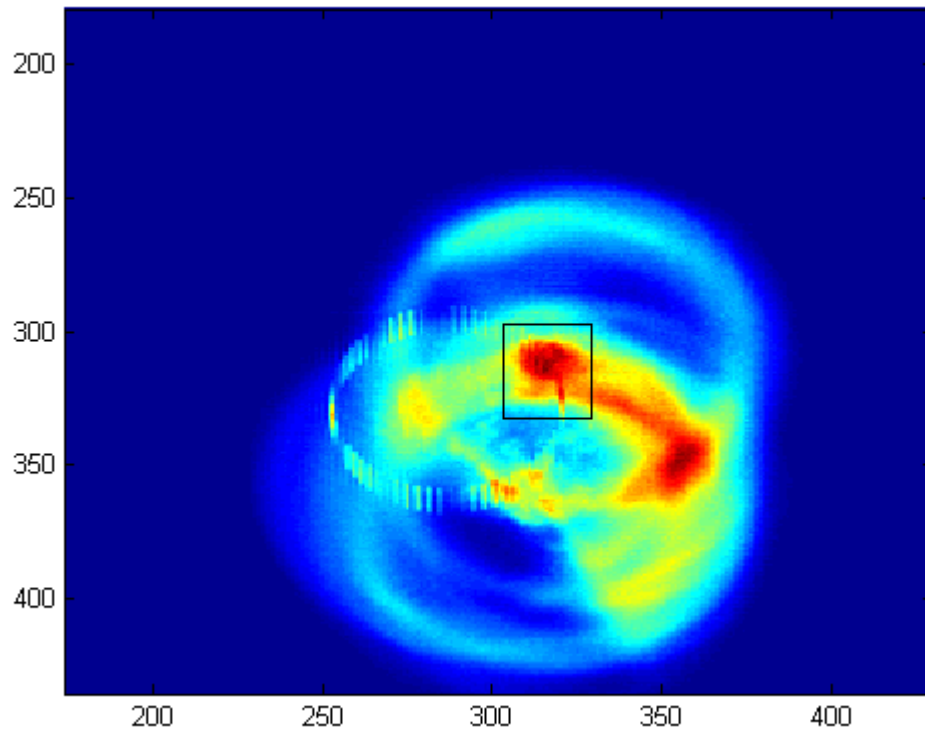
Figure 4.51: An off-wavelength reconstruction of artifacts passing through the region of reconstruction (black rectangle). The larger fireball, which wasn't measured, begins in the middle of the rectangle and sweeps in a halo to the bottom of the figure. The smaller fireball, which was measured, is the halo centered around the black rectangle.

but its center was at approximately the same as the others. It was impossible to tell if it showed black-body features because of the widths of the individual emissions.

It is difficult to assess how well CTEx worked as an imager in this scenario. The scene changed extremely rapidly, so there was no pristine image recorded. The shape of the fireball was not repeatable. Based on first hand observations, 2 fireballs were clearly seen in real time. To a qualitative degree, Figure 4.50 is an accurate reconstruction of the scene.

In other cases, like with the bar chart, the user knows what it is supposed to look like. A fireball might be expected to be roughly circular in shape, but not much else is known.

4.5.2 Filtered Backprojection.

Figure 4.52 has the filtered backprojection along with the independent comparison of the exact same scene. Much of the same can be said about this plot as of the unfiltered
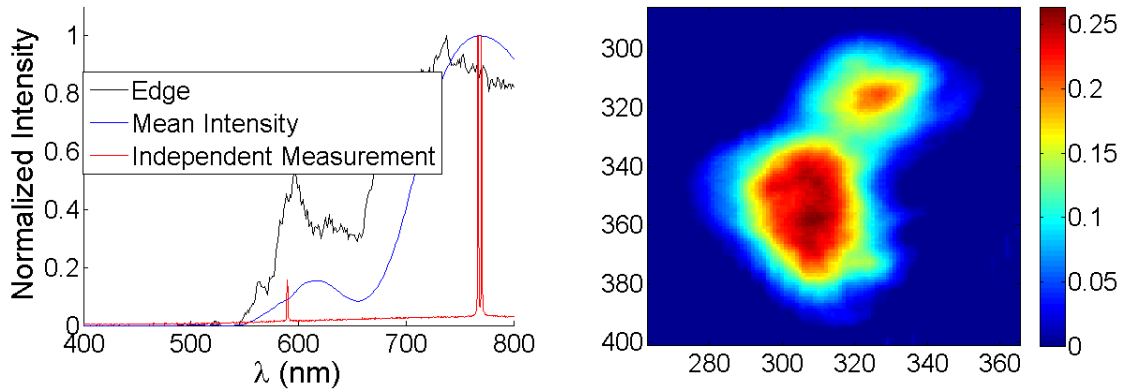

Figure 4.52: (L) The spectrum of a filtered backprojection of a fireball created with non-dairy coffee creamer and an independent measurement. (R) The reconstructed image at 770 nm of the fireball. The smaller fireball was used to build the spectrum and is at the top of the figure.

backprojection. The normalization of the intensities hid the overall reduction in pixel values for the filtered case. The reduction was expected since the images were divided by a value greater than 1 when applying the filter ($\mu = 5$ in Equation (2.17)). The mean intensity gave a peak at the 770 nm Potassium doublet. It also gave spectral information at the 589 nm Sodium doublet that was red shifted because of the artifacts from the bigger fireball. In this case, it was roughly the same relative peak intensity as the independent curve instead of much greater as before. The intensities from the big fireball were dampened by the filter. There were also some improvements and drawbacks. Even though the pen lamp was

120

still visible throughout most of the frames in the cube, the magnitude of its intensity was reduced by the filter too. It hardly showed up as a blip in the 500 nm range. The maximum of the edge technique's curve at wavelengths greater than 700 nm was spiky again, but shifted toward the blue. Some artifacts from the other fireball were present in the scene and contributed edge counts. When a slightly higher edge threshold was picked, the entire curve disappeared. Just like in the unfiltered reconstruction, the line widths were large because of the dispersion curve and defocus. There was not a marked advantage to using the filtered vice unfiltered backprojection for this scenario.

V. Conclusion

This chapter provides a summary of the research conducted in this thesis. Conclusions are made on the ability of CTEx to reconstruct hyperspectral images based on spatial, spectral, and temporal complexity. The value of using filtered backprojection versus unfiltered backprojection is assessed. The hypercube is discussed, as well as the cone of missing information. Finally, future recommendations are made.

5.1 Experiments

The main takeaway from the experiments is though CTEx can reconstruct both images and spectra, each affects the other. After projection through the prism, the spectral and spatial information are multiplexed into a single image on the focal plane array. Greater spectral and/or spatial complexity increase the amount of overlap, which diminishes the quality of reconstruction. A scene with complex spatial features and a simple spectrum, like the image of a brain illuminated by a Mercury lamp, did not reconstruct as well as the Mercury lamp behind a pinhole. Likewise, the complex spectrum of the fluorescent lamp's emission behind a pinhole did not create as accurate of a spectrum as the Mercury lamp behind a pinhole. The fireball, which had distinct emission lines and blackbody features, as well as amorphous spatial structure, was very difficult to reconstruct.

5.1.1 Spatial Complexity.

CTEx rebuilt scenes of all types of spatial complexity to different levels of success. From a pinhole to an amorphous object, it could recreate a scene that looked very much like the original, provided it was at a wavelength that was bright compared to the other emissions. The amorphous object gave the most difficulty, especially in the areas of larger spatial frequency. It was seen that wavelengths that were in focus reconstructed much better than those out of focus. Artifacts always influenced image quality when they were

122

present. Using the Air Force bar chart created spectral peaks that flanked the main peak in reconstructions, especially in the unfiltered backprojections. As the bars collapsed to the center, their artifacts added up to create the false peaks.

5.1.2 *Spectral Complexity.*

CTEx was able to reconstruct the data at all levels of spectral complexity. The best reconstructions were at bright emissions that were spectrally separated from other emissions. It also had the most success when reconstructing a wavelength that was in focus. Determining what "in focus" meant for this experiment was difficult. The steep dispersion curve in the short wavelengths caused even narrow pen lamp emissions to spread along the dispersion axis. Chromatic aberration also appeared to be present. Even though commercial compound lenses are engineered to minimize the effect, it still showed as blurry circular spots for atomic emission lines. By adjusting the focus, it was possible to get the 435 nm Mercury emission to form a tight spot. However, that may have just been repackaging the bundle of rays that should have been spread out onto a smaller area. Both chromatic aberration and dispersion likely contributed to image degradation. Many dim or badly out of focus emissions failed to register any intensity when building spectra.

The dispersion from the prism also affected the reconstruction in other ways. Since the blue wavelengths were deviated at a higher rate than the red wavelengths, they would always build a narrower line for the same spatial object. The FWHMs were sometimes only half the size in the 400 nm range as they were in the 700+ range, as was expected. That also affected the spectral resolution. The resolution was clearly better in the shorter wavelengths of a Neon emission than it was in the longer. CTEx resolved spectral separations of 10 nm, but could not distinguish between emission lines in a doublet. The smallest FWHM measured was 4.6 nm.

The reconstructed spectra of filtered and unfiltered white light and a fluorescent light bulb often closely matched the theoretical spectrum, but the importance of focus became

readily apparent again. CTEx built patterns that correlated to the spectral response of the camera. It was able to recognize the atomic emissions of the fluorescent light bulb as well as the broad-band nature of the light. During the white light portion, it was discovered that choosing the correct area to analyze was crucial to seeing spectral characteristics.

5.1.3 Temporal Complexity.

The amount of prism rotation in a single frame should be kept below 6°. If it was any more than that, motion blur would begin to degrade the intensities in the image by more than 50%. The 6°/frame threshold was for the worst case scenario. The blue wavelengths deteriorated at that rate much more than the reds because of the dispersion curve. When a broad spectrum scene is required, the blue wavelengths were the limiting case.

There was a marked improvement in image quality from a data set that included 3/4 of a prism rotation compared to one with only 1/2. There was not much of an improvement, if any at all, when going from 3/4 to a full rotation. Anything less than 3/4 began to lose entire spatial features. Therefore, at least 3/4 of a prism rotation (at a rate of 60 frames per rotation) is needed to get good image quality.

Finally, as few as 12 frames can be used in a full rotation to get a usable image. It was more grainy than a picture reconstructed with 60 frames, but there was not a significant reduction in image quality. The scene also must not change significantly over the course of the rotation. It was not quantified what a significant change was, but that will help in determining required rotation rate, frame rate, and exposure time.

5.1.4 Field Demonstration.

A fireball was imaged to pull all aspects of the research effort together. It had complex spatial and spectral characteristics and its shape evolved over time. It was shown that a transient event can be reconstructed by chromotomography. Selecting the proper prism and camera settings was extremely important. What was even more important was using the right combination of recorded frames to do a reconstruction. The spectrum built showed

important features but had very wide line widths. Because it was impossible to collect a pristine image of a scenario without repeatable results, image reconstruction was difficult to assess.

5.2 Lessons Learned

5.2.1 The Cone of Missing Information.

The cone of missing information proved to be a problem. By deleting the lower spatial frequency ξ values, it would often lose entire regions in an image. This was especially true at wavelengths with lower intensity. Deleting higher spectral frequency ζ values prevented sharp spectral transitions in the hypercube. Instead of a Mercury hypercube only having spatial structure at the 435, 546, and 578 nm slices, there was data in every slice. The structure was sharpest in on-wavelength layers and gradually softened further out. The missing cone seemed to affect filtered backprojections more than unfiltered backprojections, but it was not clear why.

5.2.2 Filtered and Unfiltered Backprojections.

It was unclear whether using the "backprojection then filter" reconstruction algorithm was an improvement over the unfiltered backprojection. The filter gave inconsistent behavior between good reconstructions, even in the same data set. For instance, one bright emission in Neon looked like a "positive" image and another looked like a "negative." It also lowered the overall intensity in a scene and accentuated the effects of the cone of missing information. It was successful at filtering out some of the artifacts. It did not completely get rid of all off-wavelength information, but it did often reduce it to the point of it looking like noise. Simple tests of varying μ indicated a value that was too low blurred the image, while a high value made it grainy. Further comparison of μ values must be done to determine the effects of choosing that value versus the fundamental limits of backprojecting then filtering.

5.2.3 *The Hypercube.*

Chromotomography, in this form, does not produce a traditional hypercube. If the intensities of one pixel through all wavelengths of the cube of a Mercury emission are plotted, it does not look like the spectrum. The spectral axis in the hypercube is not of the spectrum, but of reconstructions. The pseudo-spectra can only be teased out by looking at the quality of a reconstruction or contrast in the images. The reconstructions at wavelengths that are present should offer the highest contrast and would look like a spectrum plot when contrast is plotted versus wavelength.

5.3 Future Recommendations

The strongest recommendation would be to pursue algorithms designed to fill in the cone of missing information, such as Brodzik's Projection Onto Convex Sets [7]. Filling in that cone might restore low ξs and high ζs. That would in turn give energy in the low spatial frequency areas, especially in filtered backprojections. It would also give sharp spectral qualities and hopefully give spectral data only in slices of the cube where there was signal. If that succeeds, it is likely the spectrum can be measured the way all other hyperspectral methods do it.

The next recommendation is to develop a good way to measure the spectrum out of the hypercube if filling in the cone does not work. The techniques used in this project were hokie and weren't truly measuring spectra. They instead relied on measuring the quality of an image in each slice, plotting it versus wavelength, and calling it a spectrum.

Finally, develop a system that uses mirrors instead of refractive optics. The chromatic aberration made it very difficult to look at two wavelengths, even if they were relatively close together. If every wavelength is simultaneously in focus, the user will not have to make a decision on which to focus. Additionally, a full understanding of how the dispersion curve affects focus at each wavelength is required to ensure accurate reconstructions are performed throughout the band.

References

[1] *LOT-Oriel Group Europe Pen-Ray source manual*.

[2] Accetta, Joseph S. and David L. Shumaker. *The Infrared and Electro-Optical Systems Handbook*. SPIE Press, Bellingham, WA, 1993. ISBN 0819410721.

[3] Bernath, Peter F. *Spectra of Atoms and Molecules*. Oxford University Press, 198 Madison Ave, NY, 2nd edition, 2005. ISBN 139780195177596.

[4] Bernhardt, P. A. "Direct reconstruction methods for hyperspectral imaging with rotational spectrotomography". *J. Opt. Soc. Am. A*, 12(9):1884–1901, Sep 1995.

[5] Bostick, Randall L. and Glen P. Perram. "Hyperspectral Imaging Using Chromotomography: A Fieldable Visible Instrument for Transient Events". *International Journal of High Speed Electronics and Systems*, 18:519–529, 2008.

[6] Bridget K. Ford, Jose S. Salazar and Mark P. Wilson. *Reconstruction algorithm development and assessment for a computed tomography-based spectral imager*. Technical report, Air Force Research Laboratory, Albuquerque, NM, 2005.

[7] Brodzik, Andrzej and Jonathan Mooney. "Convex projections algorithm for restoration of limited-angle chromotomographic images". *J. Opt. Soc. Am. A*, 16(2):246–257, February, 1999.

[8] Deming, Ross W. "Chromotomography for a rotating-prism instrument using backprojection, then filtering". *Opt. Lett.*, 31(15):2281–2283, Aug 2006.

[9] Eismann, M.T. *Hyperspectral Remote Sensing*. SPIE Press, Bellingham, Washington, 1st edition, 2012. ISBN 9780819487889.

[10] Gribben, John. *The Scientists: A History of Science Told Through the Lives of Its Greatest Inventors*. Random House, 2004. ISBN 9780812967883.

[11] Hecht, Eugene L. *Optics*. Addison Wesley, 2002.

[12] Hsieh, Jiang. *Computed Tomography*. SPIE Press, Bellingham, Washington, 2007. ISBN 9780819478382.

[13] Jonathan M. Mooney, Myoung An, Virgil E. Vickers and Andrzej K. Brodzik. "High-throughput hyperspectral infrared camera". *J. Opt. Soc. Am. A*, 14(11):2951–2961, 1997.

[14] Karow, Hank H. *Fabrication Methods for Precision Optics*. John Wiley and Sons, Inc., Hoboken, NJ, 1st edition, 2004. ISBN 0471703796.

[15] Laboratory, Jet Propulsion. "Airborne Visible/Infrared Imaging Spectrometer". Online, August 1992. URL http://aviris.jpl.nasa.gov/aviris.

[16] Mantravadi, S. "Spatial and Spectral Resolution Limits of Hyperspectral Imagers Using Computed Tomography: A Comparison". *Proc. IEEE Aerospace Conf*, 1–6. 2007.

[17] Mooney, Andrzej Brodzik, Jonathan M. and Myoung An. "Principle component analysis in limited-angle chromotomography". *SPIE*, 3118:170–178, 1999.

[18] Mooney, Jonathan T. "Angularly Multiplexed Spectral Imager". *SPIE*, 2480:65–77, 1995.

[19] Niederhauser, Jason D. *Design and characterization of a space based chromotomographic hyperspectral imaging system*. Master's thesis, Air Force Institute of Technology, 2011.

[20] O'Dell, Daniel. *Development and Demonstration of a Field-Deployable Fast Chromotomographic Imager*. Master's thesis, Air Force Institute of Technology, 2010.

[21] Optics, Ocean. "Spectrometer Operating Principles". Online, 2012. URL http://www.oceanoptics.com/technical/operatingprinciples.asp.

[22] Palmer, James M. and Barbara G. Grant. *The Art of Radiometry*. SPIE Press, Bellingham, WA, 1st edition, 2010. ISBN 9780819472458.

[23] Payling, Richard and Peter Larkins. *Optical Emission Lines of the Elements*. John Wiley and Sons Ltd., Baffins Lane, Chichester, West Sussex, England, 2000. ISBN 0471623784.

[24] Su'e, Chad B. *Characterization of a Hyperspectral Chromotographic Imaging Ground System*. Master's thesis, Air Force Institute of Technology, 2012.

[25] Vision Research, Inc., 100 Dey Road, Wayne, NJ, 07470. *Spectral and Color Responses for Phantom Cameras, v5.1*, 1.0.0 edition, 07 Dec 2004.

[26] Voelz, David. *Computational Fourier Optics*. SPIE Press, Bellinghma, Washington, 2010. ISBN 9780819482044.

REPORT DOCUMENTATION PAGE

1. REPORT DATE *(DD–MM–YYYY)*	2. REPORT TYPE	3. DATES COVERED *(From — To)*
27–03–2014	Master's Thesis	Oct 2012–Mar 2014

4. TITLE AND SUBTITLE

An Experimental Evaluation of Image Quality for Various Scenarios In a Chromotomographic System With a Spinning Prism

5a. CONTRACT NUMBER

5b. GRANT NUMBER

5c. PROGRAM ELEMENT NUMBER

6. AUTHOR(S)

Dufaud, Kyle J., Captain, USAF

5d. PROJECT NUMBER

5e. TASK NUMBER

5f. WORK UNIT NUMBER

7. PERFORMING ORGANIZATION NAME(S) AND ADDRESS(ES)

Air Force Institute of Technology
Graduate School of Engineering and Management (AFIT/EN)
2950 Hobson Way
WPAFB, OH 45433-7765

8. PERFORMING ORGANIZATION REPORT NUMBER

AFIT-ENP-14-M-07

9. SPONSORING / MONITORING AGENCY NAME(S) AND ADDRESS(ES)

Intentionally Left Blank

10. SPONSOR/MONITOR'S ACRONYM(S)

11. SPONSOR/MONITOR'S REPORT NUMBER(S)

12. DISTRIBUTION / AVAILABILITY STATEMENT

DISTRIBUTION STATEMENT A:
APPROVED FOR PUBLIC RELEASE; DISTRIBUTION UNLIMITED

13. SUPPLEMENTARY NOTES

This work is declared a work of the U.S. Government and is not subject to copyright protection in the United States.

14. ABSTRACT

A lab and field based hyperspectral chromotomographic imager has been developed at the Air Force Institute of Technology. It is a prototype used to study the requirements for a space-based system. The imager uses a high speed visible band camera behind a direct-vision prism to image both spatial dimensions and the spectral dimension at the same time. Capturing all 3 simultaneously allows for the hyperspectral imaging of transient events. The prism multiplexes the spectral and spatial information, so tomographic reconstruction algorithms must be used to separate hyperspectral channels.

Experiments were conducted to compare reconstructed image quality as a function of spatial, spectral, and temporal complexity. To test spatial complexity, a simulated point source, a standard bar chart, and an amorphous object were imaged. The more simple objects were reconstructed well. When objects dispersed by the prism overlapped in the raw data, reconstructions diminished. To test spectral complexity, atomic emission lines and white light with different types of optical filters were imaged. Because of the way the prism disperses light, shorter wavelengths were reconstructed better than longer ones. The temporal complexity experiments determined 3/4 of a prism revolution is sufficient (with approximately 60 projections) to reconstruct a scene as long as there were a sufficient number of frames in the recording. As few as 12 frames are sufficient in a complete revolution. Finally, a fireball was imaged in a field experiment. The chromotomographic imager constructed the spectrum of the fireball with very wide spectral lines.

Hindrances to reconstruction, such as a cone of missing hyperspectral information, are discussed. Additionally, a comparison of and improvements to the reconstruction algorithms are suggested.

15. SUBJECT TERMS

Hyperspectral Imagery, Chromotomography, Direct-Vision Prism, Image Reconstruction

16. SECURITY CLASSIFICATION OF:			17. LIMITATION OF ABSTRACT	18. NUMBER OF PAGES	19a. NAME OF RESPONSIBLE PERSON
a. REPORT	b. ABSTRACT	c. THIS PAGE			Dr. Michael R. Hawks (ENP)
U	U	U	UU	146	**19b. TELEPHONE NUMBER** *(include area code)* (937) 255-3636 x4828 michael.hawks.ctr@afit.edu